MICROFLUIDIC TECHNOLOGIES
FOR STRUCTURAL BIOLOGY

Thesis by

Carl L Hansen

In Partial Fulfillment of the Requirements

For the Degree of

Doctor of Philosophy

CALIFORNIA INSTITUTE OF TECHNOLOGY

Pasadena, California

2004

(March 28, 2004)

© 2004

CARL L HANSEN

ACKNOWLEDGEMENTS

I would first like to thank my advisor, Stephen Quake, for his unwavering direction and steadfast resolve. Steve has been without exception a first rate mentor and role model.

From the inception of this work James Berger has been an instrumental part. I thank him for his willingness to innovate and his continued faith in this project. I also would like to thank Emmanuel Skordalakes and Jan Erzberger of the Berger lab for there excellent collaboration.

Additionally, I have had the opportunity to work with a number of excellent academic and industrial collaborators. In particular I would like to thank Pamela Bjorkman, Douglas Rees, and Francis Arnold for generously donating samples and for their continuing interest in this project. I would further like to thank Kyle Self and Gajus Worthington of Fluidigm Corporation for their huge effort and commitment to this project.

Special thanks goes to Morten Sommer who worked with me on the Formulator project while visiting Caltech as an undergraduate. His relentless enthusiasm and "naïve" optimism make working with him an absolute pleasure. I expect that he will have terrific success in his career.

Many thanks also go out to Todd Squires whose discussions over coffee have been both enjoyable and insightful. In particular I thank him for his insight into the fluid mechanics of the rotary mixer and water permeation in the harvesting device.

I extend my sincere gratitude to many colleagues whose exceptional ability and warm camaraderie have made my time at Caltech so enjoyable. In particular I thank Sebastian Maerkl, Vincent Studer, Joshua Marcus, Mark Adams, Frederick Balagadde, and Jian Liu, with whom I have worked most closely. I would also like to extend my thanks to Emil Kartalov, Heun Jin Lee, Jordan Gerton, Larry Wade, Michael Vandam, Michael Diehl, and Ido Braslovski for their comradeship. I am further grateful to Marcus Enzelberg for his patience and mentorship early in my graduate career.

Many of my fondest memories at Caltech are from cycling through the mountains around Pasadena. I thank Michael Johnson, Tobias Kippenberg and Peter Meinhold for their valued friendship and motivation. Tobias Kippenberg I also thank for teaching me patience through his persistent tardiness, and for being a worthy adversary.

I would like to acknowledge my undergraduate research advisor and new colleague, Andre Marziali, for introducing me to the fields of biophysics and biotechnology and for being my advocate over the past 5 years.

I am very grateful to the Canadian government for their continued investment in Canadian scholars, and for the financial support they provided me in the form of a Julie Payette scholarship during the 2nd and 3rd years of my graduate career.

Finally, I thank those that are dearest to me and who have supported me through all my endeavors. My parents, Don and JJ, I thank for their commitment to training, their enthusiasm for science, and their philosophical guidance. I thank my sisters, Elsa and Johanna, who through their own scientific careers are a continual source of encouragement and support. I thank my sister in law, Tiffany, for many good laughs on the phone and on vacations. I am hugely grateful to my twin brother Maxim for his example, his solidarity, and his strength. Above all I would like to express my deepest appreciation to Tara for her continued love, encouragement, and support over the past four years. I could not have done this without her.

Carl L. Hansen

May 13, 2004

ABSTRACT

In the post-genomic era, X-ray crystallography has emerged as the workhorse of large-scale structural biology initiatives that seek to understand protein function and interaction at the atomic scale. Despite impressive technological advances in X-ray sources, phasing techniques, and computing power, the determination of protein structure has been severely hampered by the difficulties in obtaining high-quality protein crystals. Emergent technologies utilizing microfluidics now have the potential to solve these problems on several levels, both by allowing researchers to conduct efficient assays in nanoliter reaction volumes, and by exploiting the properties of mass-transport at the micron scale to improve the crystallization process. The technique of Multilayer Soft Lithography (MSL) has been used to developed a set of microfluidic tools suitable for all stages of protein crystallogenesis, including protein solubility phase-space mapping, crystallization screening, harvesting, and *in silicone* diffraction studies. These tools represent the state of the art in on-chip fluid handling functionality and have been demonstrated to dramatically improve protein crystallization.

TABLE OF CONTENTS

LIST OF FIGURES

Chapter 1

OVERVIEW

Introduction

The industrialization of DNA sequencing and completion of numerous genome projects has set the stage for the next great endeavor, illuminating the cellular proteomes. Just as the invention of the microscope helped to bring about an understanding of life at the cellular scale (1), X-ray crystallography has allowed scientists to observe proteins at the atomic level, causing a structural revolution in the biological and medical sciences. A conservative estimate is that through alternative splicing, the 30 000 genes that have been identified in the human proteome will give rise to over 100 000 proteins whose structures and functions are largely unknown. The diversity of proteomes across species, the need to elucidate complex protein/protein interactions, and the visualization of ligand and drug binding, imply an effectively limitless number of crystallization targets (2).

Technological advances in synchotron X-ray sources, phasing techniques, and computing power have revolutionized data collection and model building techniques (3-5). These innovations have not however been matched by the development of techniques to rapidly obtain high-quality crystals. Major bottlenecks in the expression, purification, and crystallization of macromolecule targets continue to thwart high-throughput structural biology initiatives (6). As structure determination efforts begin to focus less on the most tractable crystallization targets (typically small soluble proteins), and instead on more challenging macromolecules, including large protein complexes and membrane proteins,

the need to develop novel and enabling technologies has become urgent (7-9). The bottlenecks associated with generating diffraction quality crystals are further exacerbated by the fact that many of the most interesting crystallization targets are difficult to express and purify in large amounts.

Microfluidic technologies have the potential to provide unprecedented economies of scale and massively parallel sample processing, making them ideal candidates for applications where the screening and processing of precious reagents is required (10-12). The fluid handling functionality necessary for realizing diverse and complex biological assays on a chip requires the integration of active valves. A recent breakthrough in fabrication techniques, Multilayer Soft Lithography (MSL) (13), uses non-conventional soft materials to fabricate true sealing valves. As a fundamental building block, these valves may be used to build up higher level fluidic components such as pumps, mixers, and injectors (13, 14).

Beyond reduction in sample consumption, the reduced length scale of microfluidic structures allows access to unique regimes of mixing and fluid flow that are not manifested in macroscopic devices. Realizing the true potential of microfluidic technologies therefore requires an understanding of the fluid physics that dominate at the micron scale. Exploiting the physical behaviors that are characteristic to the micro-environment thereby allows for the implementation of assays with increased sensitivity and higher efficiencies than are achievable by conventional techniques.

The focus of this thesis is the application of Multilayer Soft Lithography to the development of microfluidic tools that accelerate and improve protein crystallogenesis. The emphasis of this work is on realizing the highest possible scientific impact by enabling science that has hereto been intractable, and the marriage of engineering and science is a central theme in this work. The utility of a technology depends not only on sound scientific principals, but further on maximal robustness, reliability, and accessibility. These engineering principals must be present from the inception of design, and are inextricably coupled to the underlying science.

Furthermore, effective technology development requires intimate familiarity with the current methodologies and problems. Only once the inventor is immersed in the field and able to consolidate this experience with his technical expertise do the most elegant and simple solutions present themselves. Throughout this work a large effort has therefore been directed towards validating the technology through application to outstanding crystallization problems.

Context

This work builds upon the Multilayer Soft Lithography (MSL) technology developed by previously in our lab by Unger *et al.* (13). At the time the author began his work on protein crystallization in microfluidic devices, MSL was an emerging technology with enormous potential and obvious advantages over existing methodologies. It was still however in a nascent form, and technical issues severely limited the complexity of devices that could be

realized. The author has had a major role in resolving these issues and establishing MSL as a robust and reliable technology platform.

This thesis describes the first application of microfluidics to protein crystallization. In this work the development of a variety of microfluidic devices suitable for all aspects of protein crystallogenesis is described. The most mature of these technologies is a device for ultra-small volume screening of crystallization conditions by microfluidic free interface diffusion. This screening device has advanced past the prototype stage and has been extensively tested in the crystallization of diverse and challenging macromolecule targets. The screening device has been developed into a commercial product by Fluidigm Corp., and is being successfully used in structure determination projects at major pharmaceutical companies in the United States and Great Britain.

A microfluidic formulator device has been developed for the systematic characterization of protein solubility over a broad range of chemical conditions. This device allows for the first practical implementation of high-throughput solubility characterization in nanoliter volume reactions. Additionally, this device has enabled the first implementation of true combinatorial mixing on chip and represents the state of the art in microfluidic functionality and precision. The formulator device is currently in the 10th prototype version and is being refined for routine use an instrument for rational protein crystallization.

A diffraction device has been developed to allow for successful chip-based crystallization conditions to be exported with high correspondence to larger volume formats.

Additionally, this device allows for the rapid harvesting and mounting of crystals, and for *in silicone* diffraction studies both at cryogenic and at room temperatures. The diffraction device is in a early prototype stage and is currently being developed both at Caltech and at Fluidigm Corp. for commercialization.

Organization and Collaborations

Chapter 2 discusses the extension of MLS technology to the development of robust and scaleable methods for metering and dispensing reagents on chip, a fundamental requirement for all liquid handling systems. The Chapter begins by introducing the method of pressurized outgas priming. This technique is central in solving problems of device priming, small-volume sample loading, suppressing bubble formation, and maintaining sample hydration. Pressurized outgas priming allows for the simple implementation of robust metering scheme called geometric metering, which is used in the protein crystallization screening device. A second metering technique, positive displacement cross-injection (PCI) metering is also presented. This technique is used in the formulator device to realize precise and robust programmable metering on chip.

Chapter 3 begins with an introduction to the characteristic energies of protein crystallization and growth. Simple physical models are presented to provide a framework for later discussions of mixing kinetics and crystal nucleation. In particular, the concept of "crystallization phase-space" is presented. The properties of mass transport that are manifested in microfluidic devices allow for the efficient sampling of crystallization phase-space by a technique called microfluidic free interface diffusion.

Chapter 4 describes a protein crystallization screening device that uses geometric metering to realize a parallel implementation of microfluidic free interface diffusion. The effectiveness of this device is evaluated in the context of both well-characterized crystallization standards and challenging real-world crystallization targets. Protein samples used in these trials were generously provided by a number of academic collaborators: most notably the labs of J. Berger, P. Bjorkman, D. Rees, F. Arnold, and D. Eisenberg.

Chapter 5 describes a microfluidic formulator device designed for the systematic exploration of protein phase-space behavior. This device integrates valves, pumps, multiplexers, and a mixer to achieve programmable combinatorial mixing on chip. Characterization of chip reliability, metering precision and robustness are presented. Additionally, issues of cross-contamination and i/o interfacing are discussed. This work was done in equal collaboration with M. Sommer.

Chapter 6 discusses achieving fast mixing in the formulator device through mixer optimization. The application of simple fluid mechanics is used to determine the scaling laws that govern mixing times in a rotary mixer. This discussion follows work done by T. Squires. The behavior of the mixer is further investigated through numerical simulations done in equal collaboration with M. Sommer. Finally, the optimization of valve response time for achieving high flow rates in the rotary mixer is discussed.

Chapter 7 describes the use of the formulator device in the systematic study of the solubility behavior of Endo-1,4-β-xylanase (xylanase) from *Trichoderma reesei*. Solubility fingerprinting and phase-space mapping are used to characterize xylanase in a variety of precipitating agents. Information gained from these studies is used to design an optimal crystallization screen that dramatically enhances the chance of crystallization when compared to commercial sparse matrix screens (15). This work was done in equal collaboration with M. Sommer.

Chapter 8 describes a diffraction device that allows successful crystallization conditions identified in the screening device to be transported with high correspondence to a larger volume format. A technique for rapid harvesting and mounting of crystals for *in silicone* diffraction studies at cryogenic and room temperatures is presented. By minimizing crystal manipulations and providing a harvesting format amenable to automation this device establishes a clear path from crystals to structure.

Chapter 9 begins with an overview of multilayer soft lithography (MSL) as developed by Unger *et al*. The goal of the remainder of the Chapter is to highlight various technical issues related to MSL technology, and to document some useful solutions that have been realized throughout the course of this work. It is the author's hope that this section will provide a useful resource to students new to the field. Practical considerations and design problems that previously limited the reliability and achievable complexity of devices are discussed. Other issues related to fabrication and component design are presented. In

cases where the author had a major contribution only in the conception of solutions, with the implementation carried out by other students, appropriate references are made.

Chapter 2

ROBUST AND SCALEABLE MICROFLUIDIC METERING

Introduction

In the same way that miniaturization has impacted the electronics industry, microfluidic technologies promise to spark a revolution in the biological sciences by integrating ultra small-volume sample processing within a chip format. The use of nanoliter reaction volumes and highly scaleable parallel sample processing makes microfluidic technologies ideally suited to protein crystallography, where the screening and processing of precious reagents is required. Beyond reduction in sample consumption, the unique properties of mixing and fluid flow at the micron scale also allow for the implementation of assays that are highly efficient at detecting crystallization conditions (16). Despite this enormous potential, several technical problems have prevented the realization of the full potential of microfluidic devices for protein crystallization.

Central to the realization chip-based protein crystallization and other lab-on-chip technologies is achieving the fundamental fluid handling capability of precisely metering and mixing fluids at the sub-nanoliter scale. In order to be scaleable and to have general applicability, such a system must further be insensitive to both the surrounding fluidic architecture and to the properties of the working fluids. In the case of protein crystallography, this latter requirement is particularly important since the solutions used in crystal trials cover a large range of chemistries, viscosities, ionic strengths, and pH.

The early work in microfluidics was focused on the development of glass microchips that exploited electrokinetic manipulation of fluids for applications such as enzymatic assays and molecular separations. This work demonstrated that microfabricated fluidic structures may be used to accurately meter and mix fluids on the picoliter scale (17-22). Although these systems have proven useful in niche applications such as capillary electrophoresis, they have not proven to be scaleable, and have fundamental limitations that prevent there universal application. For example, the electrokinetic force used in these devices depends strongly on both the properties of the working fluid and on its interaction with the channel walls. Small changes in pH or salt concentration, that result from ion drift over time, can lead to more than a tenfold variation in injected volume (23, 24). These systems are also dependent on the viscosity and on the fluidic resistance due the surrounding channel architecture. As a result, electrokinetic devices must be recalibrated for every fluid, and are not suitable for high-throughput screening applications with a diverse ensemble of unrelated reagents.

Moreover, since electrokinetic systems have no active valves, reagents diffuse through junctions and channels over time. This leaking dilutes and contaminates samples over time, restricting the maximally achievable incubation times and the density at which assays may be integrated on chip. The problem of reagent storage is particularly acute for crystallization applications where assays may be required to incubate for several days or weeks.

All of these problems may be addressed by using MEMS (micro-electro-mechanical systems) fabrication techniques to incorporate active mechanical valves on chip. Traditional MEMS techniques, using "hard" materials such as glass or silicon, may be used to fabricate true, leak-proof mechanical valves. However, MEMS fabrication techniques are expensive and require many processing steps, rendering the integration of many valves on a chip a difficult and expensive process. Furthermore, since these valves are fabricated from hard materials, a large actuator area is needed to achieve valve closure at attainable actuation forces. The large actuators of each valve and the low yield of the fabrication process impose practical constraints on the degree of integration that is possible in microfluidic devices made from traditional MEMS techniques.

While there is a thriving MEMS community making silicon-based valves and microfluidic devices, alternative fabrication techniques using non-traditional materials, including hydrogels (25), plastics, and elastomers (26, 27), are gaining popularity and have been developed for the quick and inexpensive fabrication of passive and active microfluidic devices. In particular a technique developed by Unger *et al.*, Multilayer Soft Lithography (MSL), enables facile and inexpensive large-scale integration of valves on chip (27). MSL uses consecutive soft lithography molding and bonding steps to generate complex multilayer fluidic devices. In this way, planar channel structures separated by only a thin flexible elastomeric membrane may be integrated into a monolithic polymer chip. The orthogonal crossing of channel structures in two adjacent layers creates a deflectable membrane valve. A hermetic seal of the channel structure may be easily achieved at by application of modest hydraulic or pneumatic pressure to the control

structure. The low Young's modulus of the elastomer (~1 MPa compared to ~100 GPa for crystalline silicon) allows for the large deflection of membranes with small active areas (typically 10000 μm^2), thereby enabling the large-scale integration of valves on a chip (27). Moreover, the softness of the channel and valve structure ensures the formation of a robust seal even in the presence of particulates or fabrication imperfections.

This Chapter describes the extension of MSL technology to the development of two metering techniques that are both scaleable and robust to the properties of the working fluid. The first of these techniques, geometric metering, relies on the ability to easily prime arbitrary connected fluidic structures via the pressurized outgas priming (POP) method. Geometric metering is a static technique whereby the final aliquot volumes and mixing ratios are defined by the fluidic structure. This robust technique is extremely powerful by virtue of its simplicity of operation and scalability to massively parallel architectures, and is central to the implementation of a protein crystallization screening device (Chapter 4). An extension of this technique, in the form of variable volume nanopipettes, allows for a degree of programmability to be achieved through the analogue or discrete tuning of cavity volumes. A second technique, positive displacement cross-injection (PCI) metering, is a dynamic technique that allows for the programmable serial dispensing of an arbitrary number of reagents. This versatile method is used to realize the first demonstration of true combinatorial mixing on chip (Chapter 5).

Pressurized Outgas Priming

The realization of highly integrated and complex fluidic devices requires that the problem of priming, or initially filling the device with fluid, be addressed. For microfluidic devices made from conventional hard materials such as silicon or glass, this requirement may prevent the use of multiply crossing, highly complex fluidic architectures. Such devices must be primed using a flow-through method, which requires an outlet through which displaced gas may be vented. The introduction of the priming fluid through a complex fluidic structure may trap air bubbles at junctions and other channel features. Surface tension effects at the liquid-gas interfaces of these bubbles result in large pressure drops so that bubbles can not be easily removed and adversely affect the performance of the device. Furthermore, since a single priming fluid must pass through the entire device, it may subsequently contaminate or dilute sample solutions. These difficulties can be surmounted in silicone devices by exploiting the gas permeability of a soft silicone polymer (28, 29). The permeability of silicone rubber to a variety of gases is listed in Table 1 (30).

Penetrant	Permeability (Barrer)
H_2	890 ± 30
O_2	800 ± 20
N_2	400 ± 10
CO_2	3800 ± 30

Table 1: Permeability of poly(dimethylsiloxane) to various gases. 1 Barrer = 10^{-10} cm^3(STP)·cm/cm^2·s·cm Hg.

Arbitrarily complex, connected fluidic structures may be filled in minutes by a technique called Pressurized Outgas Priming (POP). Using the POP technique, a fluid is injected into a closed channel structure, causing the gas ahead of it to be pressurized. Due to the permeability of the elastomer, the pressurized gas quickly diffuses into the bulk material, allowing the priming fluid to completely fill the flow structure. Figure 1 shows a time sequence of a 7 nL well being dead-end filled at 8 psi loading pressure. Despite the low surface energy of PDMS (22 mJ/m^2), aqueous solutions may be easily introduced, at moderate pressures (1-8 psi), into channels having a minimum dimension of 1 μm, eliminating the need for surface modification protocols. Since no outlet is needed for the venting of gas, dead-end reaction chambers and channels may be used, allowing significant design flexibility. Furthermore, since the priming is selective and integrated valves may be used to direct flow of the fluid, a device can be primed with many different fluids in different channels or chambers. This latter property is the basis of the geometric metering scheme described below. A more comprehensive introduction to MSL technology and various relevant technical issues is provided in Chapter 9.
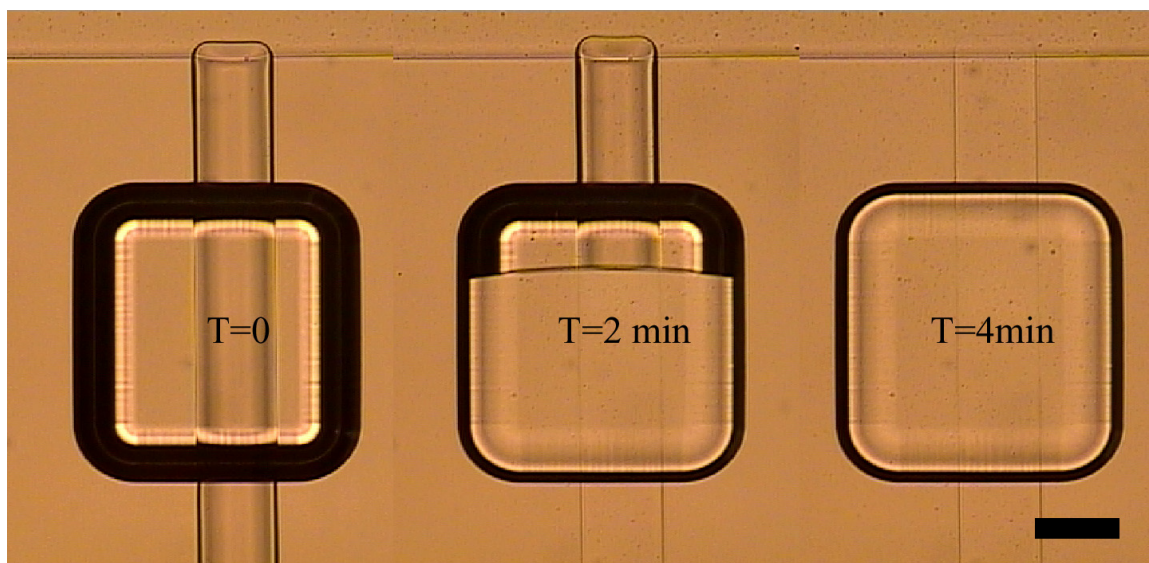
Figure 1: Opical micrographs showing the dead-end filling of a 7.5 nL reaction chamber at 8 psi using the pressurized outgas priming (POP) method. Scale bar is 100 μm.

Geometric Metering

The ability to fill a device with many different fluids in different channels and chambers using the POP technique allows for the implementation of a simple and robust geometric method of metering solutions. The principle behind this scheme is to set up a geometry in which interface valves are used to partition a continuous microfluidic reactor into sections of well-defined volume. Each section may be separately filled with different solutions through separate inlet channels. Once filling is complete, the inlet channels are sealed by actuation of containment valves, thereby isolating the reactor from the rest of the device. De-actuation of selected interface valves allows for adjacent sections of the reactor containing different reagents to be combined.

A simple fluidic structure for the geometric metering of two reagents at three different mixing ratios is shown in Figure 2A. With a central interface valve closed, the chambers on either side of the interface are first dead-end filled with two different solutions using the POP technique (Figure 2B). Once both chambers have been completely filled, the containment valves are actuated, thereby isolating the chambers from the rest of the chip and defining the total volume of the reactor. The interface valve is then opened to create fluidic connection between the chambers, allowing them to mix by diffusion. Figure 2C shows the complete diffusive mixing of an organic dye with water, creating a set of three distinct concentrations in separate reaction chambers.
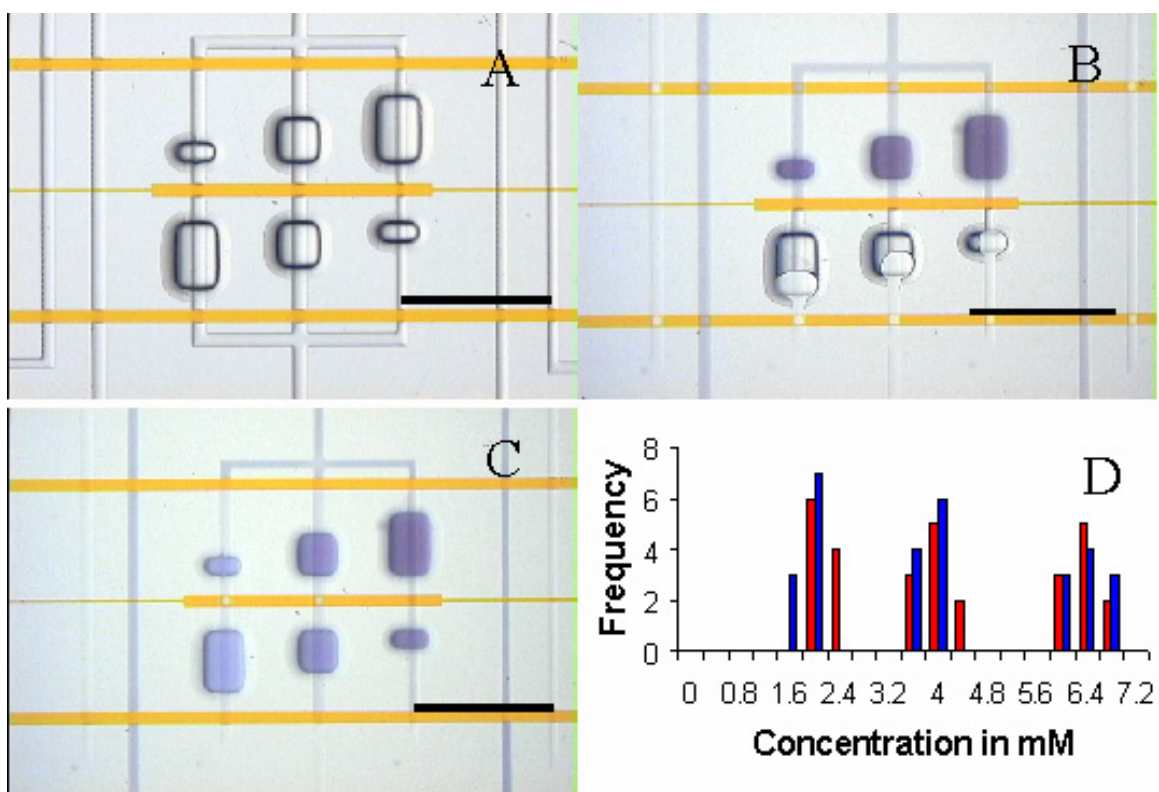
Figure 2: Geometric metering. **(A)** Three pairs of coupled microwells. Control channels are filled with 20 mM Orange G (Aldrich Chemical Company). **(B)** Loading of reagents using POP method. The interface valve (center) is actuated and reagents are loaded into adjacent sides of compound wells. The bottom wells are being dead-end loaded with water, and the top wells have been loaded with 13 mM bromophenol blue sodium salt (Aldrich Chemical Company). **(C)** A gradient of dye concentration. The containment valves (top and bottom) isolate compound wells, and the interface valve is released to allow diffusive mixing. Image shows complete mixing after 2 hours. **(D)** Histogram showing the insensitivity of BIM to fluid viscosity. BIM was used to combine 7 mM bromophenol blue sodium salt with water ($\eta \cong 1$ cP) or 34% m/m sucrose ($\eta \cong 4$ cP) tens times each at mixing ratios of (Dye:water/sucrose) 1:4, 1:1, and 4:1. Water measurements are shown in blue, and sucrose is shown in red. The variations in the concentration measurements ($\sim$ 10%) are comparable to those taken on solutions of known concentrations.

In this way the chambers effectively act as microfluidic measuring cups, precisely determining the mixing ratio by the relative chamber volumes. Since the metering depends only on the volume of the chambers it is an inherently robust technique that is insensitive to resident fluid properties. Figure 2D shows a histogram of mixing ratios achieved in 20 sets of 3 reaction chambers using two fluids of varying viscosity. Similar experiments using solutions of sodium chloride ranging from 0 M to 2 M have shown that metering is independent of ionic concentration (data not shown).

In this simple configuration, mixing is dominated by diffusion of the reagents, which takes on the order of an hour for small molecules in an aqueous solution. This purely diffusive mixing is sometimes advantageous in that it removes the confounding effects of convection, thereby allowing for slow equilibration of the various reagents. In cases for which speed is an issue, it is straightforward to implement the BIM scheme in alternative geometries, such as a ring, and then accelerate mixing by dispersion induced through active pumping around the ring (see Chapter 6). This scheme has found applications in single-cell gene expression analysis and large-scale multiplexed PCR reactions (31, 32).

A major advantage of this technique lies in its simplicity of control and scalability. The volume of the reaction chambers is precisely defined during lithography and molding so that there is no need to calibrate the system. Each of the steps in the metering and mixing process (interface actuation, filling, containment, and diffusive equilibration) proceeds to completion prior to the initiation of the next step, so that there is no requirement of precise valve actuation timing. Hence, thousands of reactions can be implemented in parallel using only two control lines irregardless of differences in the length of loading channels or in the fluid properties. Figure 3 shows a section of a device designed to implement 144 simultaneous metering and mixing experiments. The ability to implement large-scale parallel metering and mixing of reagents without increasing control complexity has been exploited in a variety of applications including protein crystallography (29, 33), multiplexed PCR reactions (32), and cell-library screening (27).
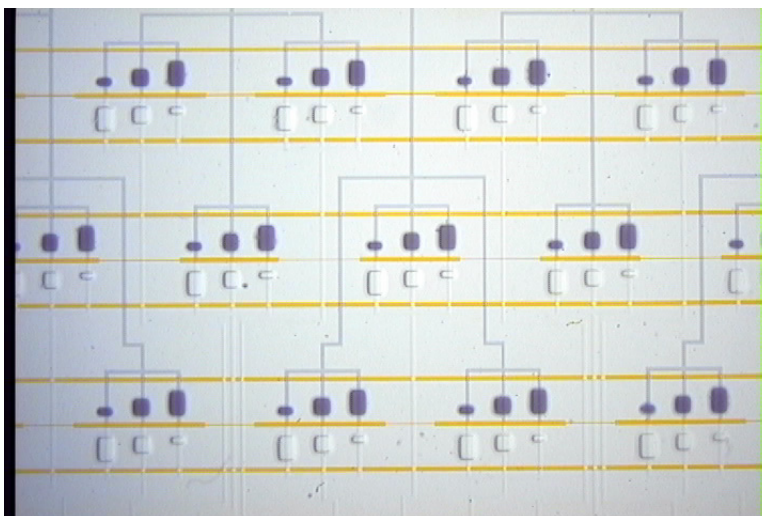
Figure 3: Parallel implementation of geometric metering. Section of a device designed for the simultaneous mixing and metering of a single sample (blue) with 48 unique reagents (clear) using only two control lines (orange).

Geometric metering is primarily a static technique in which the final dispensed volumes are "hard-wired" into the fluidic structure. Nevertheless a degree of programmability may be achieved by the inclusion of redundant valves and/or channels. Figure 4 shows a channel and valve geometry designed to allow for 10 alternate mixing ratios to be achieved by selection of one of many possible interface valves (I1 – I10) located at different locations along a reaction chamber defined by two containment valves (C). Additionally, a series of channel inlets could be included between each of the 12 valves to allow for many different numbers of reagents and mixing ratios to be implemented. Although this allows a large number of alternative configurations, such geometries greatly increase the control complexity of the device and may introduce severe routing problems that make them no longer scaleable to parallel implementations.
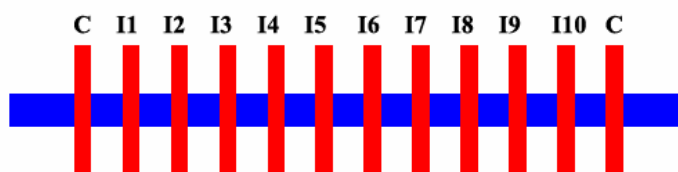
Figure 4: Channel architecture for programmable geometric metering. Selection of specific interface channel (I1 – I10) determines mixing ratio of fluids introduced at the channel inlets.

Alternatively, the geometric metering scheme may be extended to structures in which the total volume of the reaction chamber may be tuned in a continuous or discrete fashion by deflection of a membrane. Figure 5 shows a column of a microfluidic chip with an array of 1 nanoliter fixed-volume nanopipettes. Each column of nanopipettes is addressed by a separate input channel (clear). Each nanopipette has a containment valve at the inlet and a deflectable membrane. The size of each membrane defines the metered volume and is varied across the row.

The simple two-component metering of solutions at a variety of fixed mixing ratios is implemented as follows. The first fluids to be mixed are introduced into separate columns of the array via a multiplexing structure (not shown). The chip outlet is then closed and the nanopipette containment valves are opened to allow for the dead-end filling of each reaction chamber by the POP method. Once filled, the reaction chambers are sealed by actuation of the containment lines, and the next fluids to be mixed are flushed down the columns. Figure 5A shows 3 nanopipettes filled with an organic dye (20 mM bromophenol

blue sodium salt, TRIS·HCl pH 8.0). To execute the metering task the containment valves are opened and the membranes are inflated, ejecting a well-defined volume from each pipette (Figure 5B). The ejected volume is flushed from the column and replaced with the second solution (Figure 5C). The membranes are then deflated, causing a well-defined volume of the second reagent to enter the nanopipette (Figure 5D).
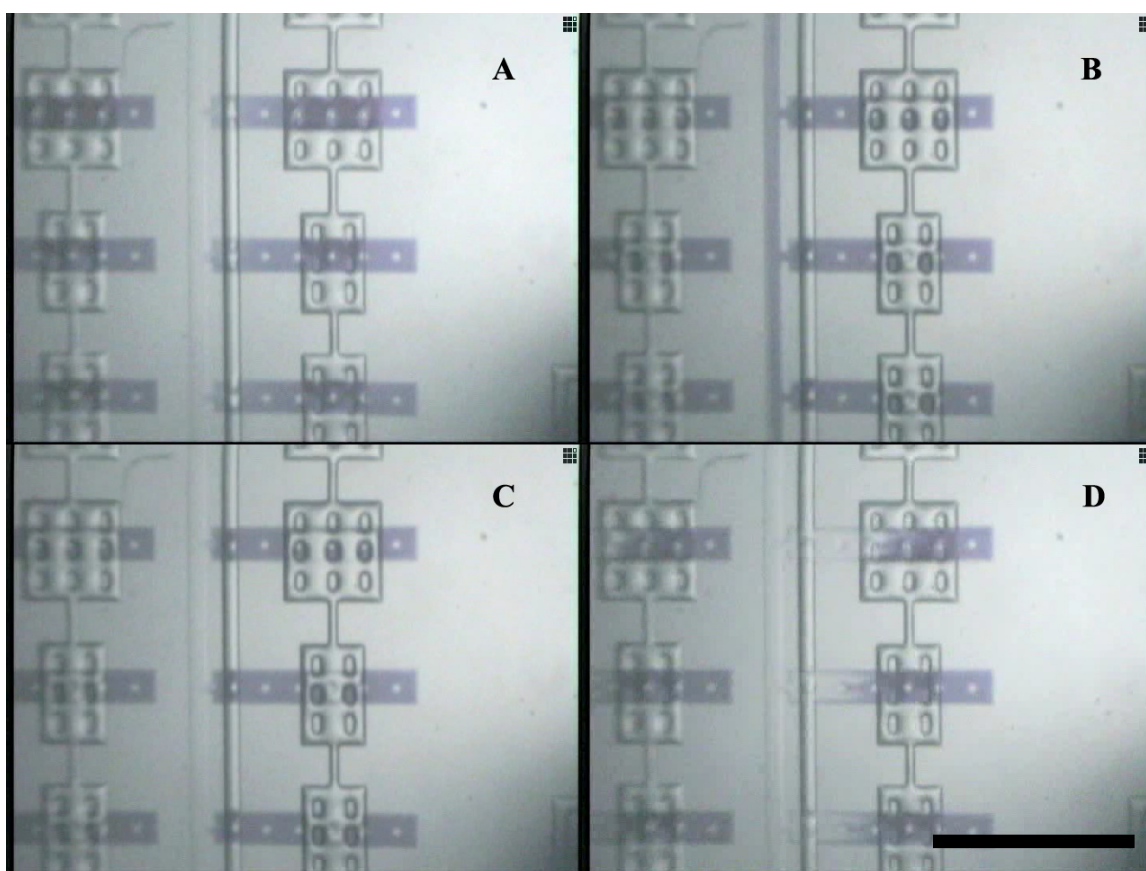
Figure 5: Parallel operation of fixed volume nanopipette. **(A)** Nanopipettes are filled first reagent (blue), containment valves are actuated, and inlet channel is flushed. **(B)** Membranes are inflated to expel a well-defined volume of first reagent. **(C)** Inlet

channel is flushed and loaded with second reagent. **(D)** Relaxation of membranes results in aspiration of a well-defined volume of second reagent.

In this setup the mixing ratio is determined by the membrane geometry and is therefore hard-wired into the device. Since a separate reagent is introduced to each column of the array and each nanopipette is designed to achieve a specific mixing ratio, this strategy allows for the parallel screening of different reagents at different mixing ratios. Figure 6 shows the mixing of two organic dyes (orange G and bromophenol blue sodium salt) at 0:1 (A), 1:3 (B), 1:1 (C), and 2:1 (D) ratios. In cases where parallel architectures are not required the nanopipette may be used to meter fluids in an analogue fashion. Varying the actuation pressure applied to deflect the membrane allows for continuous tuning of the nanopipette volume.
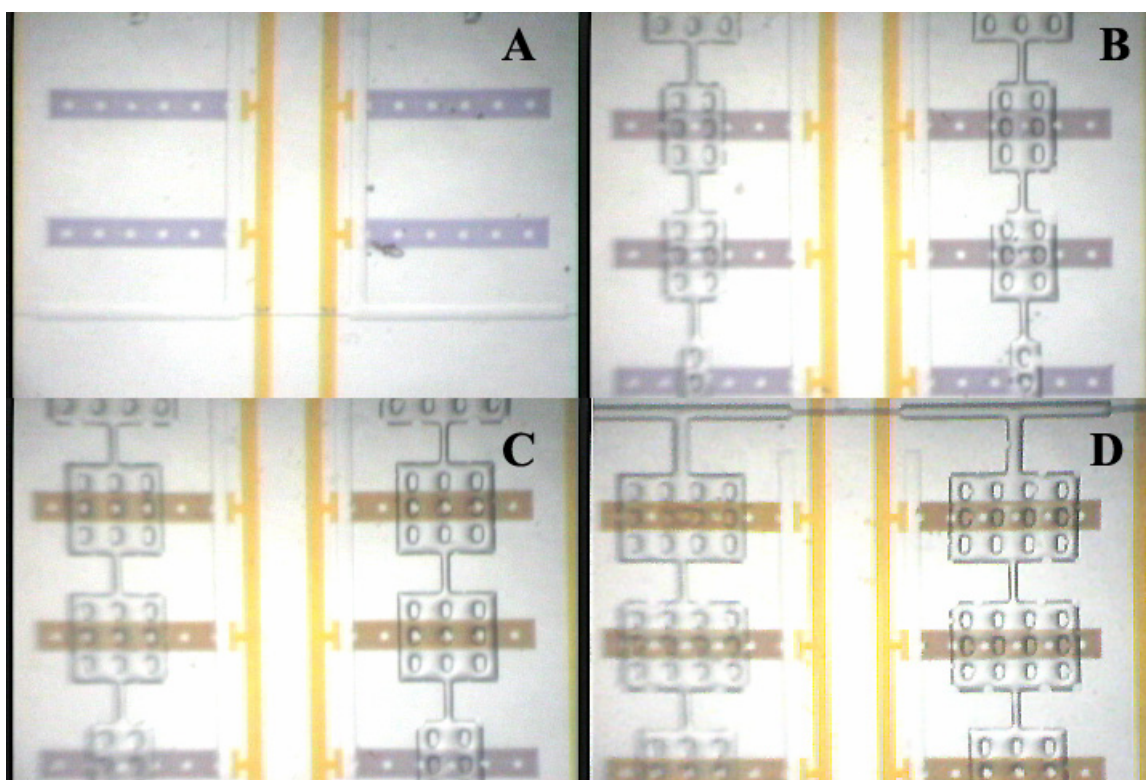
Figure 6: Parallel mixing at variable mixing ratios using an array of 1 nL nanopipettes. **(A)** 1 blue : 0 orange. **(B)** 3 blue : 1 orange. **(C)** 1 blue : 1 orange. **(D)** 1 blue : 2 orange.

Positive Displacement Cross-Injection Metering

Formulation applications require arbitrary combinations and concentrations of a large number of distinct reagents to be mixed on chip. This "mix-on-command" requirement necessitates a robust and programmable metering scheme that can accommodate a large number of input solutions. Positive displacement cross-injection metering allows for the sequential injection of precise sample aliquots from a single microfluidic channel into reaction chambers through a positive-displacement cross-injection (PCI) junction (Figure 7).

The PCI junction is formed by the combination of a three-valve peristaltic pump (13) and a four-port cross-injection junction with integrated valves on each port (Figure 7A). Two sets of valves at the junction inlets are actuated to direct the flow either horizontally or vertically. Prior to metering the flow is switched vertically through the junction, charging the cross-injector with the sample fluid (Figure 7B). The flow is then directed horizontally through the junction and the three valves forming the peristaltic pump are actuated in a five state peristaltic sequence to advance the fluid in the horizontal direction (Figure 7C). Each cycle of the peristaltic pump injects a well-defined volume of sample (approximately 80 pL) determined by the dead volume under the middle valve of the peristaltic pump. The

deflection of the valve membranes when not actuated is determined by the pressure difference across the membrane. The volume injected during each cycle therefore may be tuned continuously, allowing for variable positive displacement metering. By repeating the injection sequence, the volume of injected solution may be increased in 80 pL increments, allowing for the programmable quantized control of the final downstream sample concentration. After each injection sequence the junction is flushed and recharged allowing for the sequential introduction of different reagents down the line (Figure 7D).
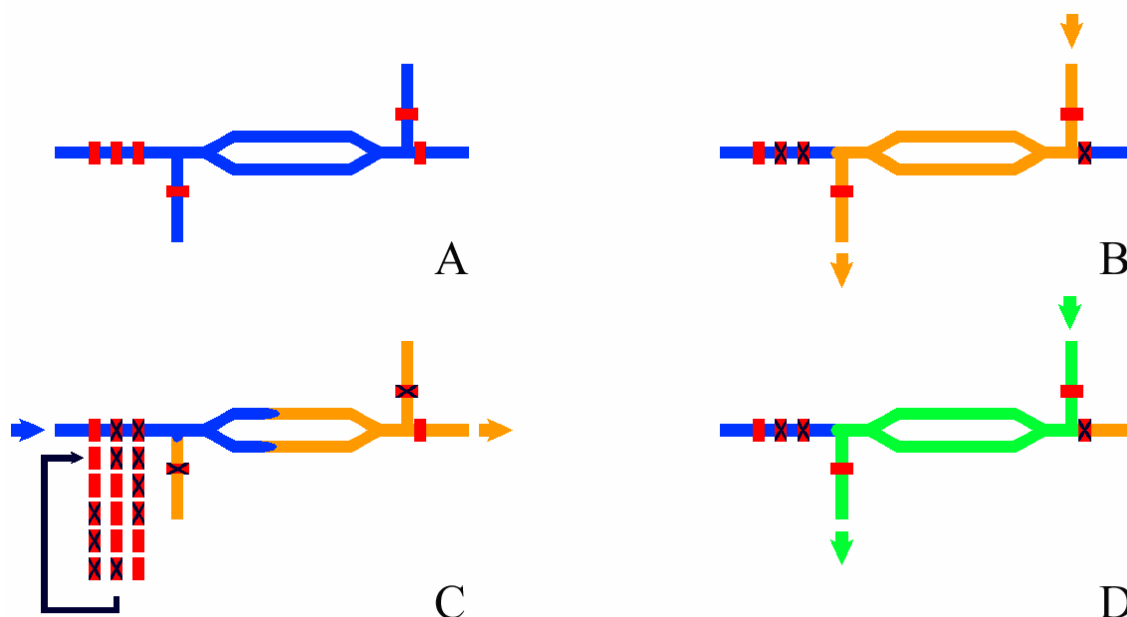
Figure 7: Positive displacement cross-injection (PCI) for robust and programmable high-precision dispensing on chip. **(A)** Schematic of a four port PCI junction. The split-channel architecture creates a larger volume injector region, thereby allowing for an increased number of injections before recharging. **(B)** Charging of the injector region of the pci junction. Junction valves are actuated to direct the flow vertically through the

junction, filling the injector region. **(C)** Precise positive displacement metering by actuation of peristaltic pump valves in pumping sequence. **(D)** PCI junction is sequentially charged with different solutions to create complex multi-component mixtures.

Certain applications may require the parallel injection of reagents into an array of reaction chambers containing different reagents/cells/bacteria. An array of five PCI junctions is shown in Figure 8A. The corresponding junction valves of all gated cross-injection junctions are interconnected, allowing an entire injection array, potentially of hundreds of junctions, to be controlled using only two control lines. The channel sections contained between the rightmost horizontal gate valves, and the peristaltic pump, define 5 reaction chambers, each having a volume of 2.6 nL. To execute the metering task the flow is first directed vertically, charging the junctions (Figure 8B). The flow is then directed horizontally through the junctions, and the peristaltic pump advances the fluid in the horizontal direction, injecting an even aliquot of sample into each reaction chamber. By operating the peristaltic pump at low frequency so that the response is linear, the amount of injected fluid is independent of the fluidic resistance of the channels. Figure 8C shows the even injection of sample solution into 5 reaction chambers of unequal fluidic resistance, and containing fluids of differing viscosity. For a similar pressure-driven injection, shown in Figure 8D, the flow through middle chamber leads that of the adjacent chambers due to the lower fluidic resistance and viscosity.
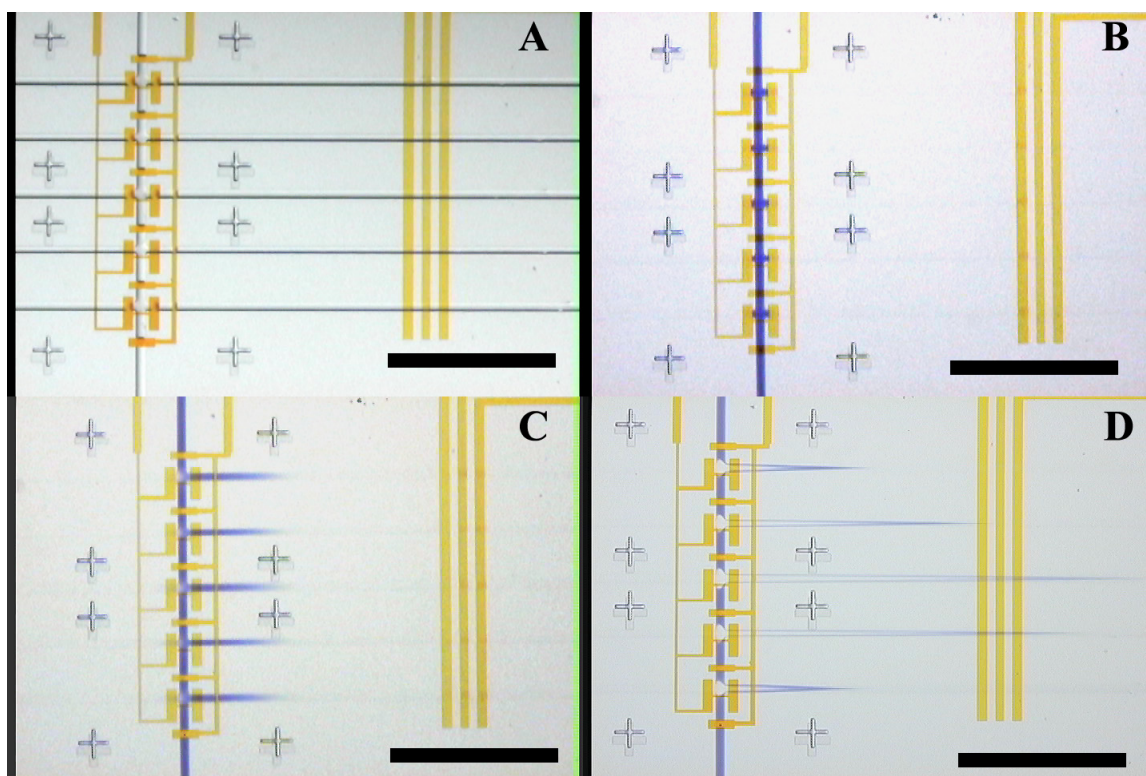
Figure 8: Parallel array of PCI junctions. **(A)** 5 PCI junctions controlled in parallel by 5 control lines. **(B)** Flow is directed vertically to charge PCI junctions with blue dye (10 mM bromophenol blue sodium salt). **(C)** Even injection of dye down 5 channels of varying fluidic impendence using peristaltic pump. Length of channels to outlet is (top to bottom) 2.5 mm, 1.5 mm, 1 mm, 1.5 mm, 2.5 mm. **(D)** Uneven pressure-driven injection of dye down channels due to varying fluidic impedence. Scale bars are 2mm.

Repeating the injection sequence allows for the volume of injected solution may be increased in discrete steps, so that programmable and quantized control of the final sample concentration is realized. Once the correct volume has been dispensed, the fluids are contained, and allowed to mix by diffusion. Absorption measurements for five adjacent reaction chambers of varying fluidic resistance and viscosity are shown in Figure 9. All

five data sets show excellent linearity, having r^2 values between .980 and .996. The average slope was determined to be 103 pL / injection, with a standard deviation of 6%, and a maximum deviation of 9%.
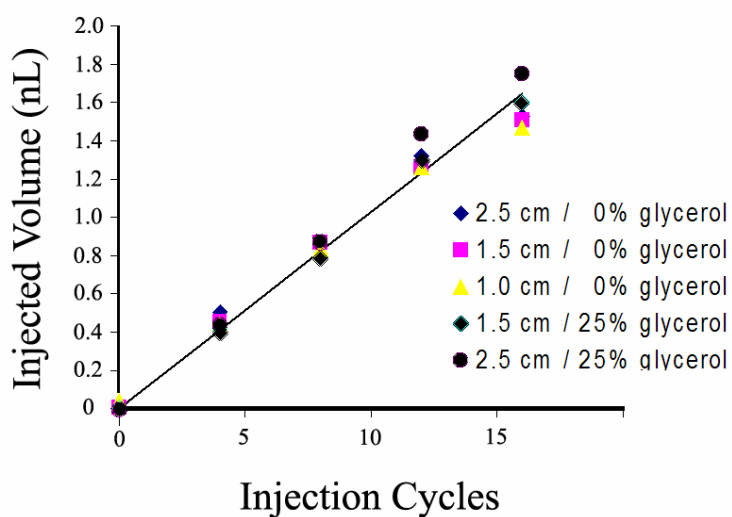
Figure 9: Absorption measurements of parallel metering using and array of 5 PCI junctions. Volume of injected dye (10 mM bromophenol blue sodium salt, TRIS·HCl pH8.0) is insensitive to changes in solution viscosity and fluidic impendence.

Chapter 3

MICROFLUIDIC FREE INTERFACE DIFFUSION: OPTIMAL MIXING

Introduction

The crystallization of a biological macromolecule is realized by the manipulation of one or more chemical and thermodynamic variables such that the solubility of a target molecule in a concentrated solution is reduced, thereby promoting a transition to the solid phase in the form of a well-ordered crystal. In principal a stable protein solution may be brought to a state of supersaturation through the manipulation of any physical parameter that appears in the thermodynamic equation of state of the protein. This is typically accomplished through the addition of precipitating agents that lower the solubility of the protein (often accompanied by a slow concentration of the solution). Traditional precipitating agents include salts, polymers, organic solvents, buffers, and various additives. When successful, these reagents promote specific protein-protein interactions by modifying solution properties such as pH, dielectric constant and ionic strength.

Natural macromolecule targets for crystallography are both large and extremely varied. Proteins, for example, are complicated polymers of amino acids with polar, non-polar, charged, and aromatic residues that interact with each other and with the external environment. These complicated interactions result in a highly varied and complicated phase-space diagram that cannot be deduced *a priori*. Consequently, macromolecular crystallization requires a brute force approach in which as large a volume of chemical phase-space as possible must be explored. The vastness of phase-space that must be

explored implies that a thorough investigation by conventional techniques is impractical. The initial search is therefore typically directed towards a sparse matrix or incomplete factorial sampling of likely crystallization agents (15, 34).

For macromolecules possessing a large volume of phase-space that is conducive to crystallization, there is a good chance that one of the randomly screened conditions will result in crystal formation. Since the first 'hit' is not likely to be optimal, initial successes are usually of poor quality, and may consist of spherulites (Figure 10A), phase separation (Figure 10B), micro-crystals (Figure 10B), needles, needle clusters, thin plates (Figure 10C), plate stacks (Figure 10D), or small single crystals (Figure 10E).   These starting conditions can be used to initiate focused and refined screening, eventually producing diffraction quality crystals (Figure 10F). If only a very narrow range of conditions is conducive to crystallization, initial screens may be too coarse to uncover promising conditions and further screening may be required.   For macromolecules that require very specific crystallization conditions, almost invariably the ones of greatest interest to the investigator, many thousands of experiments may be required before a hit is detected, if at all.
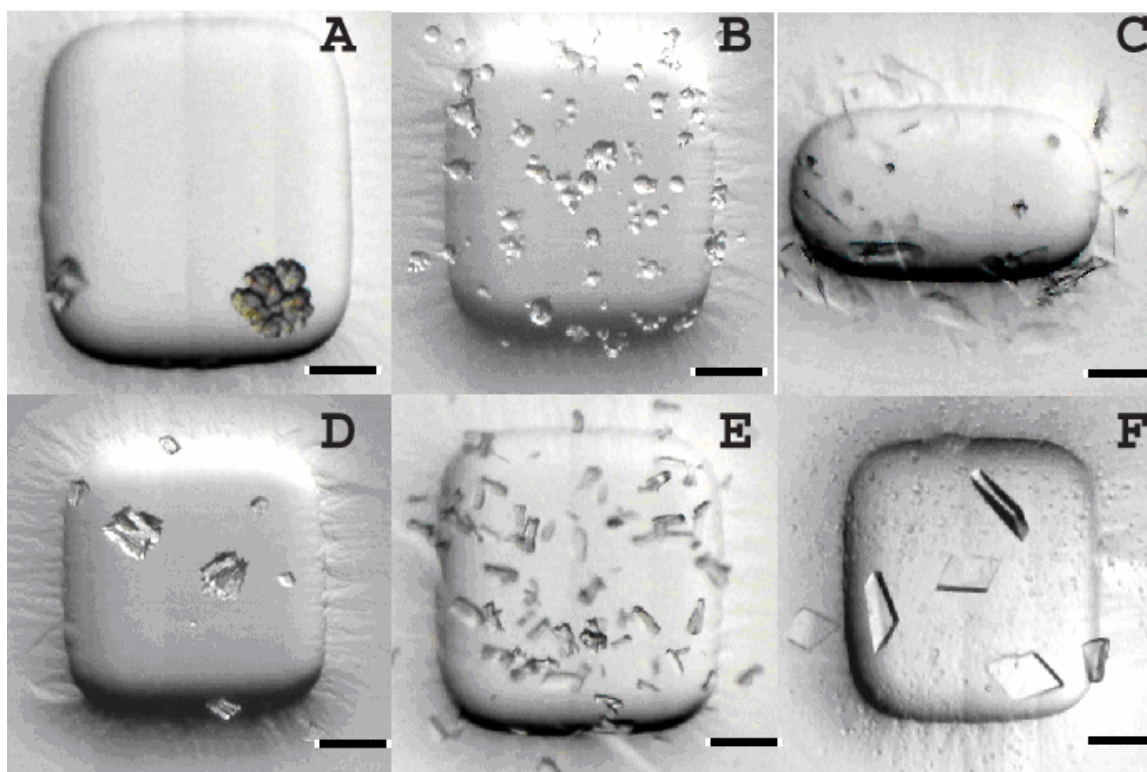
Figure 10: Examples of initial crystallization hits from a single on-chip screening experiment of a type II topoisomerase ATPase domain/ADP; 12 mg/mL. **(A)** Irregular spherulite. **(B)** Phase separation and spherulites with nucleating microcrystals. **(C)** Thin plate clusters. **(D)** Thick plate stacks. **(E)** Well-formed microcrystals. **(F)** Large single crystals. All scale bars are 100 μm.

Moreover, many important crystallization targets are only available in very small quantities. The large number of experiments required to uncover successful crystallization conditions therefore is what represents the most formidable obstacle to determining the structure of many important biological macromolecules. For example, membrane proteins play a central role in cell signaling and are often excellent targets for small molecule therapeutics. Unfortunately, the structures of only a very few (approximately 50) have

been determined to date, primarily because of the difficulties associated with expressing, solubilizing and stabilizing these molecules in the large quantities required for crystallization trials (> 1 mg) (35-37). Similarly, many proteins work in the cell as large complexes. Structural information of these targets provides invaluable information regarding complex biochemical reactions and protein/protein interactions. As with membrane proteins these assemblies are exceedingly difficult to purify in large amounts, and at times must even be purified by processing kilogram quantities of native sources (38, 39).

Traditional techniques for the crystallization of macromolecules include concentration through slow dehydration (vapor diffusion), batch and dialysis methods, and both liquid-liquid and liquid-gel diffusion experiments (For review see [40]). Practical limitations of traditional fluid handling approaches require that the minimum volume per assay for these techniques ranges from 0.2 μL to 1 μL for vapor diffusion and microbatch methods, and up to 50 μL for micro-dialysis. Since protein samples may only be available in milligram quantities, and target molecule concentrations are generally required in excess of 10 mg/mL, the ability to routinely perform nanoliter scale assays using microfluidics not only helps to promote a more comprehensive screening strategy, but further allows for experimentation with ultra-low-abundance macromolecules.

The probability of success in a crystallization screening experiment is proportional both to the number of independent trials, and to the chance of success of each trial. An optimal screening methodology must therefore maximize not only the number of independent trials

through small volume sample processing, but also the efficiency of each assay. Although the appropriate chemical variables cannot be ascertained in advance, it is possible to use the universal phase properties of the precipitant-protein interaction to systematically design experiments with optimal mixing kinetics, and thereby enhance the chance of crystal growth. In addition to the impressive economy of scale provided by microfluidic devices, the physical properties of fluid flow at the micron scale allow for the implementation of highly efficient crystallization assays.

Characteristic Energies of Nucleation and Growth

The successful crystallization of a macromolecule is determined both by thermodynamic and kinetic considerations. A concentrated solution of the target molecule must first be brought to a state in which the crystal phase is energetically favorable, and then kept in this state to allow crystal nucleation and growth to occur. An essential feature of crystal nucleation and growth is that it is necessarily a non-equilibrium process. A measure of how far out of equilibrium a system is, and therefore of the tendency towards crystallization, is the saturation defined as C/C_0, where C is the concentration of protein and C_0 is the maximum concentration of protein in thermodynamic equilibrium. By definition, saturation below unity describes a stable protein solution in which no phase change will be observed. All supersaturated solutions (S > 1) are unstable and will ultimately exhibit a phase transition to an amorphous or crystalline state. An emerging crystalline phase will continue to grow at the expense of the soluble phase until the concentration of soluble protein is reduced to C_0 and the chemical potentials of both phases

are equal. In equilibrium, the probability of observing a solution with concentration C is given by the Boltzman distribution as

$$\frac{C}{C_0} = Exp\left(-\frac{\Delta G}{KT}\right),$$ (1)

where ΔG is the Gibbs free energy of the solution relative to that of the solution in equilibrium with the crystalline phase. The chemical potential is identically the number specific Gibbs free energy of an ensemble so that taking the log of this expression gives the chemical potential of the crystalline phase relative to equilibrium as (41)

$$\mu = -KT \ln\left(\frac{C}{C_0}\right).$$ (2)

Thus, if the protein concentration in solution is greater than C_0, the crystal is energetically favored and will continue to grow.

Favorable interactions with neighboring molecules compensate for the net loss of entropy associated with incorporating a protein molecule into the growing lattice. On the surface of a growing crystal these interactions are incomplete, giving rise to an unfavorable surface term. The net free energy of a crystalline aggregate is therefore given by

$$G = -\frac{KTV}{\upsilon} \ln\left(\frac{C}{C_0}\right) + \sigma S,$$ (3)

where S is the surface area of the growing aggregate, σ is the surface energy crystal/solvent interface, V is the volume of the aggregate, and υ is the volume occupied by a protein molecule in the crystal. A hypothetical plot of the free energy of a growing nucleus as a function of radius is shown in Figure 11. The competition between the surface and volume terms gives rise to a finite activation barrier. Only after an aggregate achieves a critical radius does it become stable.
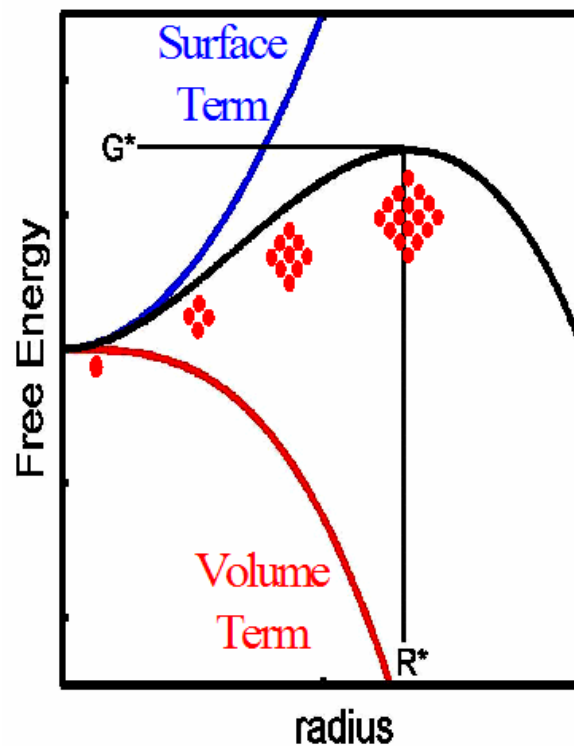
Figure 11: Activation barrier to crystal nucleation. Competition between favorable volume interactions and unfavorable surface interactions results in a minimum critical nucleus radius R^* that is stable.

If the critical radius is large compared to the size of each protein molecule, the growth of the nucleus can be well approximated as a continuous process. In this limit the nucleation process can be modeled as thermal activation of a quasiparticle over an energy barrier of height G^*, with a rate given by Kramer's relation (42):

$$J = K_0 Exp\left(-\frac{G^*}{KT}\right), \tag{4}$$

where J is the expected number of nucleation events per second per unit volume. The prefactor K_0 may be loosely interpreted as the escape attempt rate of a quasi-particle oscillating in the potential well near the activation barrier, and is therefore determined by the curvature potential in the vicinity of the soluble state minimum, the curvature near the transition state (critical nucleus), and is proportional to the concentration of molecules in solution.

An expression for the activation barrier, and hence the dependence of the nucleation rate on the degree of solution saturation may be deduced if an assumption is made as to the shape of the growing aggregate. For the case of a spherical aggregate the activation barrier may be expressed as (43)

$$J = K_0 Exp\left(-\frac{16\pi\upsilon^2\sigma^3}{3KT(KT\ln(C/C_0))^2}\right). \tag{5}$$

The very strong dependence of the nucleation rate on saturation is illustrated in Figure 12. By defining a characteristic reaction volume V_{exp}, and a relevant experimental timescale τ,

the rate of nucleation may be used to classify a supersaturated solution into one of two regimes. An average time to nucleation $1/(J\ V_{exp})$ that is much longer than τ defines the metastable regime. In this regime the growth of large, high-quality crystals is supported but nucleation events are rare, requiring impractically long incubation times. Experiments that stay in this region will likely appear as clear drops and will be unremarkable. It is worth noting that since the average time to nucleation scales with the volume of the reaction, small volume crystallization formats must achieve higher levels of supersaturation for crystals to be observed in reasonable times.
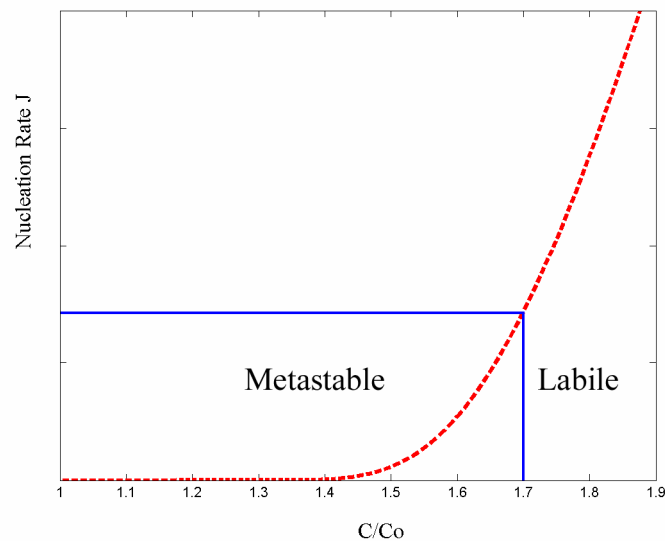
Figure 12: Nucleation rate of a spherical aggregate as a function of solution saturation.

Systems in which the average time to nucleation $1/(J\ v)$ is much shorter than τ are said to be in the labile regime. In this regime multiple nucleation events will be observed in time τ. Polycrystalline aggregates and high levels of defect incorporation are characteristic of rapid crystal growth in the labile regime (44). Furthermore, very high levels of supersaturation

often result in showers of microcrystals that may be too small to distinguish from amorphous precipitate, a problem that can cause promising conditions to be overlooked.

In conventional macromolecular crystallization a stable protein sample is brought into a state of supersaturation through the addition of a crystallizing agent. This process is represented as a deformation of a free energy landscape defining a crystalline and a soluble phase (Figure 13), where the aggregate radius has been replaced by a generalized reaction coordinate that encompasses all degrees of freedom in the system. Initially the protein sample is stable in the soluble form, having a free energy below that of the crystalline phase (Figure 13A). Perturbation of the system through the addition of a precipitating agent that lowers the solubility of the protein induces a state of supersaturation in which the energy of the soluble phase rises above that of the crystalline phase. If the degree of supersaturation is small this will result in a metastable state characterized by a large activation barrier (Figure 13B). If a higher degree of supersaturation is achieved, say through the addition of more precipitating agent, a labile state conducive to crystal nucleation is achieved in which the activation barrier has been substantially reduced (Figure 13C).

The three-dimensional aggregation of target molecules into a critical nucleus from which crystal growth may proceed is a process that requires a higher activation energy, and hence higher supersaturation, than the subsequent one- or two- dimensional nucleation needed for crystal facet growth. For this reason, an optimal crystal growth scheme should allow for

initial nucleation by transiently high levels of supersaturation followed by passage into lower supersaturation levels that support high-quality crystal growth (Figure 13D) (44, 45).
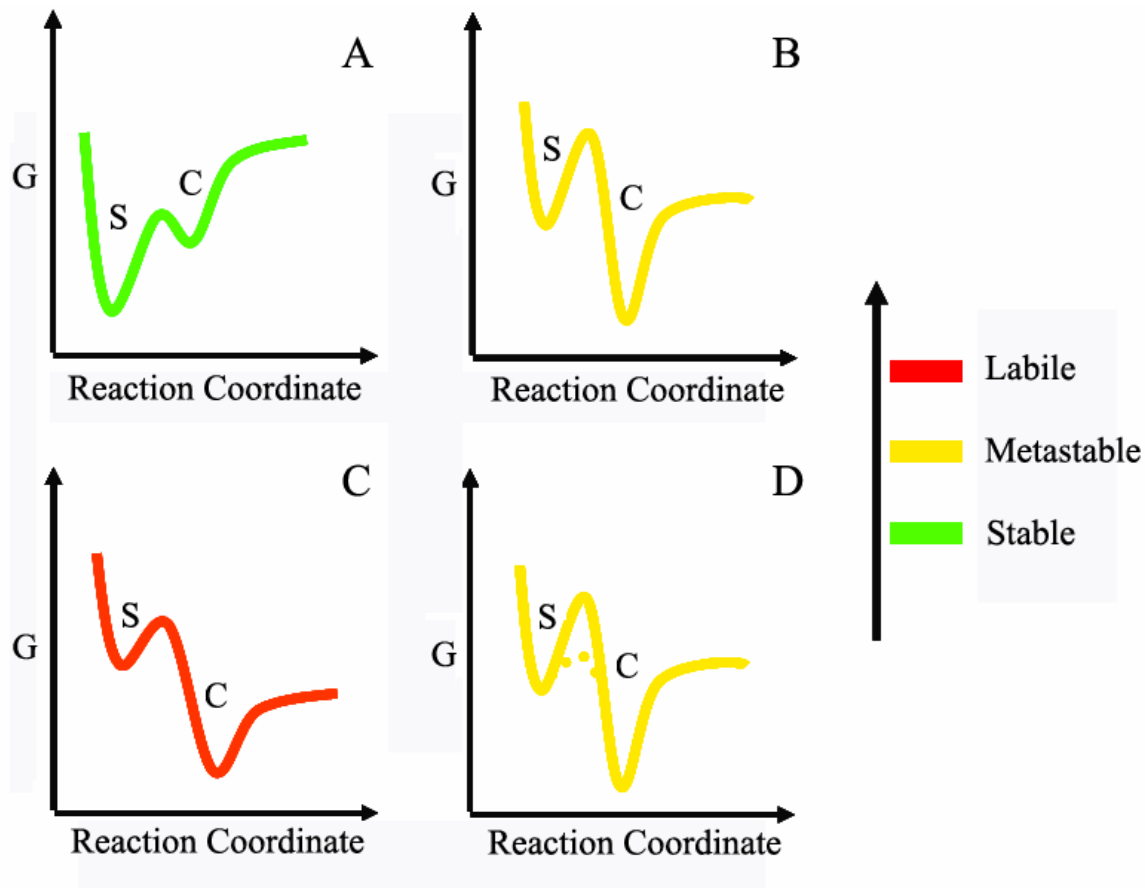
Figure 13: Hypothetical free energy diagrams characteristic of different regimes of solution saturation. **(A)** Stable regime. The soluble phase "S" has lower free energy and is stable. **(B)** Metastable regime. Growth of crystalline phase "C" is favored but nucleation events are rare due to large activation barrier. **(C)** Labile regime. A small activation barrier leads to rapid nucleation events and poor quality growth. **(D)** Metastable regime after nucleation. Activation barrier is reduced due to the presence of a critical nuclei in solution. High-quality crystal growth is supported.

Mixing at Low Grashoff Number

In the thermodynamic limit of infinite equilibration time, and with other thermodynamic variables held constant (i.e. pressure and temperature), the phase of the protein solution will be uniquely determined by the concentration of protein and precipitating agent in solution. This behavior may be represented by a hypothetical two-dimensional phase-space having concentration of protein and concentration of precipitating agent as variables. This phase-space represents the interaction of a given protein with a specific precipitating solution, and is therefore unique to that solution. Complex phase-space behavior arising from interactions such as specific protein/ligand interactions, protonation/deprotonation of amino acids, detergent micelle formation, and protein denaturation, results in highly varied and unpredictable phase behavior. The different phases that may exist within a single phase diagram include monomeric soluble phase, aggregate soluble phase, condensed liquid phase, amorphous aggregate, denatured protein, and various crystalline forms.

In the simplest non-trivial case there will exist at least two distinguishable phases: a soluble phase and a solid phase. At low protein and low precipitant concentrations the soluble phase is stable. This region is bounded by a solubility curve that determines the maximum stable concentration $C_0(C_{prec})$ of protein as a function of the precipitating agent concentration, which by definition must be single valued. For precipitating agents that have the potential to induce crystallization there exists a metastable region located just above the solubility curve. In this region the protein solution is out of equilibrium, and given sufficient time, will undergo a phase transition to a crystalline solid. Beyond the

metastable region, at higher protein and precipitant concentrations, lies the labile region where the nucleation of crystalline or amorphous aggregates is a rapid process. The boundary between these regions, which depends on the relevant timescale of the experiment, is referred to as the precipitation curve.

The equilibration of a crystallization assay can thus be represented as a parametric plot through phase-space, having time as the independent variable. It is instructive to examine the phase-space evolution of the two most commonly used crystallization screening formats, microbatch and vapor diffusion (Figure 14). In microbatch crystallization the protein is mixed at a one to one ratio with a precipitating agent and then incubated under a layer of immiscible oil. The immiscible oil prevents dehydration/concentration of the drop so that a microbatch experiment samples only a point of phase-space.
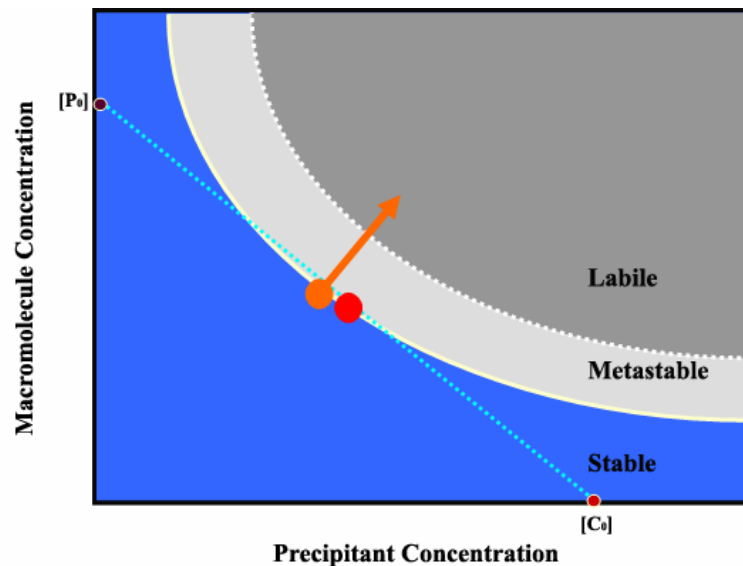
Figure 14: Schematic diagram of the evolution of hanging drop and microbatch experiments through a two-dimensional phase-space having macromolecule concentration and precipitating agent concentration as variables. The phase-space is divided into Stable, Metastable, and Labile regions. In microbatch experiments incubated under an immiscible oil (1:1 mixing ration) are represented as a single point (red) on the bisection of a tie-line connecting the initial protein concentration (P_o) and precipitant concentration (C_o). Hanging drop experiments allow post-mixing equilibration through vapor diffusion with a large reservoir of precipitating agent, slowly concentrating the reagents, and driving the sample into the super-saturation region (orange). Depletion of protein due to precipitation or crystal growth is not included in the figure.

In vapor diffusion experiments the protein and precipitant solutions are initially mixed at a one to one ratio, and are then suspended over a large reservoir of the concentrated precipitant solution. The drop subsequently equilibrates with the reservoir through a process of vapor diffusion until the vapor pressures of the drop and the reservoir are equal. This results in a monatomic concentration of the drop over time. This evolution is represented by an upward arrow in phase-space (orange).

Microbatch and vapor diffusion methods exhibit phase trajectories that are stagnant or monotonically increasing in supersaturation. The point sampling behavior of microbatch experiments results in an inefficient sampling of phase-space when compared to vapor diffusion which allows for a continuum of conditions to be explored through drop evaporation. However, the monatomic increase in both protein and precipitant

concentration does not provide the desired transiently high levels of supersaturation for nucleation followed by regression to the metastable regime for high-quality crystal growth. Furthermore, in microbatch or hanging-drop experiments, the sudden addition of the precipitating agent to the protein sample induces rapid convective mixing resulting large transient concentration gradients throughout the drop. The corresponding high levels of supersaturation that occur at the fluid/fluid interface often result in the immediate and irreversible precipitation of the protein.

As an alternative to microbatch and vapor diffusion formats, the technique of free interface diffusion (FID) allows for both slow and controlled mixing and efficient phase-space evolution. In conventional FID experiments a liquid/liquid interface is established between the protein and precipitant solutions in a capillary tube (top of Figure 15).

As the reaction begins, a slow equilibration of the molecular species across the interface occurs by diffusion. Each species present in the reaction equilibrates at a rate determined by its diffusion constant. The diffusion constant of a particle may be approximated through the Stokes-Einstein relation:

$$D = \frac{KT}{6\pi\eta r} \quad , \qquad\qquad (6)$$

where η is the solution viscosity in kg/ms, and r is the hydrodynamic radius of the particle. The inverse dependence of the diffusivity on radius implies that small molecule precipitating agents will equilibrate much faster than larger protein molecules. For

example, a salt ion with a radius of 1 Å has a diffusion constant in water of approximately 1000 μ^2/s. By comparison a typical protein molecule of radius 10 nm will have a diffusion constant of 10 μ^2/s. The counter-diffusion of analytes with different diffusion constants along a capillary of constant cross section results in a complex spatial-temporal evolution of the concentration profiles (Figure 15) (46, 47).
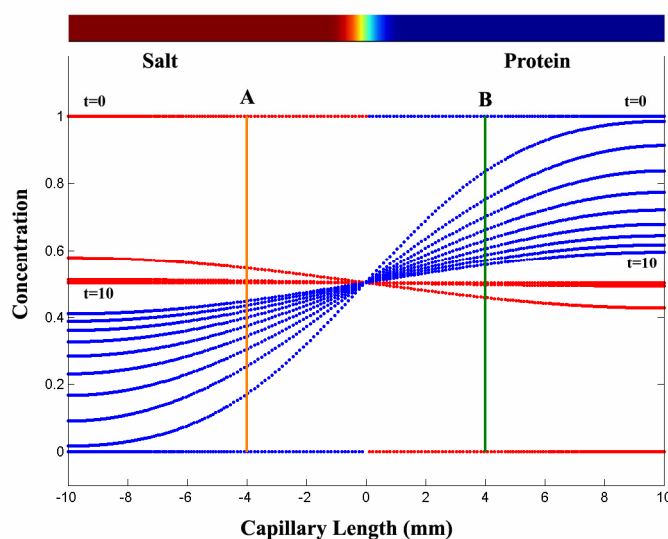
Figure 15: Conventional FID reaction. (top) Protein (blue) and salt (red) solutions are brought into intimate contact at a fluid-fluid interface within a capillary of constant cross section. (bottom) Evolution of protein (blue) and salt (red) concentration profiles due to counter-diffusion of species across the interface. Diffusion constants of salt and protein are taken to be 1000 μ^2/s and 10 μ^2/s respectively. Concentration profiles are shown at even 1 day time intervals from t = 0 days (step function) to t = 10 days.

Let us consider two observation points, A and B, located some fixed distance on either side of the interface (Figure 15). Shortly after the reaction commences the protein concentration at point A changes very little, while that of the precipitating agent, which typically has a much larger diffusion constant, increases towards the final concentration determined by initial the mixing ratio. Subsequently, over a larger timescale, the protein concentration equilibrates, decreasing towards the final protein concentration that is again determined by the mixing ratio. The concentration profile at point A therefore travels a curved path through phase-space, potentially sampling efficient crystal nucleation conditions in the labile region prior to settling into a high-quality growth regime in the metastable region. As the solutions homogenize, the evolution at point B follows a complementary trajectory to A, ultimately converging to the same final state (Figure 16).
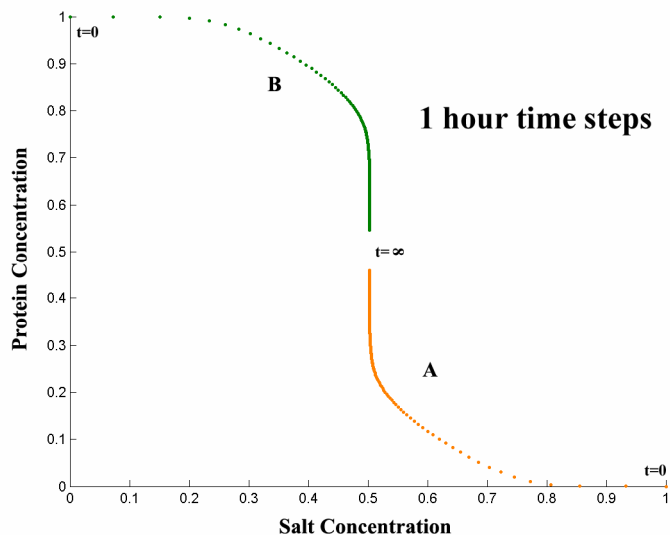
Figure 16: Phase-space evolution of FID reaction at two observation points (Figure 15) equidistant from the fluid-fluid interface. Points represent even 1 hour time steps from t = 0 hours to t = 240 hours.

Free interface diffusion has long been recognized as an efficient means of detecting crystallization conditions that has distinct advantages over microbatch or vapor diffusion techniques (45). Despite the favorable kinetics of conventional free interface diffusion, this method has not been widely adopted in the protein crystallography community for a number of reasons. For example, conventional FID setups require that solutions be carefully introduced into opposite ends of the capillary using a thin needle. This is a delicate and labor-intensive technique making it illsuited to high-throughput screening. Moreover, the diameter of the capillary must be of substantial size (typically 1mm), necessitating the use of relatively large sample volumes (generally > 5 μL). Furthermore, the introduction of the second fluid causes transient convection, resulting in a poorly-defined interface which may only be reduced by cumbersome procedures such as the introduction of hydro-gels or the prior freezing of the first solution. The intrinsic drawbacks of large required volume, delicate dispensing, and poorly-defined interface have thus prohibited the use of FID as either a routine or large-scale automated screening technique.

Even when a well-defined fluidic interface can be created, buoyancy-driven convection, due to density differences in the solutions causes complex mixing at the interface. To avoid unwanted mixing, capillaries must be stored with the long axis parallel to gravity,

and with the more dense solution on the bottom. This configuration creates a stable fluidic interface, but often causes nucleated crystals to fall away from the interface and out of the optimal growth conditions. It has thus been proposed that free interface diffusion would only realize its practical advantages in microgravity environments were gravity-induced convection is eliminated (40, 48). However, the unusual properties of fluid flow in microfluidic devices make it both possible and practical to implement nearly ideal free interface diffusion conditions in terrestrial devices. The relevant non-dimensional number that governs the onset of convection in a closed fluidic system is the Grashof number (which measures the ratio of buoyant to viscous forces):

$$Gr = \frac{\alpha \Delta c g L^3}{v^2} \quad , \tag{7}$$

where α is the solutal expansivity (cm^3/mg), Δc is the difference in solute concentration (mg/cm^3), g is the acceleration of gravity (cm/s^2), L is the characteristic dimension of the container (cm), and v is the kinematic viscosity (cm^2/s).

At low Grashof number the interface between two distinct solutions brought into intimate fluidic contact is stable. Inspection of Equation 7 suggests that this condition may be achieved at high solution viscosity (49), in microgravity environments (50) or at small characteristic length scales. Space-born free interface diffusion experiments have been conducted in microgravity environments. These investigations have shown that stable fluidic interfaces are achievable and further suggest that crystals of increased perfection may be grown in microgravity (50, 51). However, the enormous expense of conducting

space-born experiments prohibits its use as a screening technique, so that investigation has been limited to well-characterized model proteins.

Artificially increasing the solutal viscosity through the addition of polymerizing hydrogels has been investigated as a technique for achieving low Grashof number mixing in terrestrial devices (49, 52). In particular, the gel-acupuncture method has been advanced as a method of realizing purely diffusive mass transport in crystallization assays. This method has been successful over a broad range of crystallization targets and has been used to produce high-quality crystals of novel crystallization targets. Despite this success, several limitations have prevented general use of this technique. In particular, this technique has not proved amenable to small volume, large-scale crystallization screening. Additionally, the requirement of including a polymerizing gel into the crystallization reagents presents an undesirable constraint on the chemistry. An optimal crystallization technique should allow for independent control over both the chemical composition and mixing kinetics.

The third power dependence of the Grashof number on the characteristic length suggests reducing the critical dimension of the reactor as a means to suppress convection and achieve purely diffusive mass transport. Five microfluidic reactors designed to provides exactly this property are shown in Figure 17. Microfluidic free-interface diffusion (μFID) through a constricted channel connecting two microwells allows for the slow counter-diffusion of the precipitant and protein solutions.
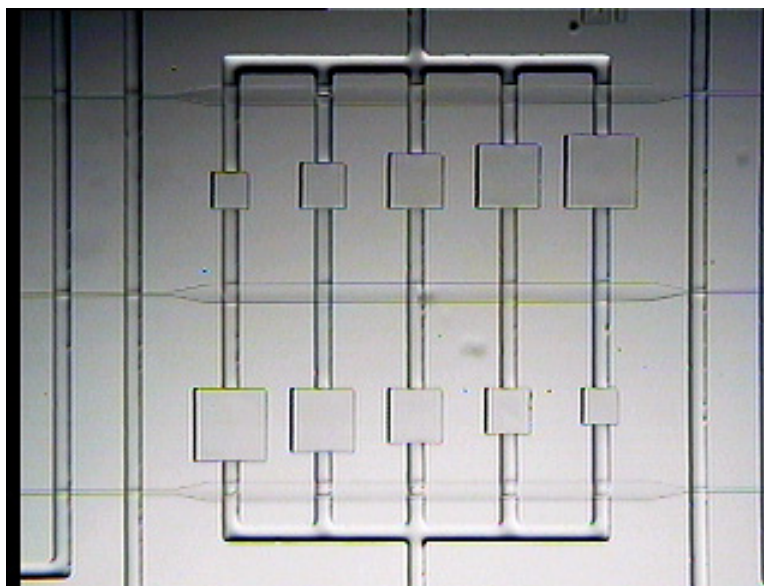
Figure 17: Microfluidic free interface diffusion (μFID) reactors. 5 pairs of microwells are designed to implement 5 simultaneous FID reactions at mixing ratios 4:1, 2:1, 1:1, 1:2, and 1:4. Total volume of each reactor is 10 nL.

In this configuration the final concentration of each reactor is determined by the relative volume of the coupled microwells. Opening the interface valve that separates the protein from the precipitating solution creates a well-defined fluidic interface that allows for diffusive equilibration of the coupled microwells. Due to the different mixing ratios the individual trajectories of each reactor fan out in phase-space, thereby providing efficient coverage of potential crystallization zones (Figure 18).
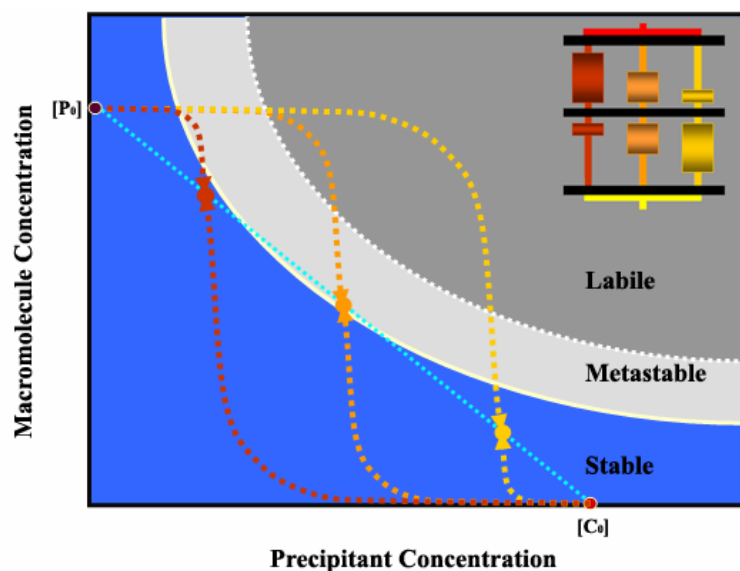
Figure 18: The evolution of 3 µFID reactions having mixing ratios 3:1, 1:1 and 1:3. Curves represent the average state of both the sample side (top) and precipitating agent side (bottom) of each compound well. The curves are representative of a counter-diffusion between Lysosyme and sodium chloride and agree qualitatively with numerical finite element simulations. A decrease in protein concentration due to precipitation or crystal growth is not included in the figure.

A further advantage of the constricted channel between the two wells is that only a very small fraction of the protein sample is exposed to large transient gradients that occur shortly after the interface is established. More concentrated precipitating solutions may therefore be used with negligible immediate precipitation so that higher levels of supersaturation may ultimately be achieved.

C h a p t e r   4

MICROFLUIDIC FREE INTERFACE DIFFUSION: SCREENING DEVICE

Parallel Implementation of μFID

The simple geometric metering architecture (Figure 17) allows for the facile implementation of nanoliter μFID crystallization assays in which the endpoint, and hence the trajectory through phase-space, may be accurately controlled. Furthermore, since this technique is robust to the properties of the resident fluid and does not require precise valve timing it is scaleable to massively parallel architectures. The robust and precise metering, simplicity of control, and highly efficient mixing kinetics of this technique have been used to implement a microfluidic screening device for protein crystallization in ultra-small volume reactions (Figure 19) (29). The current version of this device implements 240 simultaneous metering and mixing reactions while consuming only 3.0 μL of protein solution; this represents a reduction of approximately 100-fold in sample consumption when compared to traditional crystallization techniques.
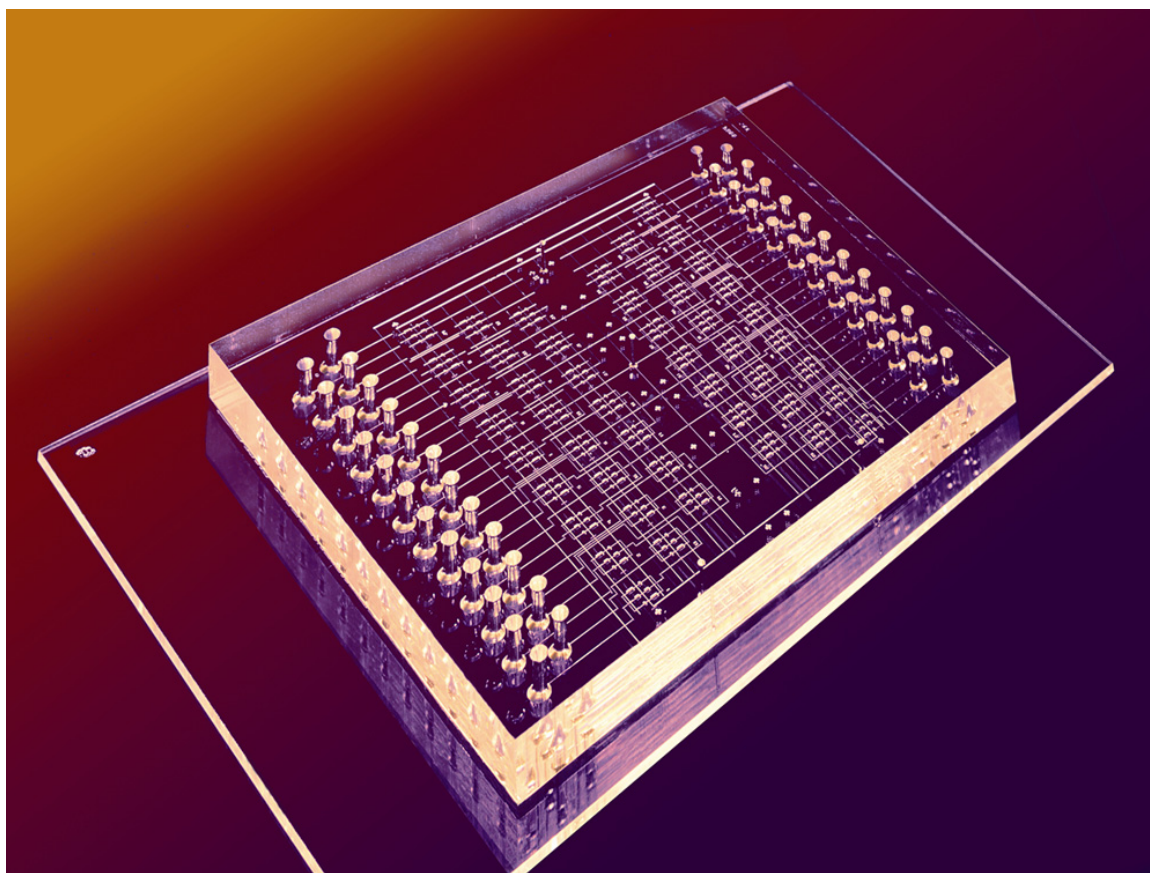
Figure 19: Microfluidic protein crystallization screening device.

A layout of the chip showing 48 reaction centers, each consisting of 5 μFID reactors with mixing ratios of 1:4, 1:2, 1:1, 2:1 and 4:1 is shown in Figure 20. Each pair of chambers is connected to the protein sample and one of 48 crystallization solution inlets. Parallel control of 720 integrated valves is achieved through two control lines that separately address 240 interface valves and 480 containment valves. By virtue of this parallel architecture the device may be used to simultaneously mix and meter 48 solutions of varying viscosity, surface tension, pH, and ionic strength at five different mixing ratios using only two hydraulic control lines.
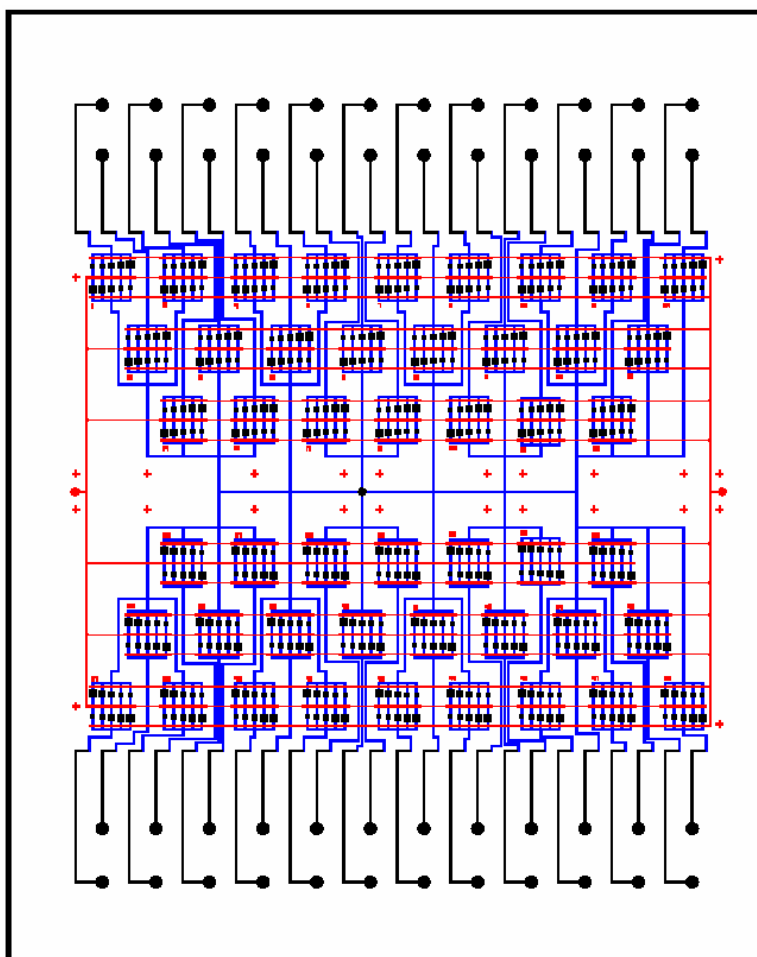
Figure 20: Layout of crystallization screening device. Flow layer is molded from a multilevel negative master having both 13 μm high flow channels fabricated from 5740 photoresist (blue), and 45-micron-high microwells and inlet channels fabricated from SU8 2050 resist (black). The high SU8 inlet structures prevent channel collapse during loading. Control structure (red) consists of two separately addressable networks for actuation of interface and containment valves. Forty-eight 4 μL reagent wells allow for direct loading of the crystallization reagents.

The chip is contained within a carrier device (Figure 21) that facilitates loading, storage, and interfacing with the control lines. The chip is secured in the base of the carrier with the interface line directly connected to one of two carrier interface pins that are externally accessible. The containment line interface pin is connected to the chip through a pressure accumulator. Once charged, this accumulator acts as an on-board pressure source to maintain actuation of the containment valves for several weeks, thereby allowing the chip to be stored and transported without the need for any external connections.
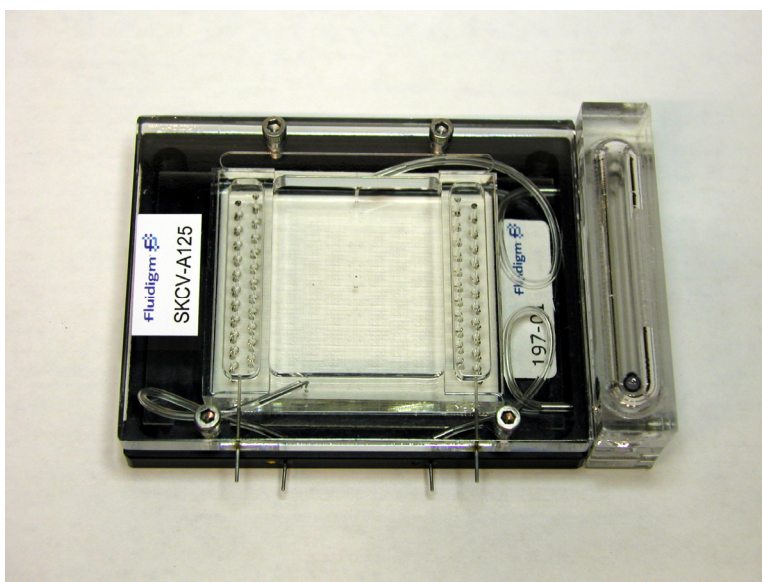
Figure 21: Crystallization chip inside carrier device. Pressure reservoir (right) allows for free transport and storage of chip. Interface pins (front) allow for easy loading and control of chip valves.

The top of the carrier has two cavities with a raised lip around their periphery and stainless steel input ports for pressurization. The cavities mate with the 48 reagent wells, creating a seal against the compliant elastomer chip when the plates are pressed together. 3 µL of each of the 48 crystallizing agents is introduced into the reagent wells of the chip using gel loading pipette tips (Figure 22). Since the crystallization reagents are loaded directly onto the chip there is no need for connecting 48 separate tubing connectors, greatly simplifying operation. Once the carrier is assembled the cavities are pressurized, simultaneously injecting the 48 crystallizing agents into the chip. The protein sample is then loaded through a single port located in the center of the chip. 4 µL of protein sample are aspirated into a pipette tip, and the tip is inserted into the protein port. The tip is then pressurized through an adapter, injecting the protein into the 240 reaction chambers. Since the sample is introduced through a single port, there is very little lost at the interface, and a true economy of scale is realized with more than two thirds of the sample being used in the crystallization assays.
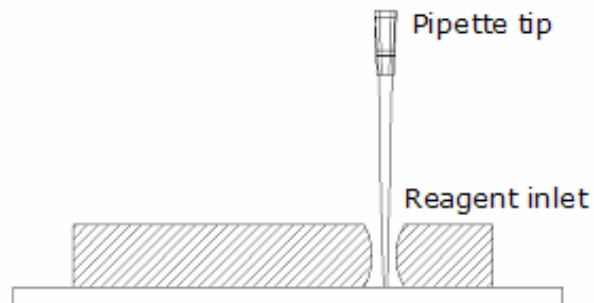
Figure 22: Loading of crystallization agents directly into reagent wells.

This device represents the first scaleable implementation of free interface diffusion in a format suitable for high-throughput structural biology initiatives. The ability to efficiently screen crystallization conditions in a small-volume format represents an enormous savings in the costs associated with upstream expression and purification processing. The modest requirements in peripheral fluidic hardware, small footprint, and simple operation make this device practical for use in both high-throughput crystallization facilities and in specialized academic labs. Furthermore, the inexpensive fabrication of these devices should be possible once adequate production technology is in place, making chip-based crystallization economical when compared to commercial liquid handling robots. It is hoped that this will democratize the field of structural biology, making small volume crystallization accessible to small academic laboratories.

Crystallization Results

An initial validation study of on-chip protein crystallization by μFID was conducted on 8 model macromolecules including 7 commercially available crystallization standards, (Lysosyme, Glucose Isomerase, Xylanase, Thaumatin, Protease K, Bovine Trypsin, and Beef Liver Catalase), and 1 protein with unpublished structure (bacterial primase catalytic core domain). The bacterial primase catalytic core domain was chosen since it had previously been extensively screened, and was known to be difficult to crystallize. Each protein was tested against two or more commercially available standard sparse matrices of precipitants. To compare crystallization in chip against standard crystallization methods, crystallization experiments were repeated for 9 of the model macromolecules using the

conventional microbatch and hanging-drop techniques; this allowed the precipitant chemistries to be kept constant while varying the kinetic scheme for crystal growth.

Crystal growth was observed in the chips for all model macromolecules tested, and showed an excellent degree of correlation with successful conditions revealed by more standard screening techniques.   Crystals of 6 different protein models grown in chips are shown in Figure 23. A histogram comparing the number of successful experiments obtained by each method for 8 model proteins (Figure 24) shows enhanced crystallization success in the chip-based experiments. Sparse matrix screens led to crystal growth more often in the chip than by conventional techniques in all but two cases (protease K and bovine trypsin). The large number of crystallization hits obtained for Protease K in microbatch experiments is difficult to explain on the basis of mixing kinetics since microbatch should be the least efficient assay format. Subsequent experimentation with a broad range of crystallization targets has shown this result to be anomalous – chip based crystallization screening has been found to generally produce more hits than conventional techniques.
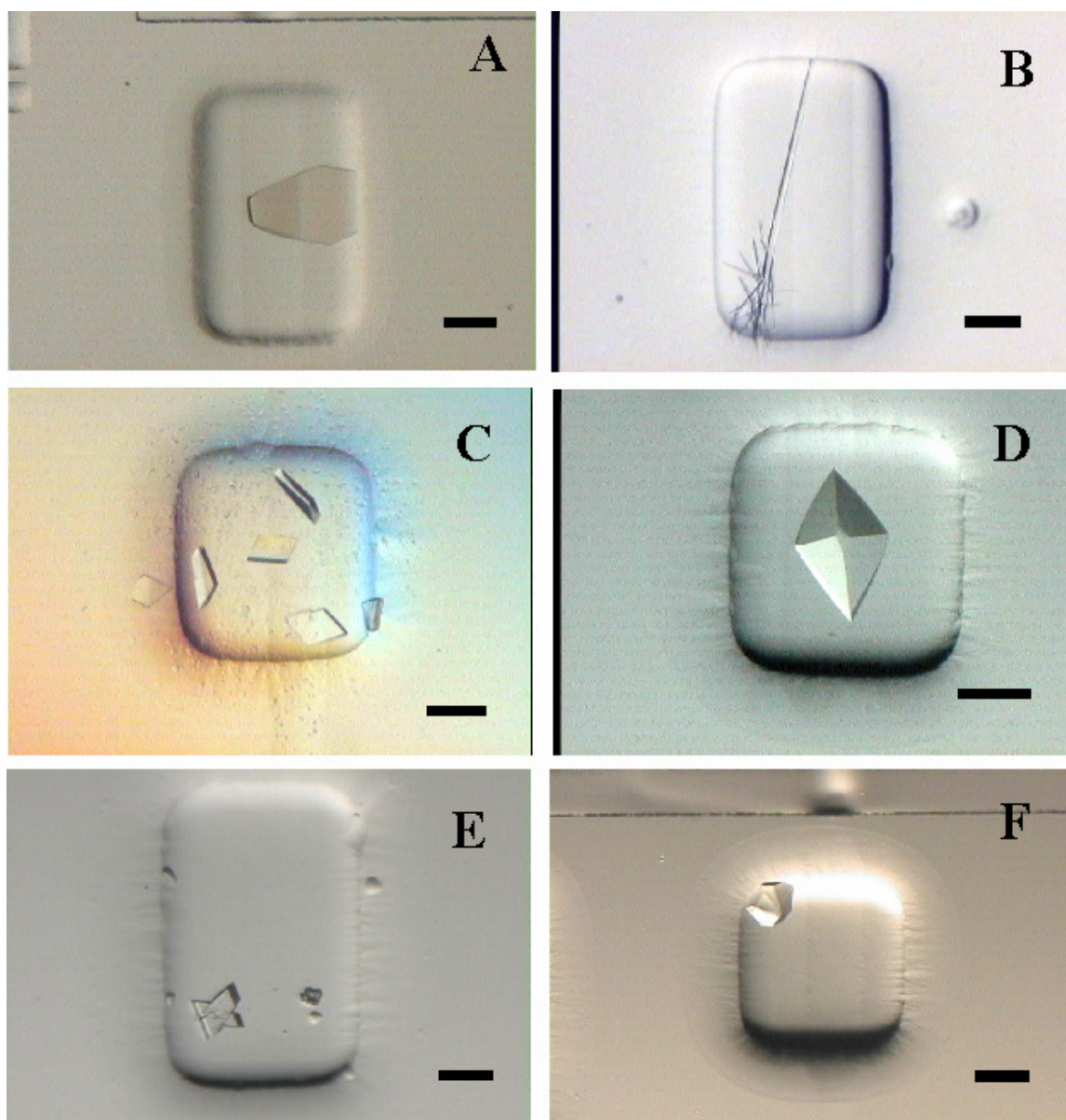
Figure 23: Optical micrographs of macromolecule crystals grown in chip. (A) Chicken Egg White Lysosyme (Sigma-Aldrich); 50 mg/mL in 0.2 M sodium acetate pH 4.7. Mixing ratio of 4:1 with 0.2 M Magnesium Chloride hexahydrate, 30% w/v iso-propanol, 0.1 M Hepes-Na pH 7.5. (B) Bacterial Primase catalytic core domain; 15 mg/mL in 50mM sodium chloride, 20mM TRIS-HCl pH 8.0, 1mM DTT. Mixing ratio of 4:1 with 1.4 M potassium/Sodium Phosphate pH 6.8. (C) Type II Topoisomerase ATPase

Domain / ADP; 12 mg/mL in 100mM sodium chloride, 20 mM TRIS pH 7.0. Mixing

ration of 1:1 with 0.2 M ammonium fluoride, 20% w/v polyethylene glycol 3350, pH 6.2.

(D) Thaumatin (Sigma-Aldrich); 50 mg/mL in 0.1 M ADA (Sigma Aldrich) pH 6.5.

Mixing ration of 1:1 with 0.8 M potassium sodium tartrate tetrahydrate, 0.1 M HEPES

pH 7.5. (E) Xylanase (Hampton Research); 43% w/v glycerol, 180 mM Na/K phosphate

pH 7.0. Mixing ratio of 4:1 with 0.2 M calcium chloride dihydrate, 28% v/v polyethelene

glycol 400, 0.1 M HEPES pH 7.5. (F)   Glucose Isomerase (Hampton Research) 31

mg/mL in 10 mM ammonium sulfate. Mixing ratio of 1:1 with 0.2 M calcium chloride

dihydrate, 28% polyethelene glycol 400, 0.1 M HEPES pH 7.5. Scale bars are 100 μm.

All scale bars are 100 μm.
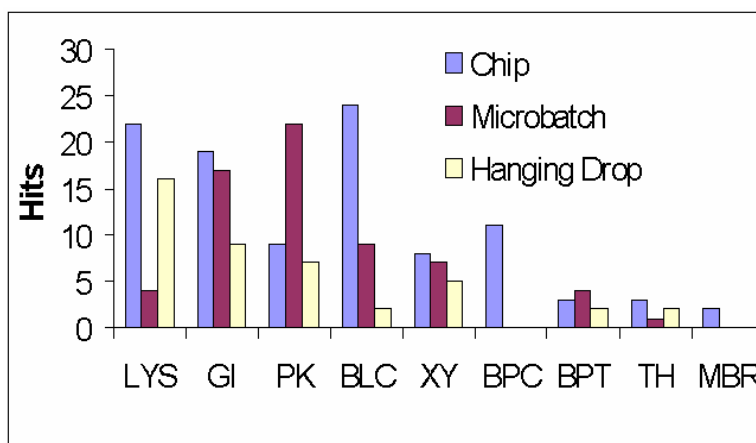
Figure 24: Histogram of crystallization hits for sparse matrix screens of model proteins.

Number of screens tested on each protein are Lysosyme (Lys) = 2, Glucose Isomerase (GI)

= 2, Protease K (PK) = 1, Bovine Liver Catalase (BLC) = 1, Xylanase (Xy) = 2, Bacterial

Primase catalytic core domain (BPC) = 3, Bovine Pancreas Trypsin (BPT) = 1, Thaumatin

(Th) = 1, mycobacterial RNase (MBR) = 3.

In the case of the bacterial primase catalytic core domain the chip-based experiments showed a dramatic improvement in success rate. μFID experiments identified 11 conditions that produced needle crystals of dimensions greater than 100 μm while no hits were observed in either macroscopic method. An additional on-chip experiment optimizing around the crystallization conditions identified from the initial screen produced crystals whose largest dimension exceeded 400 μm (Figure 23B). These conditions were subsequently transported to microbatch format. This example suggests that optimized on-chip crystallization conditions may be successfully exported to macroscopic techniques.

Finally, crystal growth in μFID experiments was generally observed to be faster than in microbatch or hanging-drop formats. For the type II topoisomerase ATPase domain crystal growth in microbatch required 2 weeks while crystals grown on chip with the same conditions appeared after only 4 hours of incubation. When crystals grew on chip in less than 12 hours, they were always observed on the protein side of the compound well, suggesting that the short crystallization times are due to the high degree of supersaturation achieved in the initial phase of diffusive equilibration.

In conventional screening formats reagents are generally mixed in a one-to-one ratio so that the influence of mixing ratio is rarely investigated. In chip based experiments different mixing ratios are set in parallel with no increase in setup time or complexity. In many cases protein/precipitant mixing ratio was found to be an important screening parameter, influencing both the success and morphology of crystallization. Figure 25 shows the

dependence of mixing ratio on the crystallization of a type II topoisomerase ATPase domain and of DNA B/C helicase complex.
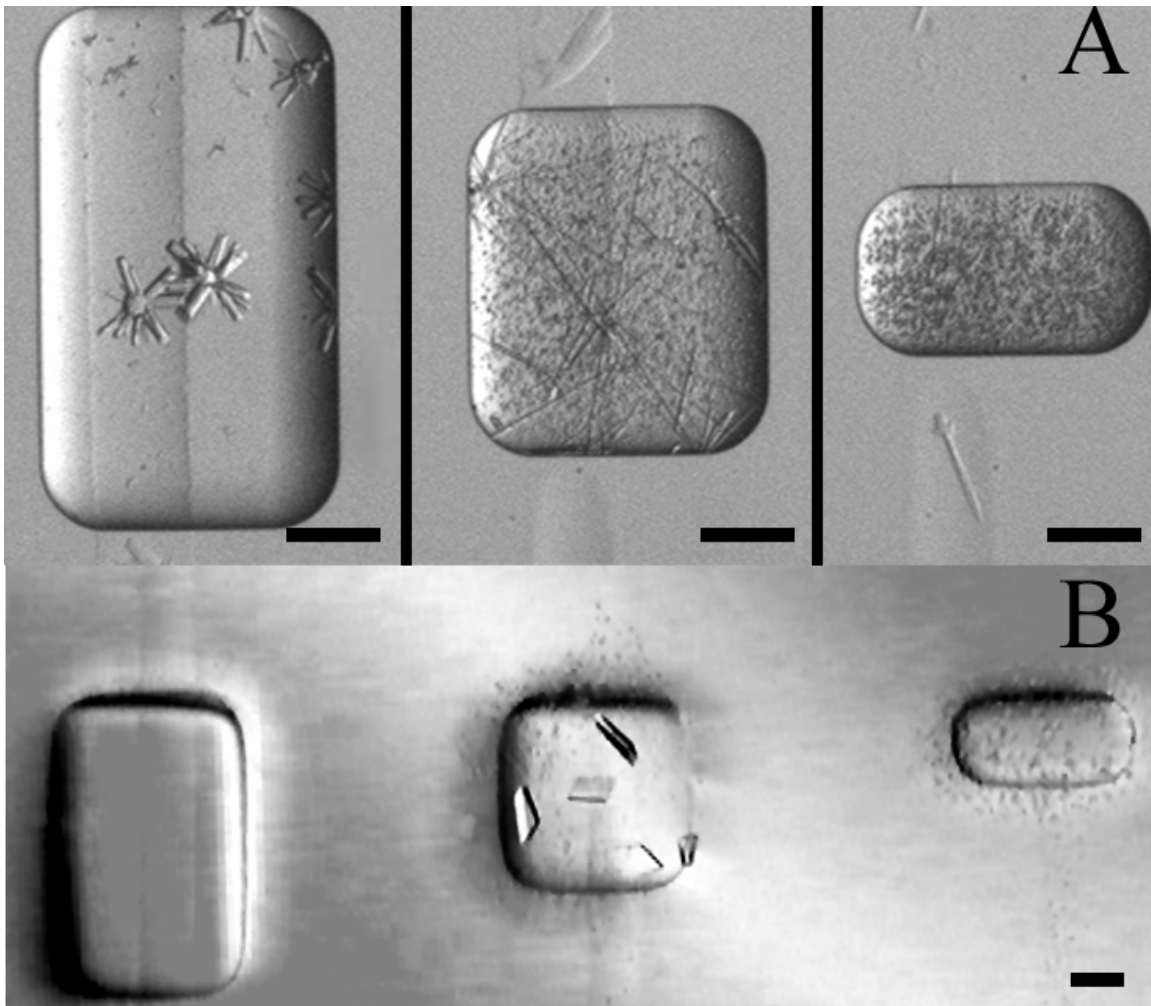
Figure 25: Variability in crystallization behavior due to different protein/precipitant mixing ratios. **(A)** Crystals of DNA B/C helicase; 14 mg/mL grown at 4:1 (left), 1:1 (center), and 1:4 (right) mixing ratios of protein sample with 2.0 M $(NH_4)_2SO_4$, phosphate-citrate pH 4.5. **(B)** Crystals of Type II Topoisomerase ATPase Domain / ADP; 12 mg/mL in 100mM sodium chloride, 20 mM TRIS pH 7.0. Mixing ratio of 4:1

(left), 1:1 (center), and 1:4 (right) with 0.2 M ammonium fluoride, 20% w/v polyethylene glycol 3350, pH 6.2. All scale bars are 100 μm.

Consistent with the localization of large initial concentration gradients to the relatively small volume of the connecting channel, μFID-based chip experiments resulted in reduced protein precipitation.   It was observed that the mixing ratios and concentration of crystallization agents that lead to crystallization on chip often caused the protein to immediately precipitate in hanging drop and microbatch experiments. In the case of a type II topoisomerase ATPase domain, the final concentration of precipitating agent achievable in chip was 4 times greater than that possible for microbatch.

Beyond experimentation with well-characterized crystallization standards the present technique has proven useful in the crystallization of outstanding and challenging macromolecule targets. During these trials, chip-based μFID reactions have been used to crystallize membrane proteins, large macromolecule complexes, and targets that had failed to produce crystals by conventional screening techniques.

The crystallization device has been used for the *de novo* crystallization of 3 targets (a type II topoisomerase, a transferring receptor heterodimer complexed with HFE (hdTfR/HFE), and 10 MDa vault protein assembly) that had not previously been successfully screened by conventional methods.   A single device was used to screen the topoisomerase protein against a commercially available sparse matrix screen (Hampton Crystal Screen I; Hampton Research). After 24 hours of incubation this screen identified 18 conditions that

gave crystals exhibiting varied quality and morphologies including some large single crystals (Figure 23C). Crystals obtained from 10 of these conditions were reproduced in microbatch format and were ultimately used to collect data at a resolution of 2 Å (53).

hdTfR/HFE is a complex of an engineering heterodimer of transferrin receptor mutants (hdTfR) and HFE, a protein implicated in hereditary hemochromatosis (54). The hdTfR/HFE complex was screened against 4 commercially available sparse matrix screens (Hampton Crystal Screen I, Hampton Crystal Screen II; Hampton Research, Wizard I, Wizard II; Emerald Biostructures), resulting in the identification of 3 conditions that gave rise to small (approximately 5 micron) plate clusters. Two rounds of subsequent optimization using systematic grid screens resulted in plate clusters and some single plates having maximum dimensions of approximately 50 microns (Figure 26A). It was determined that hdTfR/HFE crystallized only in a very narrow range of conditions, and in a specific protein/precipitant mixing ratio. Changing the concentration of precipitant (PEG MME 750) by as little as 1% from the successful condition (17% v/v PEG MME 750, 100 mM TRIS·HCl pH 7.6, 250 mM NaCl) did not produce crystals. Efforts to export these conditions to microbatch and hanging drop formats have thus far been unsuccessful despite highly resolved screening of precipitant and salt concentrations.
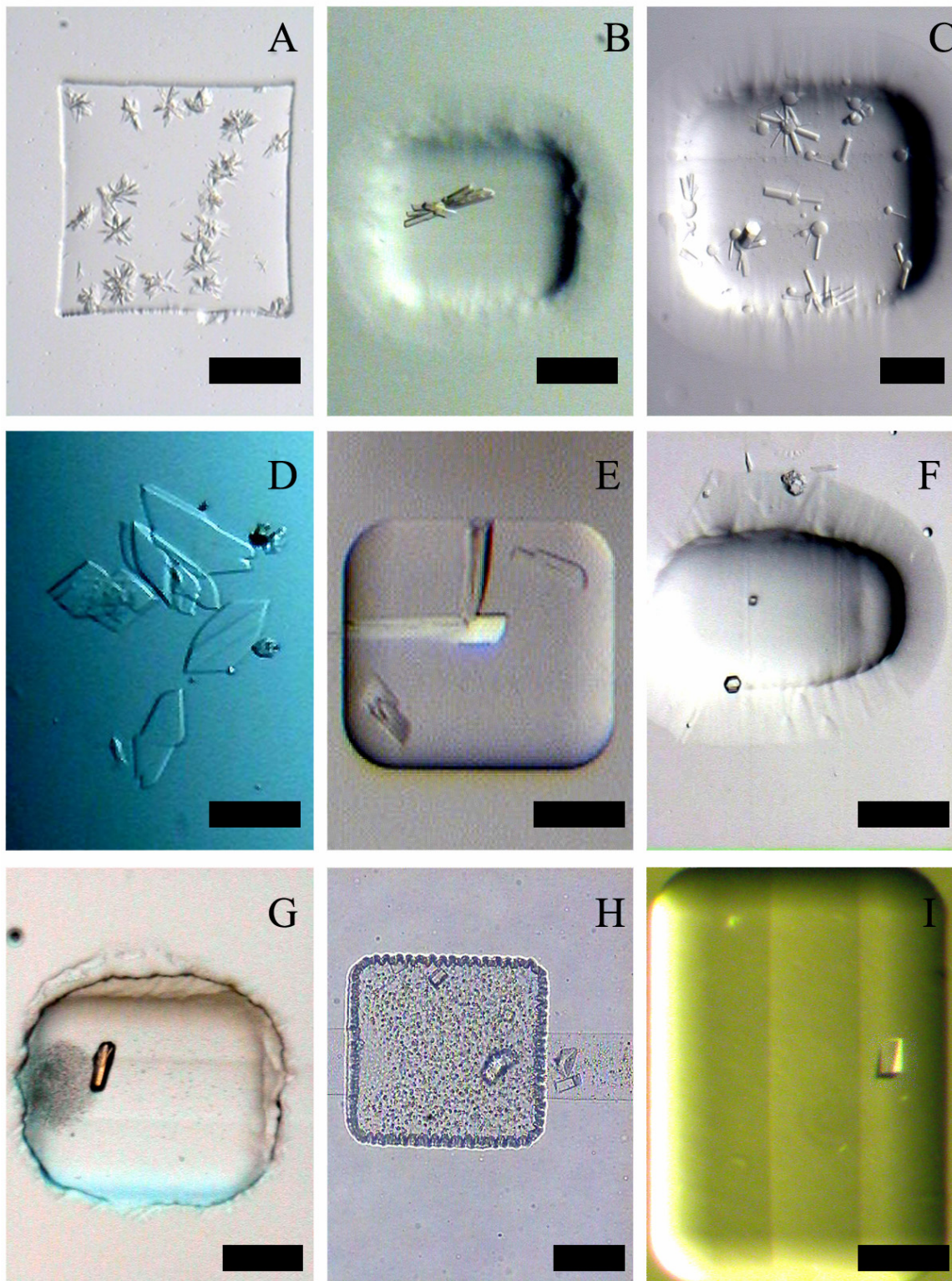
Figure 26: Optical micrographs of macromolecule crystals grown in chip. **(A)** Needle clusters of hdTfR/HFE complex. 13 mg/mL sample mixed at 1:1 ratio with precipitant (17% v/v PEG MME 750, 250 mM sodium chloride, 100 mM TRIS·HCl pH 7.6). **(B)** Rod cluster of P450 Alkane Hydroxylase MUT 139-3. 30 mg/mL sample mixed at 1:1 ratio with precipitant (30% w/v PEG 8000, 0.2 M sodium acetate, 50 mm sodium citrate pH 5.5). **(C)** Rod crystals of DNA helicase B/C complex. 15 mg/mL sample mixed at 1:1 ratio with precipitant (1.26 M $(NH_4)_2SO_4$, sodium cacodylate pH 6.5) **(D)** Crystals of Vault. 3 mg/mL protein sample mixed 1:1 with precipitant (15% PEG 400, 0.2 M sodium citrate, TRIS·HCl pH 8.5) **(E)** Crystals of E. coli aquaporin AqpZ. 20 mg/mL sample mixed at 3:1 ratio with precipitant (28% v/v PEG MME 2000, 200 mM , 4% isopropanol 100 mM magnesium chloride, 100 mM sodium cacodylate pH 6.5) (55) **(F)** Crystal of Probable ribonuclease III (RNASE III) from mycobacterium tuberculosis Rv2925. 7 mg/mL sample mixed at 1:3 ratio with precipitant (20% (w/v) PEG-8000, Ca(OAc)$_2$, MES pH 6.0) **(G)** Crystal of 70s ribosome. Approximately 5 mg/mL sample mixed at 1:1 ratio with precipitant (18% w/v PEG 8000, 0.2 M calcium acetate, 100 mM sodium cacodylate pH 6.5) **(H)** Crystals of mechanosensitive ion channel of large conductance (MscL) from E. coli. 20 mg/mL sample mixed at 1:4 ratio with precipitant (35 % PEG 600, 100 mM ammonium sulfate, 100 mM sodium cacodylate pH 6.5). **(I)** Crystals of DNA condensin complex cndD/G/H. 20 mg/mL sample mixed at 4:1 with precipitant (10 % w/v PEG 8000, 8% v/v ethelyne glycol, 0.1 M HEPES pH 7.5)

Vault is an extremely large (13-MDa) ribonucleoprotein assembly, composed of three proteins (TEP1, 240 kDa; VPARP, 193 kDa; and MVP, 100 kDa) that are highly conserved in eukaryotes and an untranslated RNA (vRNA). This complex is of interest to nanotechnology as a potential vehicle for drug delivery and has also been implicated in the multidrug resistance in cancer cells (56). Although two-dimensional crystals were reported during cryo-electron microscopy studies, severe limitations in sample availability had prevented conventional crystal screening, making it an ideal target for chip-based experimentation. Vault was screened in the μFID format against (3) commercial sparse matrix screens (Crystal Screen; Hampton Research, Wizard I and Wizard II; Emerald Biostructures). Large single plate crystals having largest dimensions of approximately 100 microns were detected in three conditions (Figure 26D). These conditions were successfully exported directly to hanging drop format. Preliminary diffraction data at low resolution has been collected from these crystals (D. Eisenberg, personal communication).

Different crystal forms of a macromolecule can exhibit large variations in robustness, size, shape, and perfection. Since not all crystal forms will be suitable for high-quality diffraction studies, it is often of interest to detect new crystallization conditions. The greater efficiency of μFID crystallization screening allows for novel conditions to be identified which were missed by traditional screening. A previously unidentified crystal form of the bacterial 70S ribosome was obtained (Figure 26G) in three conditions of a

sparse matrix of precipitants (Hampton Crystal Screen I), demonstrating that large protein/nucleic acid complexes may be crystallized in chip (C. Hansen, A. Vila-Sanjurjo, and J. Cate, personal communication).

P450 139-3 is refers to the heme domain of a mutant of P450 BM-3 from *Bacillus megaterium* (P450 BM-3). P450 139-3 is a highly efficient catalyst for the conversion of alkanes to alcohols (57). P450 139-3 had failed to produce crystals from initial screens in vapor diffusion format. Subsequent broad-based screening gave rise to very thin (minimum dimension less than 1 micron) needle crystals. A single round of chip-based screening using standard sparse matrix screens resulted in the identification of novel conditions giving rise to single three-dimensional rod-shaped crystals (Figure 26B). Crystals were scaled up and harvested using larger-volume µFID format (see Chapter 8), and subjected to diffraction studies. Initial diffraction produced reflections out to approximately 10 Å resolution. The low resolution diffraction was likely in part due to poorly optimized cryo-protection and mechanical damage during harvesting; crystals showed visible cracking and melting during harvesting process. Subsequent protein preparations gave rise to markedly different behavior, failing to produce crystals. This study was ultimately abandoned due to difficulties in obtaining protein samples of consistent quality from our collaborators.

Chip-based µFID has further proved applicable to the crystallization of integral membrane proteins. In one study (performed at Fluidigm Corporation in collaboration with B. Stroud) a successful condition for the crystallization of an ion channel (aquaporin AqpZ from *E.*

coli) identified in hanging drop, and transported directly to chip resulted in large single crystals; demonstrating that membrane proteins can be crystallized in nanoliter volume silicone μFID reactors (Figure 26E).

In a second study a previously crystallized mechanosensitive ion channel (MscL) was screened against 5 sparse matrix screens (Hampton Crystal Screen I, Hampton Crystal Screen II, Hampton Peg Ion Screen, Emerald Biostructures Wizard I, Emerald Biostructures Wizard II) at 20 °C and 4 °C. MscL refers here to the mechanosensitive ion channel of large conductance from *E. coli*. MscL is a member of a large family of mechanosensitive channels implicated in the regulation of osmotic pressure in prokaryotes (58). 10 successful conditions were identified in the experiments performed at 4 °C; room temperature screening produced only phase separation. The chip-based crystallization conditions showed excellent agreement with those identified in hanging drop experiments, and included an additional crystallization condition. This novel condition was optimized and transported to larger volume μFID format (see Chapter 8) to grow large crystals that diffracted to low resolution (approximately 9 Å). Attempts to improve resolution by screening cryo-protectants were unsuccessful. The low resolution diffraction is consistent with data collected from crystals optimized from hanging drop formats and suggests low intrinsic crystal order. One possible source of crystal disorder that has been suggested is the incomplete cleavage of HIS tags from the protein subunits, resulting in a heterogeneous protein sample (S. Steinbacher, personal communication).

For target macromolecules that exhibit a very narrow crystallization slot, the growth of high-quality crystals is dependent on achieving optimal mixing kinetics. In some cases, such as the hdTfR/HFE complex, crystallization may require very specific mixing kinetics and conditions which are difficult to acheive in microbatch or vapor diffusion formats. In other cases, the highly efficient mixing kinetics realized in μFID reactions may be used to change the habit and improve the quality of crystals grown using conventional techniques. One such example is the crystallization of a 450 KDa DNA B/C helicase loader complex. DNA B is the bacterial hexameric replicative helicase and DNA C is the accessory protein that mediates DnaB loading at replication initiation sites. In this study hanging drop conditions based on sulfate salts were found that produced very small (maximum dimensions of 5 μm, minimum dimensions < 1 μm) poorly formed needles. No improvement in the size or morphology of these crystals was achieved despite attempts at optimization through extensive grid and additive screening. Independent screening of this complex against standard sparse matrix screens identified similar crystallization conditions based on ammonium and lithium sulfate salts. Chip-based crystals were however of much higher quality, exhibiting three-dimensional hexagonal rod morphology with maximum dimensions of 200 microns, and minimum dimension of 25 microns (Figure 26C). Although harvesting of these chip-grown crystals has been problematic, initial diffraction studies from a single crystal that was grown in hanging drop (and could not be reproduced) showed reflections to 3 Å resolution. Indexing data from chip-grown crystals confirmed that the space group and lattice constants (space group P3; unit cell dimensions a=b=174.5 Å, c=87.98 Å, $\alpha=\beta=90°$ $\gamma=120°$) were the same, suggesting that the crystals are intrinsically well ordered.

Perhaps the most striking result of these studies has been the rapid identification of crystallization conditions for novel targets that had been exhaustively screened without success. In one instance, crystals of a mycobacterial RNase were obtained from a single experimental condition on chip (Figure 26F), whereas no crystals had been observed for this sample despite extensive prior trials using traditional methods. Subsequent broad-based screening efforts around this condition using hanging-drop vapor diffusion setups proved successful, but only after the protein concentration was increased from 7 mg/mL to > 40 mg/ml. Crystals grown by vapor diffusion diffracted to 2 Å resolution and were used to solve the structure of this protein (D. Aiky, personal communication).

In another striking example a 750 KDa ternary complex (DNA D/G/H) (59), that had been in crystallization trials for over two years without success, was screened against 4 sparse matrix screens in chip. DNA D/G/H refers here to a subassembly of the *S. cerevisiae* condensin complex comprised of the CndD, CndG, and CndH subunits. It lacks the two ATP-binding subunits of condensin, Smc2 and Smc4. After 2 days of incubation at 20 °C single three-dimensional crystals with rounded edges (maximum dimension 20 microns) were observed at a mixing ratio of 3:1 (precipitant : protein) in two related chemical conditions based on PEG 3350 and sodium acetate. This condition was reproduced in a subsequent chip-based experiment performed at 4 °C, resulting in three-dimensional polyhedron-shaped crystals (maximum dimension 20 microns) with well-defined edges. A systematic grid screening strategy varying precipitant concentration, salt concentration, and pH was used to successfully transfer this condition to hanging drop. Initial diffraction

studies of these crystals gave very poor diffraction (highest-order reflections at approximately 20 Å). Subsequent protein preparations failed to produce crystals despite repeated trials over a period of approximately 4 months. Crystals were finally recovered in chip-based trials by conducting a partial proteolytic digest of c-terminal residues (Figure 26I). Initial diffraction studies of chip-grown crystals displayed reflections to approximately 5.5 Å resolution. The crystals were in space group P3 with unit cell dimensions a = 223.11 Å, b = 223.11 Å, c = 265.56 Å, $\alpha = \beta = 90.0°$, $\gamma = 120°$ (S. Gradia, personal communication). Attempts to transfer this condition to hanging drop vapor diffusion format by systematic screening based on the chip condition were unsuccessful until a detergent additive was used. The condition that ultimately gave crystals in hanging drop format included a detergent additive, had higher salt concentration, and lower peg concentration when compared with the successful chip condition. These crystals showed diffraction to 5.5 Å. Unfortunately, subsequent protein preparations have again failed to crystallize despite meticulous reproduction of the initial expression, purification, and crystallization protocols. Continued crystallization trials attempting to reproduce this success are currently underway. Additionally, orthologues of this complex derived from a variety of organisms are being investigated as potentially more tractable crystallization targets (J. Berger, personal communication).

C h a p t e r 5

SYSTEMATIC SOLUBILITY STUDIES: FORMULATOR DEVICE

Introduction

Understanding the phase behavior of proteins is an essential part of the crystallization process. The growth of crystals from a protein solution requires the existence of a nontrivial phase diagram which allows the protein state to be manipulated between at least two thermodynamic phases: soluble and precipitated. The processes of crystal nucleation and growth arise on the boundary between these two phases, and are governed by subtle effects in physical chemistry. There are a variety of schemes that manipulate the kinetics of the crystallization process, and all take advantage of generic features of these phase diagrams (44). However, in practice the phase behavior of very few proteins has been studied in detail (60-68), and solubility information for a specific protein is rarely available for crystallization and optimization experiments (69, 70).

Furthermore, it is often an arduous process to find the right combination of chemicals that yields appropriate phase behavior for a given protein. Every protein is different, and even a modest subset of stock precipitating solutions comprise a vast chemical phase-space that must be explored. The large amounts of sample required make systematic exploration by conventional techniques infeasible, and screening is typically directed towards random sampling using an incomplete factorial or sparse-matrix approach, which is a brute-force process requiring large numbers of experiments (15, 34). There have been numerous attempts to rationalize this procedure, for example by using computational approaches to

predict phase behavior (71, 72) or by trying to correlate measurements of osmotic 2nd virial coefficients (73, 74) with crystallization conditions. Practical limitations have thus far prevented these techniques from being generally applicable.

Although the small-scale characterization of protein solubility by a pre-crystallization solubility assay has been reported (15, 75, 76), this technique has not been widely adopted since the large required sample volumes make it unsuitable for targets that cannot be expressed and purified in large quantities. Microfluidic technologies enable ultra-small volume processing and hence are ideally suited to address these problems. Previously microfabricated dispensers have been used to reduce sample consumption in cases where the sequential addition of reagents to a levitated drop of microliter volume is sufficient to explore a restricted chemical space (76). This Chapter describes the development of a microfluidic device that allows for the practical and systematic exploration of protein phase-space behavior.

Combinatorial Mixing on Chip

Thorough characterization of protein solubility behavior requires accessing a vast chemical space through the combinatorial mixing of a limited number of stock reagents. The layout of a microfluidic formulator device that combines precise and robust PCI metering with microfluidic mixing (14) and multiplexing elements (27) is shown in Figure 27. This design allows for unprecedented fluid handling capability and represents the first implementation of true combinatorial mixing on chip.
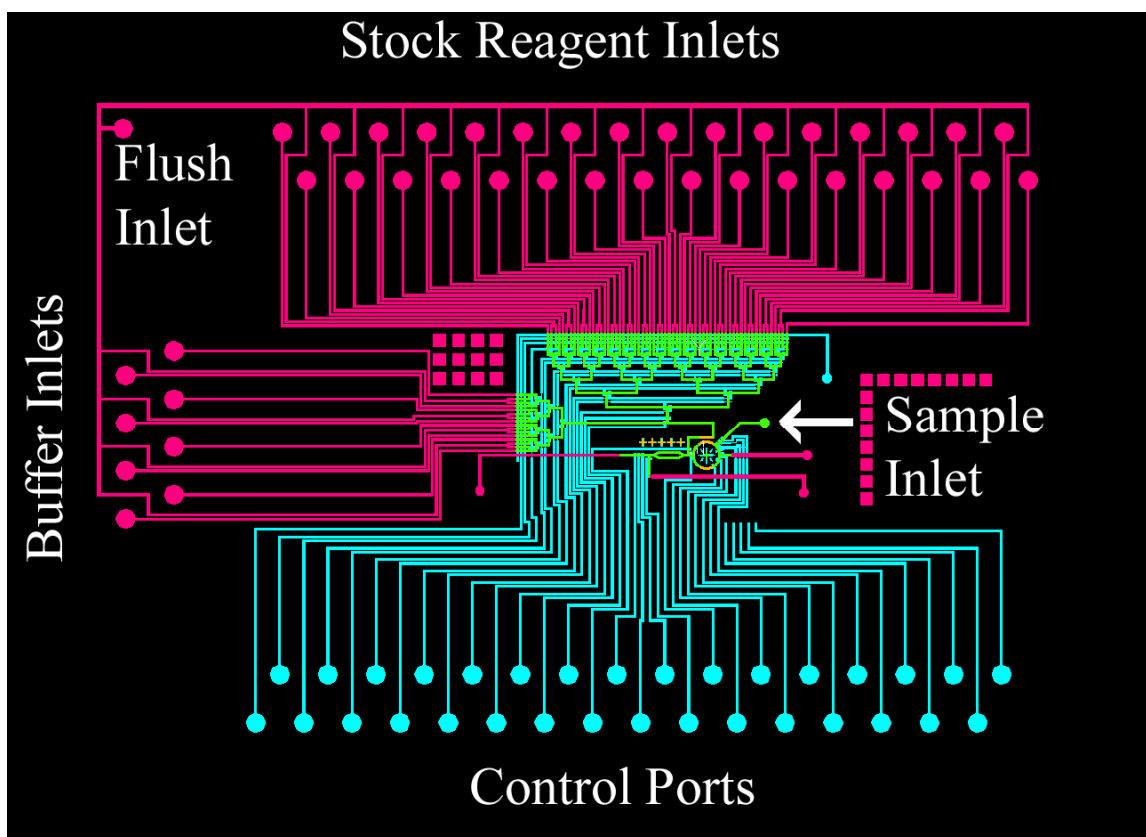
Figure 27: Microfluidic formulator device. Device allows programmable combinatorial mixing of 32 stock solutions (top), 8 buffer solutions (left) and a sample solution (center). 27 pneumatic and hydraulic control lines are interfaced to external solenoid actuators through an array of control ports (bottom). The control layer mold is patterned from a single mask shown in blue. A multilevel flow layer is patterned from three separate lithography steps; 50 μm SU8 2075 for low impedance inlets and outlets (pink), 13 μm 5740 for rounded channel structures compatible with integrated valves (green), and 10 μm SU8 2015 for observation windows of rectangular cross section (yellow).

The active region of an earlier version of the microfluidic formulation chip that allows for the arbitrary combinatorial mixing of 16 stock reagents into one of 16 buffer solutions is

shown in Figure 28A. Two 16-solution multiplexer arrays, actuated by 8 control lines, allow for the selection of buffers (left) and reagents (bottom). A PCI junction, formed by a 3-valve peristaltic injection pump (red) and cross-injection valves (center green) dispenses directly into a 5 nL ring reactor. Once the reactor has been flushed, a reagent line is selected and the cross-injection sequence is executed. The extended split channel region increases the volume of the cross-injection junction, thereby allowing for up to 15 injections. The maximum number of consecutive injections that may be executed before the junction needs to be recharged depends on the Taylor dispersion (77) of the injected fluid as it is pumped down the channel, and is therefore a function of the analyte diffusivity and the flow rate. Figure 28B shows the injection of 4 slugs, each having a volume of 80 pL, into the ring reactor. Arbitrary combinations of 16 reagents may be produced in the reactor by sequential flushing and injection steps. Figure 28C shows a color gradient formed from the sequential injections of water, blue dye, green dye, yellow dye, and red dye. In screening applications that require the interrogation of a precious sample against many pre-mixed reagent formulations, the cross-injection flushing step is wasteful and is circumvented by the injection of sample through a separate sample injection site (Figure 28D). After the ring is filled with the desired reagents, they are mixed by active pumping around the ring (14).
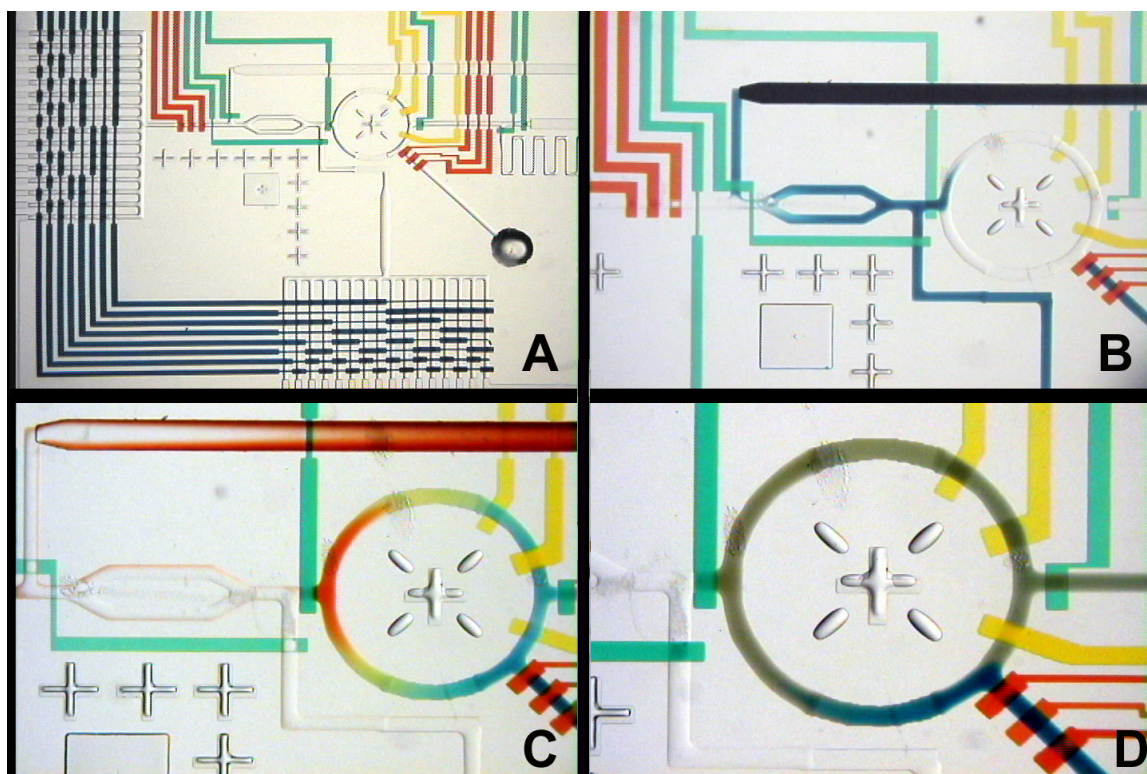
Figure 28: Combinatorial mixing using a microfluidic formulator. **(A)** Integration of multiplexer (dark blue), peristaltic pumps (red), rotary mixer (yellow), and PCI junction (center green) components for on-chip combinatorial formulation. The parallel multiplexer shown has been replaced with a binary tree multiplexer in more recent designs. **(B)** Injection of approximately 250 pL (4 injection cycles) of blue dye into rotary mixer. **(C)** Color gradient formed by consecutive injections into mixing ring (8 injections blue, 8 injections green, 8 injections yellow, 8 injections red). **(D)** Pumping around ring for 3 seconds results in complete mixing of dye. Blue dye is added to mixture through sample injection inlet (bottom right).

Robust and Precise Picoliter Metering

The reagents used in crystallization exhibit a large variation in physical properties such as viscosity, surface tension, ionic strength, and pH. This variation presents a formidable challenge for fluid handling systems that must allow for arbitrary fluid combinations and proportioning. The positive displacement cross-injection metering method overcomes this obstacle, allowing for variable dispensing to be dynamically programmed by the user in 80 picoliter increments with less than 5% variation over a broad range of fluid properties.

The precision of metering was evaluated by injecting variable amounts of dye (bromophenol blue sodium salt; Sigma) into a reactor, mixing, and performing absorption measurements. Measurements were taken to determine the concentration of bromophenol blue sodium salt (absorption peak at 590 nm). A 9 μm high segment of the mixing ring (approximately 300 μm by 80 μm) having rectangular cross section was illuminated with a 590-nm diode (AND180HYP; Newark Electronics) and imaged through a stereoscope (SMZ 1500; Nikon) onto a charge coupled device camera. Pixel intensities were averaged and compared to an identical adjacent reference channel containing the undiluted dye (2 mM bromophenol blue sodium salt, 100 mM TRIS-HCl pH 8.0). In some experiments glycerol was added to the injected dye to vary the viscosity. Dye concentrations were calculated using the Beer-Lambart relation as

$$\frac{C_{data}}{C_{max}} = \frac{\ln\left(\dfrac{I_0 - I_{back}}{I_{data} - I_{back}}\right)}{\ln\left(\dfrac{I_0 - I_{back}}{I_{ref} - I_{back}}\right)} \quad , \qquad \textbf{(8)}$$

where I_0 is the intensity measured prior to injections, I_{back} is the background ccd intensity, I_{ref} is the intensity measured in the reference channel, and I_{data} is the intensity measured in the ring. The injected volume was then calculated from the measured concentration assuming a nominal ring volume of 5 nL determined by the measured height and geometry of the master mold.

A set of 900 sequential titration experiments (Figure 29A) shows the metering to be both precise and reproducible, with a slope of 83.4 pL per injection cycle and a coefficient of correlation of 0.996. The standard deviation of the injected slug volume was determined to be approximately 0.6 pL. Although the positive displacement metering ensures that the injected volume is robust to changes in the fluid viscosity, the viscosity of the working fluid does however reduce the bandwidth of the injector. It was found that for a solution having viscosity of 400 cP the frequency response of the injector began to roll off at 10 Hz. When operating at an injection frequency of 5 Hz all solutions having viscosities below 400 cP produced even injection volumes. Since the metering mechanism is completely mechanical, there is no dependence on the pH or ionic strength of the injected fluid. Additionally, since the fluid is not dispensed from the chip, there is no phase interface, and therefore little dependence on surface tension, so that the metering technique is truly robust to the physical properties of the injected fluid. Titration experiments with fluids of varying glycerol concentration show the injection volume to vary by less than 5% over a viscosity range of 1 cP to 400 cP without any modification to the injection sequence (Figure 29B).
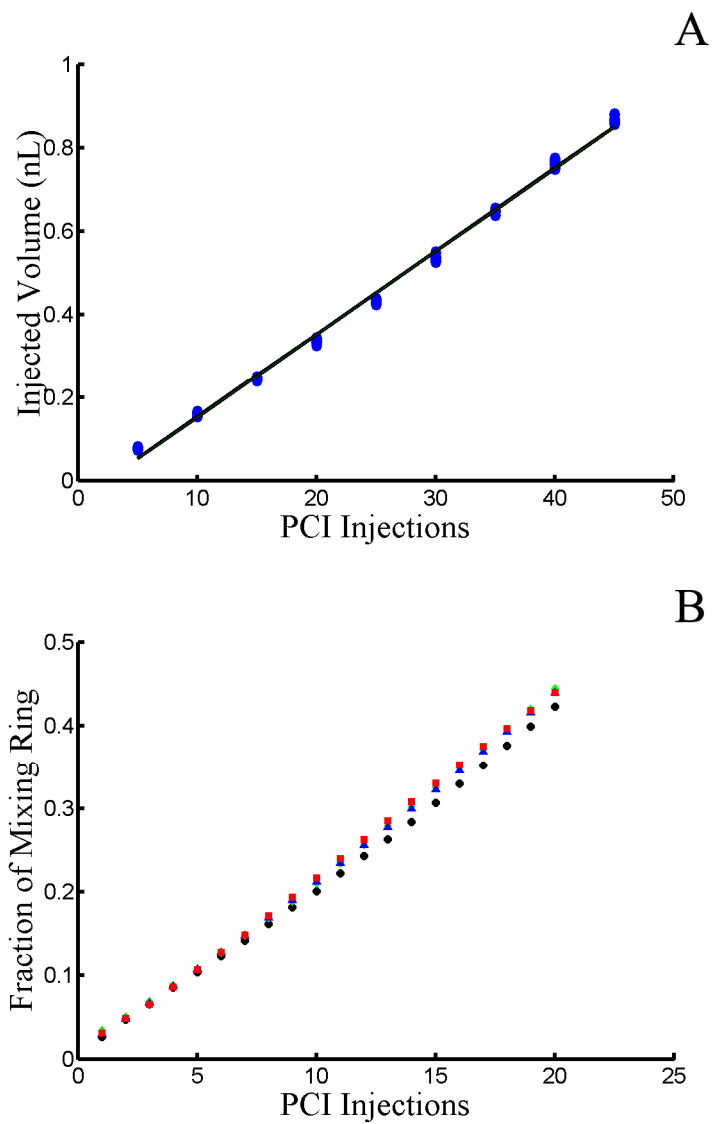
Figure 29: Precise and robust microfluidic metering. **(A)** Absorption measurements showing high precision and reproducibility of PCI injections. Each of the 9 clusters represents 100 identical injection sequences. **(B)** Absorption measurements of 4 sets of 20 injection and mixing sequences showing metering to be robust to the viscosity of the injected fluid. Fluids contain varying amounts of glycerol and have viscosity ranging from 1 cP to 400 cP (black = cP, blue = 40, red = 100 cP, green = 400 cP).

Cross-Contamination Issues

The cross-contamination of reagents is a concern in formulation experiments that are sensitive to residual amounts of various chemicals that are present in the stock solutions. Within the formulator device cross-contamination may occur by three mechanisms: carry-over within the PCI junction, adsorption to the elastomer walls, and unwanted mixing within the multiplexer structure.

Carry-over within the PCI junction may be minimized by proper fluidic design and sufficient flushing protocols. To ensure the complete exchange of reagents within the PCI junction during a flushing cycle it is necessary to minimize the dead volume of the junction. This is accomplished by ensuring that the inlet of the junction is, within fabrication tolerances, directly adjacent to the mixing ring inlet. A comparison between a poorly designed injector and a low dead volume injector is shown in Figure 30. In the poorly designed injector (Figure 30A) a significant volume of fluid is caught in a stagnation region adjacent to the ring inlet and therefore is not efficiently exchanged by convection. In this case the complete exchange of fluids within the injector is limited by the characteristic time for diffusion of species out of the stagnation region. In the low dead volume injector (Figure 30B) there is no appreciable stagnation region near the inlet so that convection can rapidly exchange the fluids. In this case the flushing speed is only limited by the diffusion of species across the gradient of the flow profile (width of the channel) and is therefore much faster. It should be noted that incomplete flushing at the stagnation area near the outlet of the injector does not contribute to contamination. Absorption

measurements were used to quantify the injector carry-over during a flush cycle of 1.5 seconds. Using a low viscosity solution and standard operating pressure the carry-over (residual concentration of dye) was determined to be less than 5 parts in 10,000 (the limit of detection).
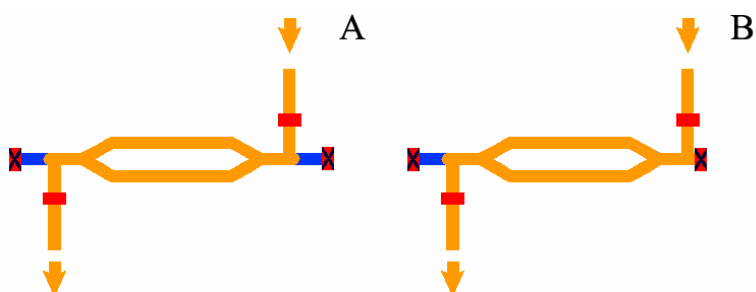
Figure 30: Comparison of injector designs. **(A)** Poorly designed injector having substantial dead volume. **(B)** Low dead volume injector.

Possible contamination due to nonspecific adsorption of molecules to the walls of the container has not been thoroughly investigated. The highly hydrophobic surface of the PDMS makes the adsorption of soluble small molecules unlikely. However, due to their amphiphilic properties, the adsorption protein molecules to the elastomer surface is a concern. For applications in which modest protein concentrations are employed this effect can be significant due to the large surface to volume ratio that is characteristic of microfluidic structures. In the case of protein crystallization, this effect can safely be ignored due to the very high protein concentrations. Considering a section of low aspect ratio channel of width 100 µm and height 10 µm, the surface area per unit length is 220

μm^2. The adsorption of a densely packed monolayer of protein having a characteristic dimension of 5 nm to this surface would require 8.8×10^6 molecules per unit length. Assuming a molecular mass of 40,000 Da, the total mass of protein adsorbed from a 1 km section of channel (1 mL) is approximately 0.5 mg. Since protein concentrations used in crystallization are typically 10 mg/mL or more this represents only 5% of the total protein in solution.

The parallel multiplexing structure (27) reported by Thorsen *et al.* consists of an array of parallel channels which are connected to a single cross-channel and addressed via an array of valves. The large dead volume at the downstream end of each channel within this parallel multiplexing structure makes a certain degree of reagent cross-contamination unavoidable (Figure 31). Although this contamination can be reduced to acceptable levels at the PCI junction by sufficient flushing it causes serious problems in the vicinity of the multiplexer due to unwanted reactions between reagents. In the case of protein crystallization the stock solutions include various salts, polymers, buffers, and organic solvents. The inadvertent mixing of certain combinations of these reagents can lead to phase separation, aggregation, or the formation of insoluble salts. For instance, the mixture of phosphate salts with salts containing magnesium or calcium anions results in the instantaneous formation of insoluble magnesium/calcium phosphate salts. Once insoluble salts are formed they quickly clog the microchannels and ultimately lead to device failure. This reagent incompatibility imposes very stringent demands on the fluidic design and flushing protocols.
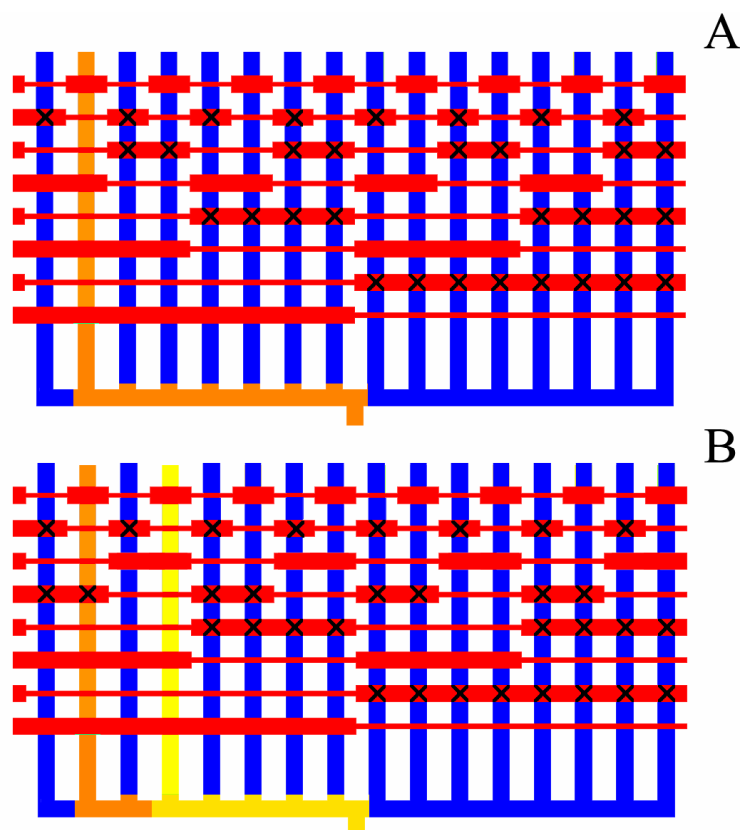
Figure 31: Contamination in parallel multiplexing structure. **(A)** Selection of reagent causes contamination in dead volumes at the inlets of remaining channels and at multiplexer outlet. **(B)** Sequential selection of reagents causes unwanted mixing within multiplexer.

Initial attempts to eliminate this problem used an additional flush channel through which the front of the multiplexer could be flushed after every injection step. A protocol of successive flushing and peristaltic pumping was used to prevent the unwanted mixing of reagents within the multiplexer. Initially the multiplexer is filled with dionized water through the flush channel. A reagent is selected and used to charge the PCI junction. Once the reagent flush step is complete the multiplexer valves are closed and the front of the

multiplexer is flushed through the flush channel. The valves of the multiplexer are then actuated in a peristaltic sequence to expel any contaminated reagent from the multiplexer. The front of the multiplexer is then flushed again and the multiplexer valves are pumped in the reverse peristaltic sequence to refill the multiplexer with dionized water. In this way a "buffer" of water is used to maintain separation between the reagents and prevent unwanted mixing. This protocol was successful in eliminating the formation of insoluble salts over a two week period of operation; in the absence of this protocol insoluble salt formation was observed within a minute of device operation.

Although the protocol of successive flushing and pumping steps is effective at eliminating unwanted reagent mixing it adds considerable control complexity and has two undesirable drawbacks. Firstly, the additional flushing and pumping steps are very time consuming and account for nearly half of the experiment time. Secondly, it was found that in order to avoid unwanted mixing it was necessary to have more reverse pumping steps than forward pumping steps, leading to the growth of the dionized water "buffer" region over time. Charging of the PCI junction with a selected reagent requires that this buffer region be completely expelled and therefore requires that the flush time be increased. Since the size of the "buffer" is determined by the history of the flushing sequence it is difficult to ascertain the appropriate length of each flush cycle. Additionally, if a reagent is not used for extended periods of time the "buffer" becomes impractically large extending off the chip and into the connecting tubing.

In order to eliminate reagent cross-contamination and avoid cumbersome flushing protocols a low dead volume multiplexing structure was designed. A binary tree flow channel structure that allows for low dead volume multiplexing of reagents is shown in Figure 32 (personal communication S. Maerkl). N consecutive bifurcations originating at a single channel allow for the 2^N inlet channels to be connected through equivalent fluidic paths. Each level of the binary tree has pairs of valves at the bifurcations which allow for flow to be directed either to the left or right. At the final level of the binary tree every second channel is a flush channel connected in parallel to a common flush inlet containing dionized water (Figure 27). Operation of the device is as follows. The reagent with which the PCI junction will be charged is selected and flushed through a path of the binary tree. Once the injection sequence is complete the least significant valves on the binary tree are reversed, causing water to be flushed through the tree by the same path that the previous reagent followed. The binary tree is thereby restored to its original state and is ready for the next injection sequence. Provided that the flushing step is complete this protocol completely eliminates the possibility of unwanted mixing within the multiplexer.
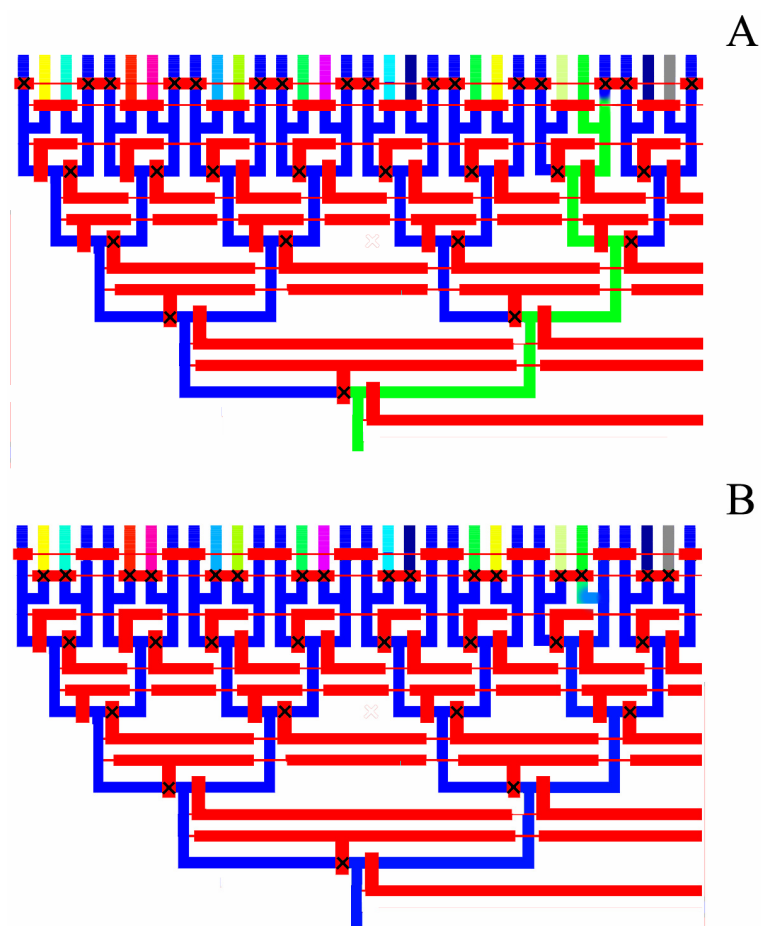
Figure 32: Binary tree multiplexing structure. Low dead-volume junctions and interleaved flush lines (blue) allow for zero reagent cross-contamination. **(A)** Selected reagent (green) is flushed through unique path of binary tree. **(B)** Reversing logic of least significant valves (top) restores the multiplexer to its original state.

I/O Interfacing

The utility of a technology depends ultimately on the ease with which it can be used. Invariably, time spent optimizing the robustness of a device, and engineering practical interfaces, results in increased productivity. The large number of solution and control

inlets used in the formulator device presents a significant challenge for chip i/o interfacing. Individually connecting the 78 required fluidic connections that must be made is very time consuming and introduces the risk of incorrect connections being made. Additionally, since the formulator uses extensive flushing protocols, and can operate for weeks at a time it is necessary that there be a sufficient reservoir of flushing, buffer, and stock reagents.

In the case of the screening device the problem of introducing 49 separate solutions into the chip was solved by introducing each reagent into a separate inlet well using a pipette and then applying pressure to all reagents simultaneously via a seal with the top of the device. In the case of the formulator device, the footprint of the wells required to supply a sufficient volume of stock solutions (approximately 100 μL) is impractical. To address this issue a manifold was designed that allows for 1 mL reservoirs of reagents to be interfaced to the device. The base of the manifold consists of a Delrin® block into which an array circular holes has been machined to accommodate 1 mL Nalgene® centrifuge tubes (Figure 33A). The holes are designed such that, when inserted, the tops of the tubes are just below the surface of the block. The block has a cover plate with an array of tapped 10-32 through holes that are aligned with the tubes (Figure 33B). Fittings with 20 gauge stainless steal pins are screwed into each hole of the plate (Figure 33C). O-ring seals at each fitting make an air-tight seal with the plate. An O-ring seal between the plate and the block creates a closed chamber that may be pressurized through a single inlet located on the side of the block. When assembled (Figure 33D) the end of each pin is immersed a separate reagent tube so that pressurizing the chamber causes the reagent to flow through the tube. A thin layer of paraffin oil is added to the top of each tube to ensure minimal evaporation during

the course of an experiment. The large volume of reagent in each tube (1 mL) is sufficient for continuous operation of the formulator over several weeks.
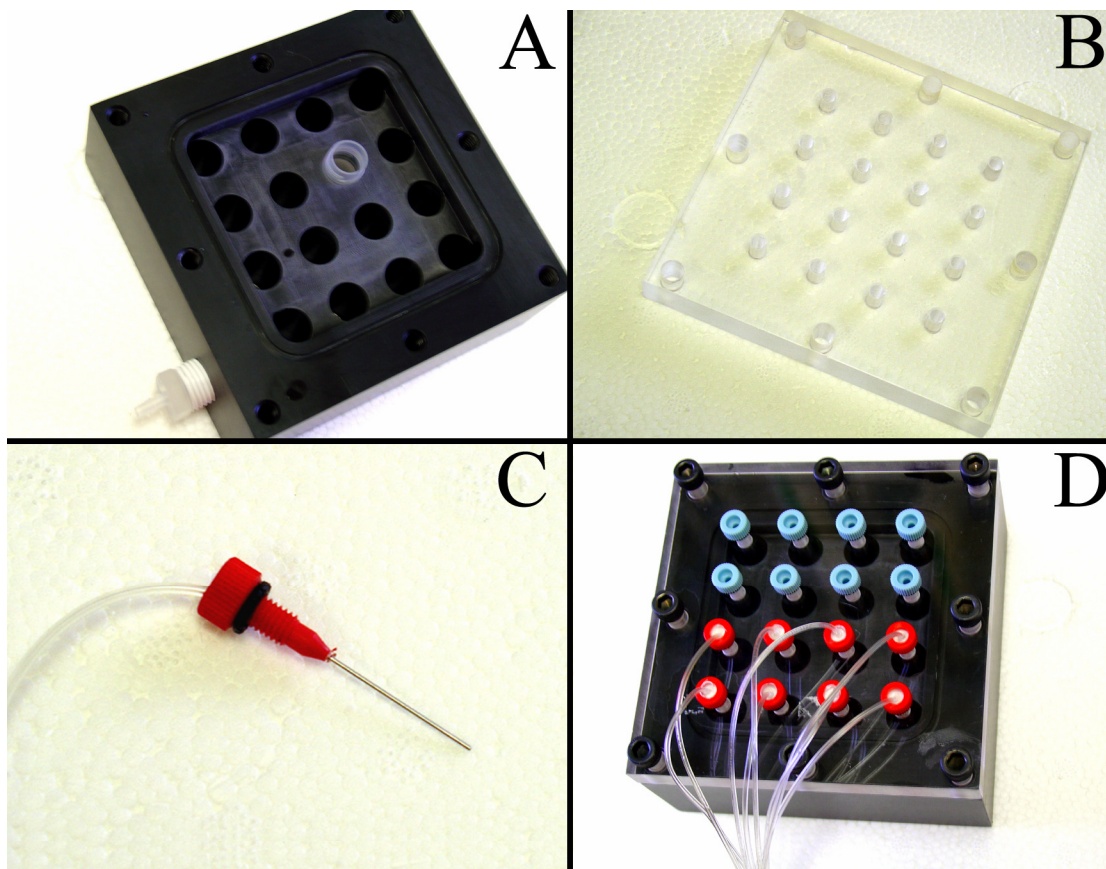
Figure 33: Reagent manifold for formulator device. **(A)** Delrin block with pressurization port (bottom left). One reagent tube in inserted in hole array. **(B)** Top plate of manifold. **(C)** Fitting with o-ring and pin. **(D)** Assembled manifold shown with 8 of 16 wells connected to tubing. Remaining ports are occupied by plugs.

In order to quickly and correctly establish the large number of connections required for the formulator operation, a standard one-touch connector was designed. The connector consists of an aluminum piece with two rows of 16 through-holes bored at a 0.1″ pitch.

The rows are separated by a distance of 0.1″ and offset by 0.05″. Each hole accommodates a 1″ long 20 gauge stainless steal pin that extends ¼ ″ from the surface of the connector that mates with the chip (bottom). The pins on the top of the connector are bent 90° and interface with microbore Taigon® tubing that is connected to the reagent manifold. This 32 pin connector is easily inserted and removed from the device to make quick connections. The connection of a formulator device to 32 reagent lines and 32 control inputs via two one-touch connectors is shown in Figure 34.
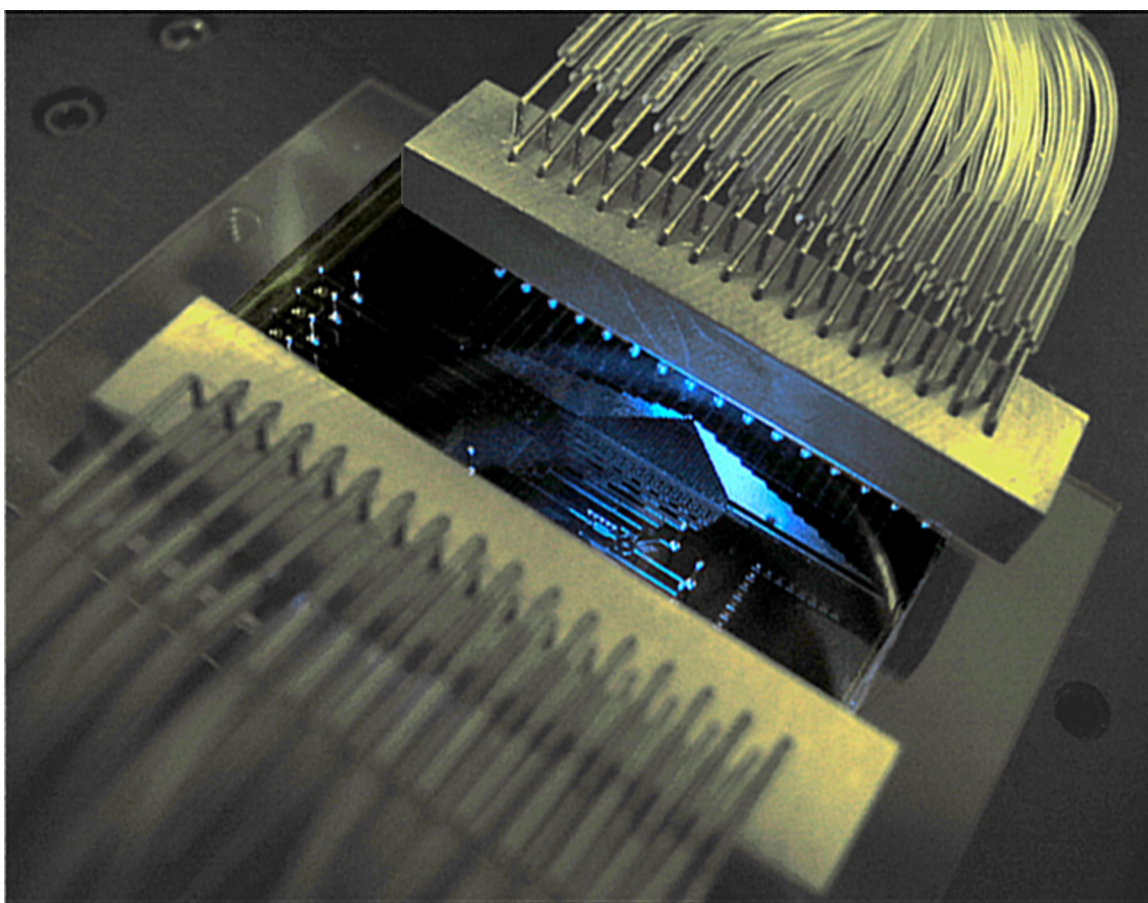
Figure 34: Microfluidic formulator device with one-touch 32 pin fluidic connectors. Stock reagents are introduced from manifold through a 32 pin one-touch connector (top).

Pneumatic and hydraulic control lines are interfaced through a separate 32 pin connector that interfaces with solenoid manifolds.

C h a p t e r   6

MICROFLUIDIC MIXING: SCALING LAWS AND OPTIMIZATION

Introduction

Rapid microfluidic mixing is necessary for conducting the large number of experiments required for systematic phase-space mapping in a pratical time. This Chapter discusses how the basic physics of microfluidic fluid flow and mass transport affect the design and optimization of the rotary mixer used in the formulator device.

Achieving efficient mixing in the microfluidic environment is problematic due to the characteristic laminar flow that is manifested in these devices. At the small length scales that are characteristic of microfluidic devices viscosity becomes dominant over inertial effects in mass transport phenomena. Put simply, this implies that the fluid has no memory and that the flow field is instantaneously determined by the imposed boundary conditions. In particular the advection of momentum, which leads to turbulent mixing in macroscopic systems, is suppressed so that the flow is laminar. The relative importance of viscous and inertial forces, and hence the onset of turbulence, is determined by the Reynolds number:

$$\text{Re} = \frac{\rho U L}{\mu} \quad , \tag{9}$$

where ρ is the fluid density (g/cm^3), U is the characteristic velocity (cm/s), L is the characteristic channel dimension (cm) and μ is the viscosity of the fluid (g/cm·s). For most flows in small channels the Reynolds number is small so that the flow is laminar and the

familiar turbulent mixing of macroscopic devices vanishes. The transition from laminar to turbulent flow occurs at Reynolds numbers of approximately 2000. By comparison, the flow of water at 1 cm/s down a 10 μm high channel has a Reynolds number of 10^{-1}, and is therefore completely laminar.

All mixing is ultimately accomplished by diffusion. Accelerated mixing may therefore be accomplished by generating convective flows to increase interface areas, decrease characteristic diffusion lengths, and enhance concentration gradients. In the case of macroscopic fluidic devices (like a coffee cup) this may be readily achieved through turbulent mixing. Turbulent mixing gives rise to exponential reduction in characteristic separations, thereby causing rapid and efficient mixing. For example, pulling a spoon through a coffee cup causes complete mixing within seconds.

Turbulent mixing cannot be accessed in microfluidic devices that operate in the regime of low Reynolds number. It is nevertheless possible to achieve exponential mixing by the process of chaotic advection. The implementation of chaotic advection for efficient microfluidic mixing has been reported using three-dimensional flows created by spiral mixers (78), herringbone mixers (79), and reverse-micelle mixers (80). All of these strategies achieve chaotic advection by means of a three-dimensional flow field.

Generally, steady two-dimensional flows are integrable and cannot access exponential mixing by means of chaotic advection. However, geometric mixing can be accomplished by the repeated "folding" or "kneading" of a fluid onto itself. A rotary mixer based on this

principal was proposed by Chou *et al.* (14). In this mixer two or more fluids occupying different sections of a ring-shaped channel structure are homogenized by active pumping around the ring. Unlike the herringbone and spiral flow-through mixers which accelerate mixing between laminate streams of fluids flowing in juxtaposition along a channel, the rotary mixer is a batch mixer that homogenizes fluids that are serially introduced into the ring. Fluids pumped around the ring are subject to a transverse gradient in the flow velocity due to the non-slip boundary conditions at the channel walls, resulting in the axial dispersion of analytes. Mixing in this structure is accelerated through the combination of this axial dispersion and the periodic boundary conditions imposed by the ring structure.

During mixing, molecules are subject to the combined effects of convection and diffusion. As molecules diffuse transversely across the channel they sample different flow rates. The net dispersion, and hence the time required to homogenize different reagents, therefore depends on the relative contributions of convection and diffusion. A comparison of the importance of these two effects is given by the non-dimensional Peclet number:

$$Pe = \frac{UL}{D},$$
(10)

where U is the fluid flow velocity, L is the characteristic spatial dimension (say the width of the channel), and D is the diffusion constant of the analyte.

The dispersion of an analyte due to pressure-driven flow down a channel of circular cross section was first described by G.I. Taylor in 1953 (77). A thin slug of tracer particles

flowing down a channel is stretched by the non-uniform velocity profile. The non-slip boundary condition imposed at the channel wall implies that a line of tracer particles is stretched to a thickness $U_{max}t$ in time t. Therefore, in the absence of diffusion, the dispersion of the plug is generally linear in time.

Diffusion of the molecules within the flow stream acts to significantly reduce dispersion. As the plug is stretched by the flow a transverse concentration gradient is established, thereby causing molecules to diffuse across streamlines from regions of high velocity to regions of low velocity and vice versa. The characteristic time for a molecule to diffuse the width of the channel is $\tau = h^2/D$. At the end of this time interval the molecule will be located somewhere within the slug that has stretched to a length of $U_{max}\tau$. Therefore, at time t the net progress of the molecule down the channel can be approximated as a random walk of t/τ steps having an average step size of $U_{max}h^2/D$. The dispersion of the molecules is therefore diffusive in nature with an effective diffusivity proportional to $U_{max}^2h^2/D$. At long times a collection of molecules initially defined within a thin slug will evolve into a Gaussian distribution centered at $U_{avg}t$ having mean squared displacement proportional to $U_{max}^2 h^2/(Dt)$. Figure 35 shows a finite difference time domain simulation of the dispersion of a line of tracer molecules in a two-dimensional parabolic flow profile. Concentration profiles are shown after 10 seconds of dispersion for a maximum flow velocity of 100 μm/s, and an analyte diffusivity of 100 μm^2/s. The Peclet number is varied by changing the channel width in each simulation to illustrate the qualitatively different behavior. The Taylor dispersion description is only valid at long times when the molecules have sampled

the entire flow profile and large transverse gradients are relaxed. In the simulation this condition is achieved in the case of Pe = 10.
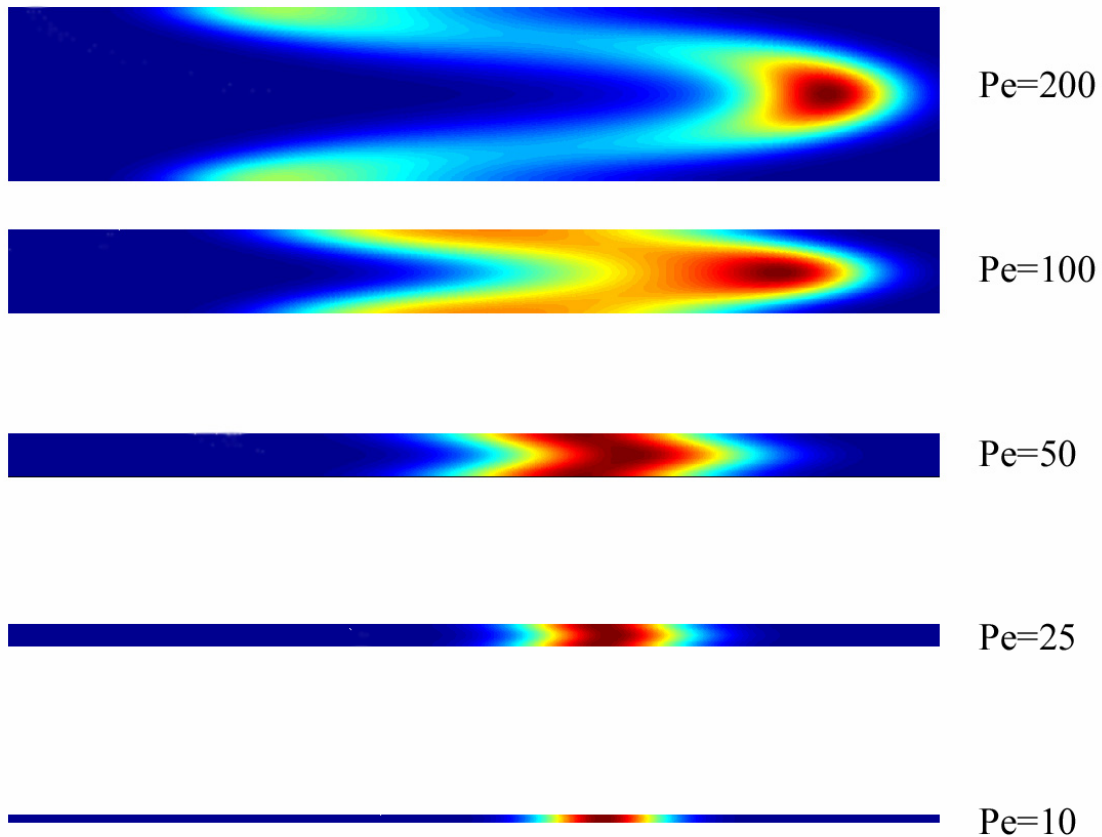
Figure 35: Finite difference time domain simulation of dispersion of tracer particles in parabolic flow profile at varying Peclet number. Diffusion constant is 100 μm^2/s and maximum velocity is 100 μm/s so that Peclet number is equal to the channel width in microns.

Dispersion in Low Aspect Ratio Channels

The distribution of analyte along the stretched plug is determined by the gradient of the flow profile and hence depends on the exact geometry of the channel. The viscous flow of an incompressible Newtonian fluid through a static structure satisfies the Navier-Stokes equation subject to non-slip boundary conditions. For steady-state flow within a channel of constant cross section, and in the absence of body forces, this reduces to the one-dimensional Poisson equation subject to Dirichlet boundary conditions,

$$\frac{\nabla P}{\mu} = \nabla^2 U_z = Const$$
$$\partial U_z / \partial z = 0$$
$$U_z \big|_{\partial \Omega} = 0$$

(11)

The form of solutions to this equation is completely determined by channel geometry and is proportional to the ratio of the pressure gradient to the viscosity, which by similarity arguments must be constant along the channel. In the previous discussion the Peclet number determining the Taylor diffusivity was based on the width of the channel. As discussed below, this is appropriate for channels of semi-ellipsoidal (rounded) cross section but not for channels of rectangular cross section.

Flow through low aspect ratio channels of rectangular cross section is described by Hele-Shaw flow. In general, viscous drag effects in low aspect ratio structures with constant height are dominated by the constricted dimension (height), so that lateral features (obstacles) only have significant effect on length scales comparable to the height. In

situations where Re << h/w << 1, flow lines reproduce those of two-dimensional potential flow (flow at infinite Reynolds number) with a thin boundary layer.

In the case of low Reynolds number flow through a shallow rectangular channel viscous drag is dominated by the height dimension so that only within a distance comparable to the height of the channel is there a significant effect of the wall. This results in a velocity profile that is essentially constant across the width of the channel (Figure 36A). In the vertical direction the flow profile is parabolic, resulting in large velocity gradients. Since the channel height is much smaller than the channel width, gradients due to the wall no-slip condition do not significantly contribute to Taylor dispersion. The relevant Peclet number for determining the Taylor dispersion in a shallow channel of rectangular cross section is therefore based on the channel height. The nearly constant velocity profile across the largest dimension of the channel results in a dramatic reduction in Taylor dispersion when compared to flow through a channel of equal circular cross section. The effective "Taylor diffusivity" in a rectangular 1:10 aspect ratio channel is $U^2A/(2100D)$ compared to $U^2A/(48\pi D)$ for a circular channel of equal cross sectional area A.
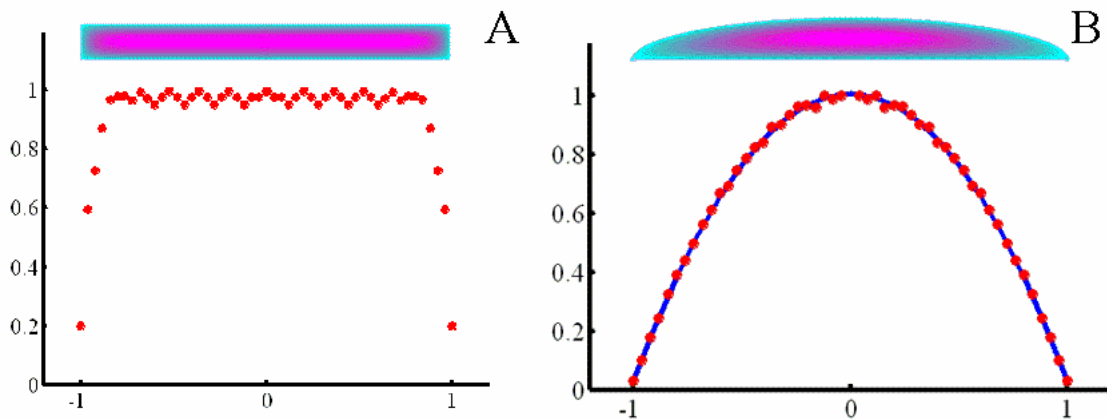
Figure 36: False color plots of normalized flow velocity profiles down a 10 μm high, 100 μm wide rectangular channel (top A) and a 13 μm high, 100 μm wide semi-ellipsoidal channel (top B). Average velocity profiles across channels obtained by integrating out height dependence (bottom A and B). Curve fit to average flow profile in B is $y = 1 - x^2$.

Annealing flow molds to generate a rounded channel cross section has a dramatic effect on the flow profile and the magnitude of Taylor dispersion. A common standard MSL flow-channel geometry is a width of 100 μm and a 13 μm high semi-ellipsoidal cross section. The tapering of the height of channel away from the centerline results in a greatly enhanced fluid drag at the edges. This drag generates large transverse velocity gradients and hence enhances dispersion. Figure 36B shows a finite difference simulation of the flow profile through a 1:10 aspect ratio channel with semi-ellipsoidal cross section. Integrating out the height dependence yields a flow profile that is nearly perfectly parabolic. This profile is observed in experiments (Figure 37). The flow profile in the vertical direction is also essentially parabolic due to the small curvature of the channel. However, since the characteristic diffusion time across the width of the channel is much greater than that across the height (by a factor of 100 for 1:10 aspect ratio), the dispersion arising from the velocity gradient across the width dominates. The appropriate Peclet number for channels of semi-ellipsoidal cross section is therefore based on the width.
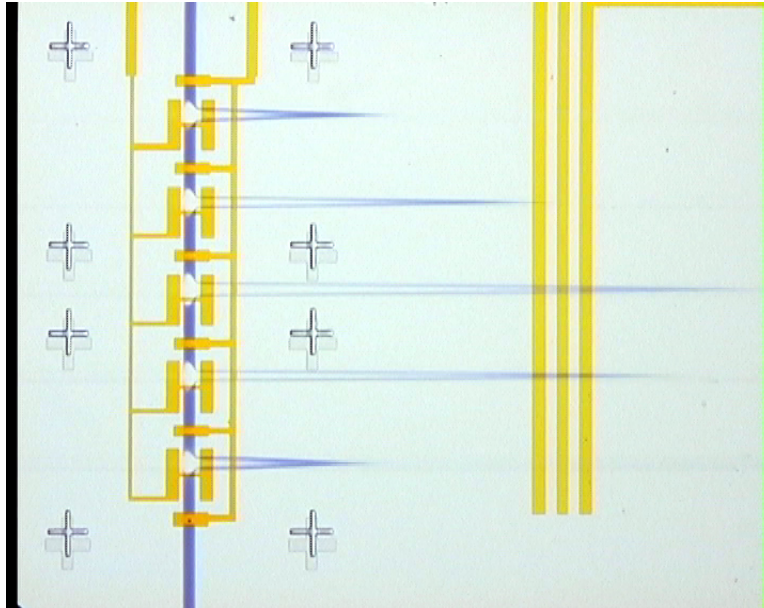
Figure 37: Parabolic flow profile observed across width of semi-ellipsoidal channels.

It is interesting that the thermal reflow of flow channels necessary for complete valve sealing results in the nearly perfect parabolic flow profile that is the two-dimensional analogue of Poiseuille flow through circular capillaries (the geometry treated in Taylor's original paper). The dispersion in the channel case is however greater than that of the capillary case. In the capillary geometry the velocity is a function of the radius so that the occupancy of molecules is biased towards low velocities. The parabolic flow profile combined with opposing linear occupancy results in a constant average concentration along the dispersing slug in the limit of very high Peclet number. In the semi-ellipsoidal channel geometry the occupancy is biased towards high velocities due to the varying channel height, creating a more dispersive flow.

Rotary Mixing: Scaling Laws and Simulation

In the rotary mixer the dispersion of analytes due to the combination of diffusion and convective dispersion is exploited to accelerate mixing. As the Peclet number at which the rotary mixer is operated increases, the dominant mechanism of mixing changes. The scaling laws that determine the mixing time as a function of Peclet number may be determined for three separate regimes of mixer operation.

Very low Peclet number defines a regime of mixing that is dominated by diffusion. In this regime a molecule has ample time to diffuse the full width of the channel before convection can impart any significant downstream displacement. The molecules thus sample the entire flow velocity profile and therefore do not undergo appreciable flow-induced dispersion. The dispersion of a line of tracer particles will therefore be dominated by diffusion and will spread out into a Gaussian distribution centered at $U_{avg}t$:

$$c(z,t) \approx \frac{1}{\sqrt{2\pi DT}} \exp\left(-\frac{\left(z - tU_{avg}\right)^2}{2Dt}\right), \qquad (12)$$

where strict equality holds in the limit of Pe → 0, and U_{avg} is the average flow velocity over the channel cross section. The mixing time at low Peclet number is therefore approximated by the time for a molecule to diffuse the circumference of the ring:

$$\tau_{mix} \approx \frac{\left(2\pi R\right)^2}{D}, \qquad (13)$$

where R is the radius of the mixing ring. Assuming a ring radius of 1 mm, the time require for a salt solution ($D \approx 1000$ $\mu m^2/s$) to be completely mixed is approximately 10 hours.

At intermediate Peclet numbers the dispersion of a slug of tracer molecules is determined by the interplay of diffusion and convection in mass transport as described by Taylor dispersion. The required mixing time at intermediate Peclet number therefore has the dependence

$$\tau_{mix} \propto \frac{(2\pi R)^2}{U_{max}^{\;2} h^2 / Dt} \propto Pe^{-2}. \qquad\qquad \textbf{(14)}$$

A flow of salt solution ($D \approx 1000$ $\mu m^2/s$) at 100 $\mu m/s$ down a channel having a width of 100 μm corresponds to a Peclet number of 10 which is an intermediate value. Once again assuming a ring radius of 1 mm, the time required for complete mixing of this solution is on the order of several minutes.

As mentioned previously, the Taylor dispersion analysis is only valid once the molecules have had sufficient time to sample the entire flow profile so that significant transverse gradients have been eliminated. The periodic boundary conditions imposed in the rotary mixer structure imply that at high Peclet number this condition will not be achieved the ring and mixing is accomplished by a mechanism of "convective stirring." At flow rates where $h^2/D \gg \pi R/U$ tracers will be stretched around the ring before they have a chance to diffuse across the channel. Each circuit of the ring wraps the line of tracer particles back

onto itself in thin interlaced streams. The characteristic distance between these streams decreases linearly with the number of cycles and is given by $d^*=h/2N$, where N is the number of cycles. The mixing time can therefore be approximated as the required time to ensure that the separation distance between streams becomes comparable to the diffusion length. Equating $d^*=(Dt)^{1/2}$ and substituting $N = Ut/2\pi R$ gives (T. Squires and S.R. Quake; Review of Modern Physics, in press)

$$\tau_{mix} \approx \left(\frac{h^2\pi^2 R^2}{DU^2}\right)^{1/3} \propto Pe^{-2/3} \qquad (15)$$

A flow of salt solution ($D \approx 1000$ $\mu m^2/s$) at 5000 $\mu m/s$ down a channel having a width of 100 μm corresponds to a Peclet number of 1000. Assuming a ring radius of 1 mm, a line of salt tracer molecules will make approximately 10 circuits of the loop in the time required to diffuse the full width of the channel. The time for mixing in this situation will therefore be on the order of a second.

The scaling of mixing time with Peclet number is shown in Figure 38. Mixing time may be monotonically decreased by raising the Peclet number within the system. Since the diffusivity is a material property of the particular reagents being mixed, achieving rapid mixing requires either modifying the channel geometry or increasing the flow velocity. The size of the channel directly influences the Peclet number by scaling the appropriate length dimension. Generally, larger channels have higher effective dispersivity. However, at high Peclet number the mixing time has an explicit dependence on the channel critical

dimension. This reflects the fact that the dispersion of molecules is only enhanced in the axial direction.
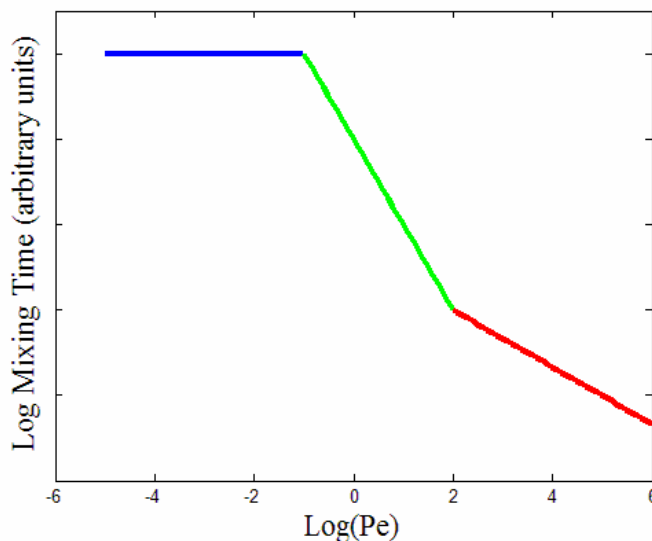
Figure 38: Scaling of mixing time as a function of Peclet number.

Figure 39 shows finite time difference simulations of the evolution of tracer molecules originally occupying half the volume of a rotary mixer. Simulations were performed in MatLab® using a first-order finite time difference algorithm. The script used for these calculations is included in Appendix B. The simulations are carried out for flow velocities $(10 \leq Pe \geq 10\,000)$ chosen to illustrate the transition from the Taylor diffusion regime $(Pe = 10)$ to the "convective stirring" regime $(Pe = 10\,000)$. The simulations show the dramatic enhancement in mixing efficiency as the flow velocity is increased. Also of interest is the delayed mixing within the center of the channel at high Peclet numbers. This effect is due to the direct dependence of mixing time on width and is accentuated by the small velocity gradients present near the channel center.
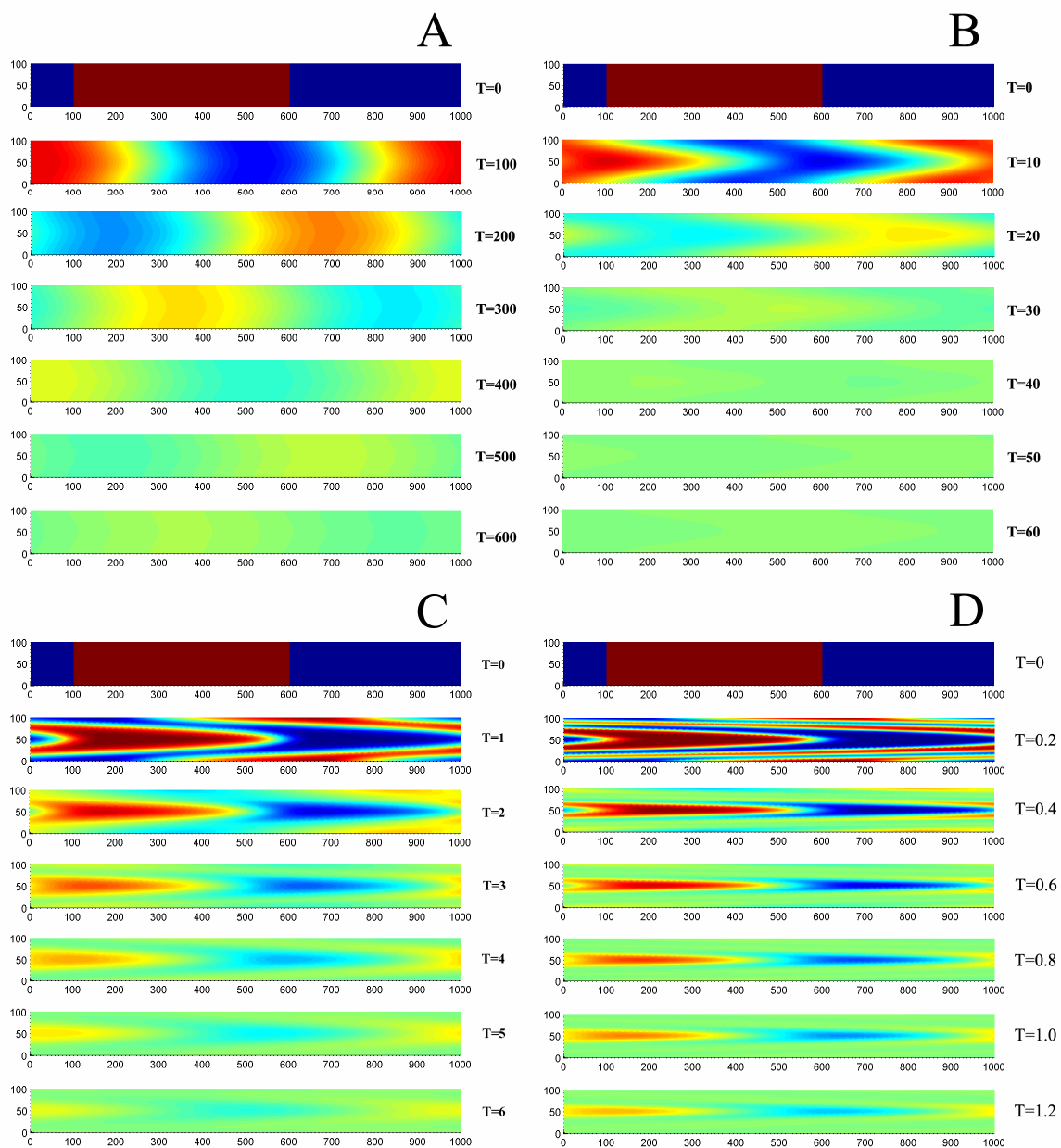
Figure 39: Finite difference time domain simulations of rotary mixer. Evolution of concentration profiles are shown at various times T (seconds). Periodic boundary conditions are imposed at ends of 1000 μm channel to simulate dispersion in ring.

Channel width is 100 μm and diffusion constant is 100 μm²/s so that the Peclet number is equal to maximum flow velocity (A: Pe=10, B: Pe=100, C: Pe=1000, D: Pe=10000).

Fast Valve for Fast Mixing

Regardless of the specific channel geometry, optimal mixing requires that the flow rate be maximized. When operated in the linear regime, the speed of flow driven by a peristaltic pump is proportional to the pump cycle rate so that achieving rapid mixing requires that the valve response be optimized. Actuation of a pneumatic or hydraulic valve requires that a volume of fluid be displaced down the control line to deflect the valve membrane (Figure 40). The valve response is therefore dependent on the speed at which fluid can be pushed in and out to displace the membrane. For low aspect ratio control channels of rectangular cross section the flow rate determining the time constant of actuation can be approximated as (81),

$$Q = \frac{wh^3}{12\mu L}\Delta P \ , \qquad\qquad (16)$$

where Q is the volume flow rate, h is the channel height, w is the channel width, L is the channel length, ΔP is the driving pressure, and μ is the fluid viscosity.
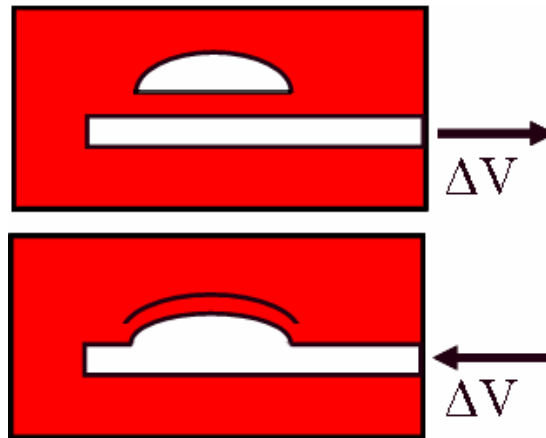
Figure 40: Valve actuation. Opening (top) and closing (bottom) of valve requires transport of finite volume ΔV through control structure.

In order to optimize pumping speed, the control channel height was changed from 10 μm to 25 μm, and ΔP was raised by increasing both the actuation pressure and the fluid pressure by 5 psi. As an added benefit, raising the back-pressure of the fluid was found to suppress the nucleation of air bubbles. This enabled the control line fluid to be changed from water (viscosity 1cP) to air (viscosity 0.01 cP).

Although the use of a compressible fluid (air) in the control lines adds capacitance to the control structure, the greater reduction in fluidic resistance results in a net improvement in response time. The response of the control structure to a pressure input can be modeled as an exponential rise having an RC time constant, with the channel resistance defined by Equation 18 and the channel capacitance defined as the ratio of control volume input to change in pressure. As a first approximation the capacitance of the control structure can be written as the sum of the intrinsic capacitance of the channel structure due to the

compliance of the elastomer (82), the fluid capacitance due to the compressibility of the fluid, and the capacitance due to the expansion of the membrane.

It was determined using absorption measurements that the height of the channel increases by approximately 40% when pressurized to 15 psi. The capacitance of the channel is therefore approximately 0.4 times the channel volume per atmosphere pressure. The capacitance of the membrane is approximately 100 pL per atmosphere and is negligible in comparison. Pressurizing air to 15 psi results in approximately a 50% volume reduction so that the fluid capacitance is approximately the channel volume per atmosphere pressure. The relative increase in capacitance associated with using a compressible fluid instead of water is therefore of order 1 (approximately 3 fold). Therefore, since the viscosity of air is 100 times smaller, the net reduction in the actuation time constant should be on the order of 30 fold. This argument does not include corrections for air permeation into the elastomer which would further slow the response.

The combined effects of changing the fluid control height, changing the actuation fluid, and increasing the back pressure allowed for the pump frequency to be increased from 10 Hz to 100 Hz. At this frequency the valve actuation speed is limited by the maximum frequency of off-chip solenoid actuation. 100 Hz pumping frequency resulted in a maximum flow velocity of approximately 2 cm/s; this represents a 10 fold improvement over previously reported work using similar channel geometries (13, 14). At these flow rates complete mixing of non-viscous reagents is achieved in less then 3 seconds, and solutions with viscosities of approximately 100 cP may be mixed less than 9 seconds.

Chapter 7

SYSTEMATIC SOLUBILITY CHARACTERIZATION: CASE STUDY

The flexibility, precision, fast mixing, and small volume requirements of the formulator device make feasible the systematic mapping of crystallization phase-space. In order to demonstrate the utility of *ab initio* solubility characterization prior to crystallization trials we exhaustively explored the solubility behavior of a commercially available crystallization standard, Endo-1,4-β-xylanase (xylanase) from *Trichoderma reesei* (83, 84). Xylanase is a 21 KDa member of the gluconase enzyme family of industrial interest in the processing of pulp and paper due to its ability to break down xylans. Xylanase was chosen for solubility studies since it is stable for long periods of time at room temperature, and is known to be more challenging to crystallize than other crystallization standards.

Endo-1,4-β-xylanase (xylanase) from *Trichoderma reesei* (Hampton Research) was prepared in deionized water from stock (36 mg/mL protein, 43% wt/vol glycerol, 0.18 M sodium/potassium phosphate pH 7.0) by repeated buffer exchange at 4 C using a centrifugal filter with a molecular weight cutoff of 10,000 Da (Micon Bioseparations). Protein concentration was measured by absorption at 280 nm and adjusted to 120 mg/mL. 10 μL aliquots were flash frozen in liquid nitrogen and stored at −80 °C. To avoid sample-sample variations, a single sample preparation was used for all solubility screening, phase-space mapping and corresponding crystallization experiments.

Automation and Data Aquisition

Automation of metering, mixing and data acquisition allows for thousands of solubility experiments to be executed without the need for user intervention. In each solubility experiment a unique mixture of the 32 reagents and the protein sample is produced. All device control and data acquisition was implemented using a custom software driver developed in LabView (National Instruments). Mixing recipes were generated using a spread-sheet program and translated into valve actuation sequences by the software driver. Off-chip solonoid valves (Lee Products Ltd.), controlled using a digital input output card (DIO-32HS; National Instruments), were used to generate square-wave pressure signals at the device control ports. A frame-grabber card (Imagenation PXC200A; CyberOptics) was used to automate image acquisition from a charge coupled device camera.

Precipitation Detection

Precipitation of the protein was automatically detected by imaging a portion of the mixing ring, calculating the standard deviation of the pixel intensities and comparing this value to the background (no protein added). To ensure even illumination, images were taken at 112 times magnification at a 9 μm high section of the mixing ring having rectangular cross section. As a metric of precipitation, the standard deviation of imaged pixels not only allows for distinction between precipitated and soluble conditions, but further allows for a rough quantitative measure of the degree of precipitation. Beyond the precipitation limit, the pixel standard deviation increases linearly with the protein concentration, and therefore is proportional to the concentration of precipitated protein present in the solution (Figure

41). A video of on-chip protein titration and precipitation is included as supporting information.
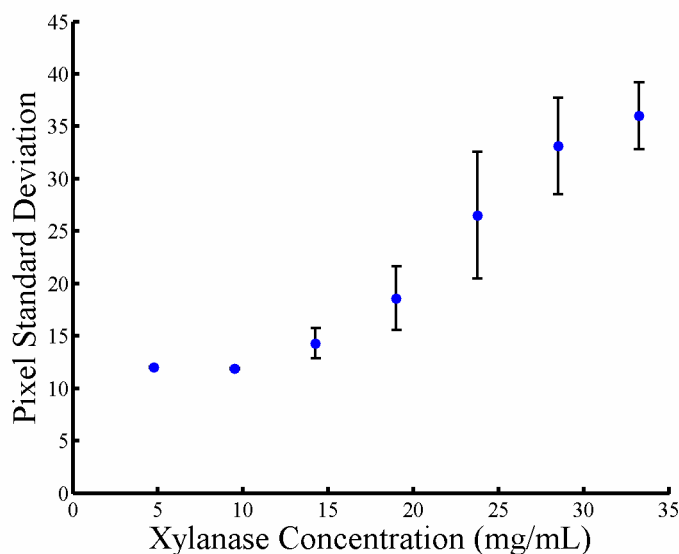
Figure 41: Precipitation measurements at varying concentration of xylanase in 0.6 M potassium phosphate with 0.1 M TRIS/HCl pH 6.5. Standard deviation of pixels provides a quantitative metric of protein precipitation. Below the precipitation limit standard deviation shows constant background level with low variation. Above 12 mg/mL solution is in the precipitation regime where the pixel standard deviation exhibits an approximately linear dependence on protein concentration. All points represent the mean of 5 identical experiments with error bars indicating standard deviation of measurements.

Solubility Fingerprinting

A two-step protocol was used to map out the solubility space. An initial coarse search was used to identify reagents that have a strong precipitating effect on the target macromolecule. In this step concentrated protein sample is combined with a wide range of potential precipitating agents (chemical conditions) at high concentrations. This generates a solubility fingerprint of the crystallization target. Each precipitation peak in this fingerprint represents a chemical condition that exerts a pronounced effect on solubility. Chemical conditions that do not result in protein aggregation even at high concentrations are dismissed as unlikely crystallizing agents and are not explored further.

The solubility fingerprint of xylanase generated by 4 independent runs, each consisting of approximately 4000 titration experiments, is shown in Figure 42. This fingerprint is highly reproducible and is characteristic of the protein studied. The chemical conditions tested in Figure 42 were grouped by the identity of the major precipitating agent so that each peak represents the effect of this reagent over a range of pH values and concentrations. The large width of these peaks indicates a high level of experimental redundancy, suggesting that a more efficient search could be conducted using less related chemical conditions.
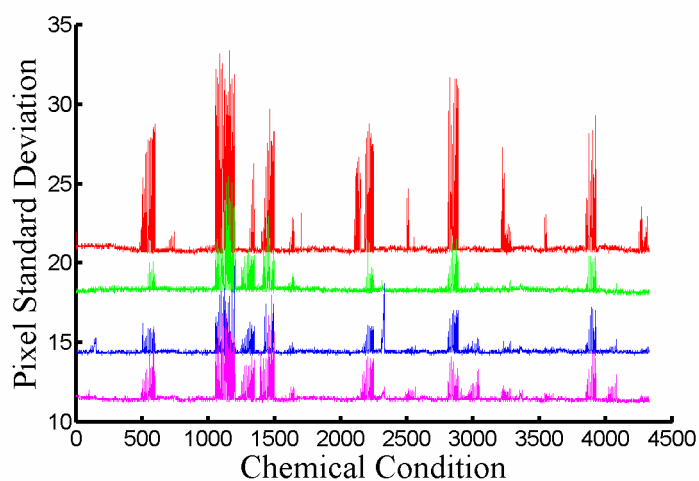
Figure 42: Solubility fingerprints of xylanase over approximately 4200 chemical conditions. Each data series represents a separate fingerprinting experiment using the same basis of chemical conditions. The top solubility fingerprint (blue), generated using a sample having elevated protein concentration (90 mg/mL), exhibits both higher signal to noise and additional peaks not present in the other data series (70 mg/mL). The two center solubility fingerprints were generated sequentially on a single device (first orange, then green) with the same loaded sample, demonstrating the stability of the protein over the time of the experiment (approximately 20 hours). The bottom solubility fingerprint (red) was generated using the same sample as orange on a separate device, showing reproducibility across devices.

The solubility fingerprint of xylanase revealed 5 salts (sodium citrate, di-potassium phosphate, ammonium sulfate, and sodium/potassium tartrate) as likely crystallizing agents. A high molecular weight polymer (polyethelyne glycol 8,000) in combination with

various salt additives was also identified to be a strong precipitating agent at high pH values. The high isoelectric point of xylanase suggests that the reduced effectiveness of this precipitant at low pH values is due two-body electrostatic repulsion. A smaller molecular weight polymer (polyethelyne glycol 3,350) was found to be a much weaker precipitating agent and was not investigated further in phase-space mapping experiments.

Protein Phase-space Mapping

The identified xylanase precipitating conditions were expanded in 24 systematic grid searches over all accessible protein and precipitant concentrations. Each grid consists of 72 separate mixing experiments, creating a two-dimensional phase-space with protein concentration and precipitant concentration as variables. All 24 phase-spaces were generated sequentially on a single device using less than 3 uL of protein sample (approximately 100 nL per phase-space) and are included in Appendix C. A comparison of precipitation phase-spaces measured for xylanase in chip (5 nL reactions) and in microbatch format under paraffin oil (5 μL reactions) shows good agreement in detecting the precipitation boundary (Figure 43). Since measurements of precipitation are made immediately after mixing (within 3 seconds), the locus of points that separate the precipitated and soluble regions of the graph generate a precipitation curve that is distinct from the thermodynamic solubility curve. Conditions that reside just below the precipitated region may be in a metastable state conducive to crystallization.
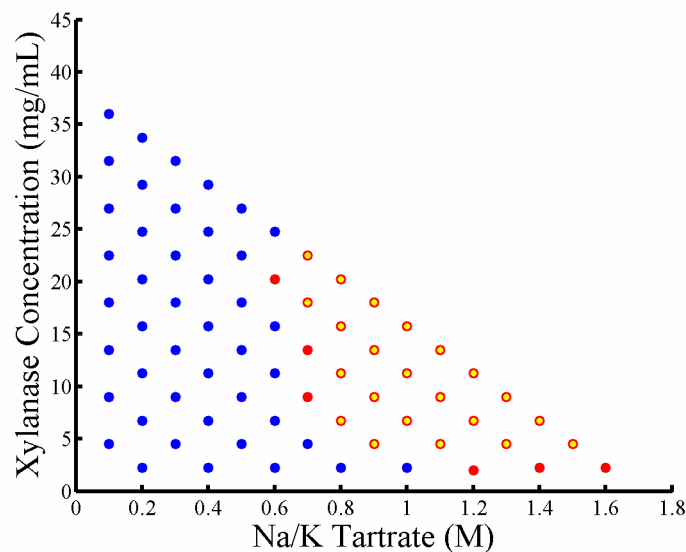
Figure 43: Comparison of phase mapping done on chip (small yellow circles) and in microbatch (large red circles) experiments. Microbatch experiments were set at a final volume of 2 μL and actively mixed under oil by repeated aspiration with a pipette.

Solubility Hysteresis

The formulator has been used to make a direct observation of the supersaturation region of chicken egg white lysozyme. The concentrations of salt and lysosyme were manipulated while keeping the buffer concentration constant in order to evolve the chemical state of the mixing ring radially out from the origin and then back again. Measurements of precipitation were taken at approximately 1 minute intervals. The addition of a family of such radial titrations was used to generate two phase-space diagrams for chicken egg white lysosyme; one for the outward titrations and one for the return titrations (Figure 44). The first observation of protein precipitation appears at higher salt and protein concentration during the outward trajectory than on the return path, thereby exhibiting solubility

hysteresis. The intersection of the soluble region of the outward phase-space with the precipitated region of the return path phase-space provides a direct observation of a metastable regime in which the aggregate phase is thermodynamically stable but not observed at short times. The observation of the reversible formation of a protein aggregate may be used to distinguish between denatured and well-folded protein aggregates. Additionally, identified metastable regions in phase-space provide likely candidates for crystal seeding and growth experiments.
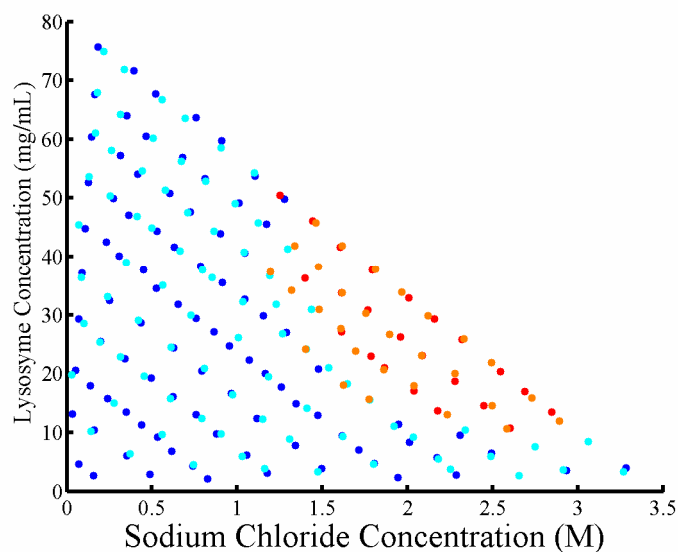
Figure 44: Overlay of two phase-space diagrams generated by outward and return titrations. Observed hysteresis in precipitation threshold identifies metastable region of phase-space.

Optimal Crystallization Screening

A detailed knowledge of protein solubility behavior provides an empirical basis for the design of maximum likelihood crystallization trials. The 24 phase-spaces generated for xylanase were used to design an optimal crystallization screen consisting of 48 reagents. A single batch crystallization trial using the optimal screen was set by combining relative amounts of protein and precipitant stock so that the final condition was located on the boundary of the precipitation region. The efficiency of this screen was evaluated by comparison with standard commercially available sparse matrix screens (Crystal Screen I, Crystal Screen II; Hampton Research, Wizard I, Wizard II; Emerald Biostructures). 2 batch crystallization trials of 48 unique conditions were prepared for each of the 4 sparse matrix screens for a total of 384 individual assays. For each commercial screen final protein concentrations of 12.5 mg/mL and 25 mg/mL were used; the recommended concentration range for the crystallization of xylanase is 10 mg/mL to 40 mg/mL. All batch crystallization trials were actively mixed by repeated aspiration and incubated under paraffin oil. Crystallization trials were inspected daily for a period of two weeks. Observed crystals were confirmed to be protein crystals by staining (IZIT dye; Hampton Research) and were recorded as crystallization hits. The optimal screen formulations and crystallization results are listed in Appendix D.

Twenty-seven crystallization conditions were observed in the optimal screen compared to a total of 3 crystallization conditions in the 8 standard sparse matrix screens. The use of *ab initio* solubility information therefore resulted in a 72-fold enrichment in crystallization success (Figure 45). A surprising result was that xylanase crystals were observed in the

optimal screen for all the precipitants identified in coarse screening. These results suggest that achieving optimal levels of supersaturation is more important in the crystallization of xylanase than is the broad sampling of chemical space. Additionally, crystallization conditions were identified in the optimal screen that gave large single three-dimensional crystals (Figure 45B); flat plate clusters were observed in the standard screens.
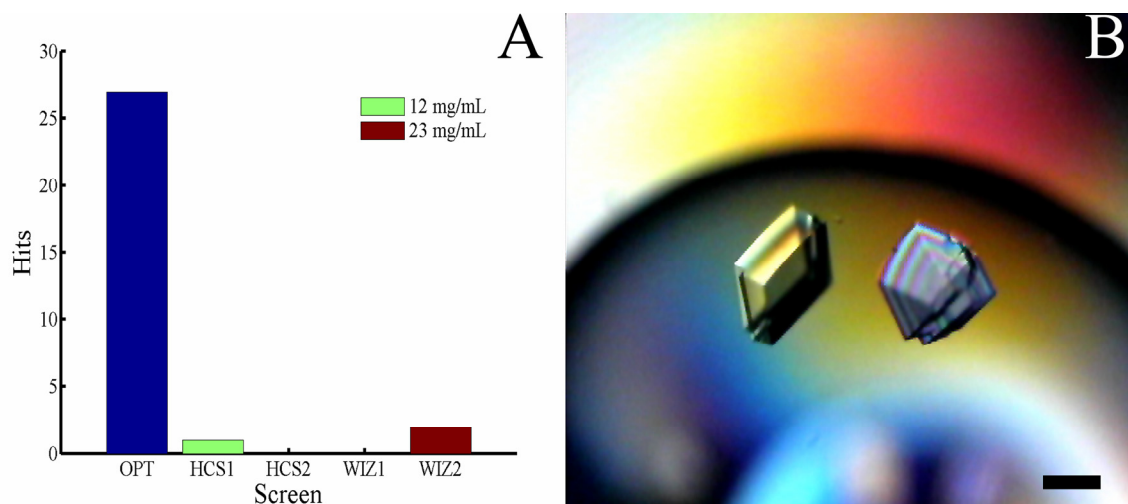
Figure 45: Comparison of microbatch crystallization experiments using commercially available sparse matrix screens to an optimal crystallization screen based on solubility phase-spaces. **(A)** Histogram showing number of successful crystallization conditions identified with sparse matrix screens (each at protein concentrations of 12 mg/mL and 23 mg/mL) and optimal screen. **(B)** Polarized micrograph of large single crystals grown directly from optimal screen (16% polyethelyne glycol 8000, 65 mM sodium chloride, 65 mM TRIS-HCl pH 8.2, 42 mg/mL xylanase). Scale bar is 100 μm.

Crystallization Variability

Subsequent crystallization experiments based on the optimal screen were repeated using different protein sample obtained from the same vendor and prepared in the same way as the original sample. 14 of 17 polyethelyne glycol conditions that gave crystals in the original experiment were reproduced using the second sample, compared to 1 of 10 for the salt based conditions. To determine if this discrepancy was due to variations in phase-space behavior a complete phase-space of one condition (sodium/potassium tartrate, TRIS·HCl pH 8.5) was measured in microbatch format for both samples (Figure 46). It was discovered that although both samples exhibited comparable phase-space behavior they produced vastly different crystallization results. The reason for this difference in behavior is unclear but may be due to slight sample-sample variations or trace amounts of chemical contaminants introduced during purification or concentration steps. It is interesting that some crystallization conditions (those based on PEG 8000) may be more robust to batch-dependent perturbations.
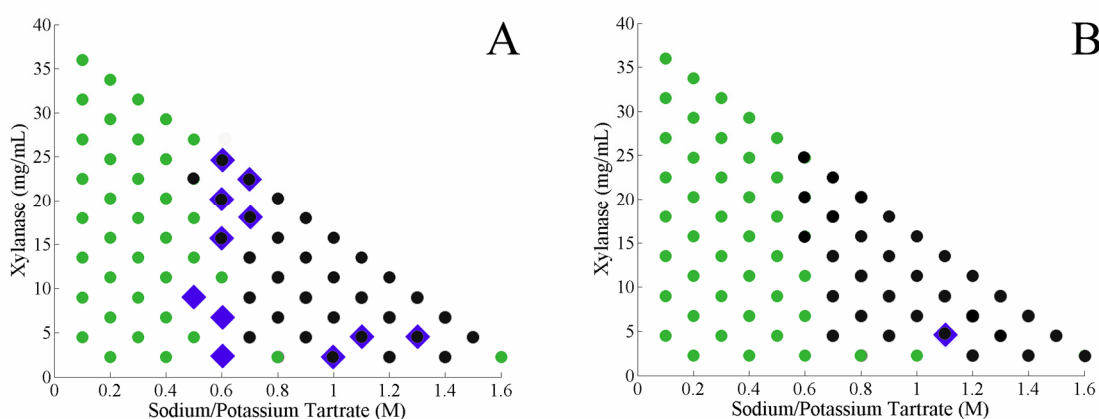
Figure 46: Crystallization variability. Two phase-space mapping and crystallization experiments with different batches of Xylanase. All experiments were set in microbatch format under paraffin oil with a final volume of 2 μL. Active mixing by repeated aspiration through a pipette was used. Location of soluble (green circles) and precipitation (black circles) conditions correspond well between batches. Crystallization conditions (blue diamonds) were observed after one week of incubation.

Another application of protein solubility phase-space mapping is in transporting successful crystallization conditions from one experimental format to another. The successful crystallization of a protein is determined both by the established thermodynamic variables and the kinetic trajectory of an experiment. For this reason experiments conducted with different crystallization kinetics (e.g., Hanging drop vapor diffusion, microbatch, free-interface diffusion) using the same precipitating agents will not necessarily produce similar results. For example, the hydroxylase domain of a cytochrome p450 alkane hydroxylase (Mutant 139-3 of BM-3) did not produce crystals in initial hanging drop trials, but was found to crystallize readily by microfluidic free interface diffusion (29) (1 part protein 20 mg/mL, 1 part 30% m/v polyethelyne glycol 8000, 0.2 M sodium acetate, 0.1 M TRIS-HCl pH 7.0). This condition was unsuccessful when set in hanging drop vapor diffusion format, resulting only in amorphous precipitate. The microfluidic formulator was used to generate a phase-space at constant buffer and salt concentration (100 mM TRIS-HCl pH 7.3; 200 mM sodium acetate) with polyethelene glycol concentration and protein concentration as variables. Two hanging drop experiments were designed to equilibrate near the solubility limit determined from the phase-space map. One condition (8 μL of 35 mg/mL protein

sample mixed with 6.7 µL of 10% polyethelene glycol, 100 mM sodium acetate, 50 mM TRIS-HCl pH 7.3, and equilibrated at 20 °C against 1 mM of 20% polyethelene glycol, 200 mm sodium acetate, 100 mM TRIS-HCl pH 7.3) produced crystals within 3 days. This success demonstrates the usefulness of solubility mapping in transporting conditions across crystallization formats.

Chapter 8

CLEAR PATH TO STRUCTURE

Introduction

Nanoliter-scale protein crystallization screening in μFID reactors has proven a powerful technique for identifying protein crystallization conditions over a broad range of challenging crystallization targets. In particular, the ability to screen very small sample volumes and the number of successful crystallization studies with targets that have proven intractable by conventional screening techniques highlights the potential of this technology to have a large impact on structural biology. The realization of this potential however depends crucially on establishing a clear path from chip-based crystallization to structure. This Chapter discusses the ongoing development of general methods for growing high-quality crystals of sufficient size for diffraction studies, and harvesting these crystals without damaging them.

Direct Harvesting from Screening Devices

Once crystallization conditions giving rise to high-quality crystals are determined in chip-based screening experiments a method must exist for getting crystals into the x-ray beam. The most direct of these methods is the extraction of crystals from screening devices. Despite the small volumes, crystals of sufficient size for crystallographic structure determination may be grown and harvested directly from the chip. Figure 47 shows a high-resolution diffraction pattern for a single thaumatin crystal grown from only 5nL of protein solution (29). Crystals were exposed by separating the microfluidic device from a glass

substrate containing microfabricated reaction chambers, cryo-protectant was dispensed on the reaction wells, and the crystals were harvested using conventional cryo-loops.
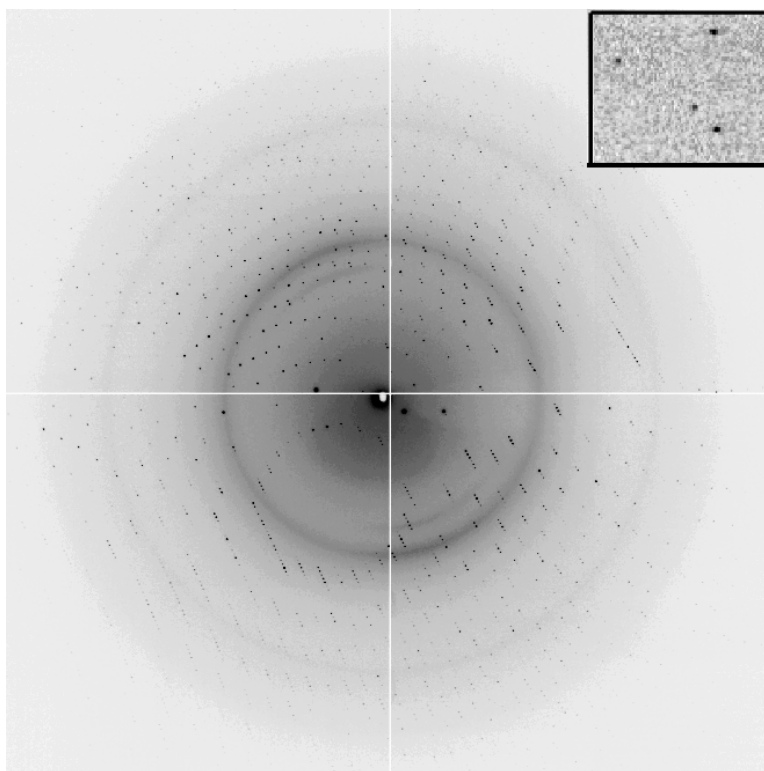
Figure 47: X-ray diffraction pattern (resolution < 1.35 A$^{\circ}$) from a single thaumatin crystal grown from 5 nL of sample in chip. The inset shows a clean reflection at 1.35 A$^{\circ}$ resolution. Diffraction data was collected at station 8.3.1 of the Advanced Light Source (ALS) at an incident wavelength of 1 Å, with a 20 s exposure and 1° oscillation.

The high-resolution data obtained from chip-grown thaumatin crystals exceeds that reported of crystals grown by conventional ground-based techniques, and is comparable to that obtained from thaumatin crystals grown in space (85). In general crystallization

experiments in space have suggested that microgravity environments may be well suited for the growth of large, high-quality crystals (48, 85-87). The mechanism for the increased order of space-grown crystals is not completely known but is largely attributed the lack of buoyancy-driven convection during crystal growth, an effect also present in terrestrial microfluidic devices. (88-90).

High-resolution diffraction data has been collected from crystals of several protein models extracted directly from chip (lysozyme, glucose isomerase, ferritin, bovine liver catalase). Despite this success, the direct extraction of protein crystals from screening devices is a delicate and time-consuming procedure that has not proven to be generally applicable. For instance, large single crystals of a type II topoisomerase ATPase domain extracted from a screening device diffracted to only 3.5 Å; crystals grown from the same condition in hanging drop experiments diffracted to 2.0 Å (personal communication with K. Corbett). Several technical problems make this method prone to damaging crystals, thereby compromising their diffracting power.

Chemical variations and osmotic shock introduced during harvesting can severely reduce the diffracting power of a crystal. This mechanism is particularly important in nanoliter volume screening devices due to the large surface to volume ratio of the reactors and the permeability of the elastomer material.

Permeability Effects

In addition to equilibration by free interface diffusion, chip-based reactions are subject to slow hydration/dehydration due to vapor diffusion through the elastomer chip. The magnitude of this effect is determined by a complicated interplay of chemical, material, geometric, and environmental factors. The transport of water vapor through the elastomer device is governed by the diffusion equation :

$$\frac{\partial P}{\partial t} = K_P \nabla^2 P \ , \qquad\qquad (17)$$

where P is the partial pressure of water vapor, and K_P is the permeability of the elastomer to water vapor. This equation is valid within the bulk of the elastomer device. An exact solution to this equation is made difficult due to the three-dimensional geometry and the complex time-varying boundary conditions. The problem is directly analogous to a heat-flux problem and is illustrated in Figure 48 below.
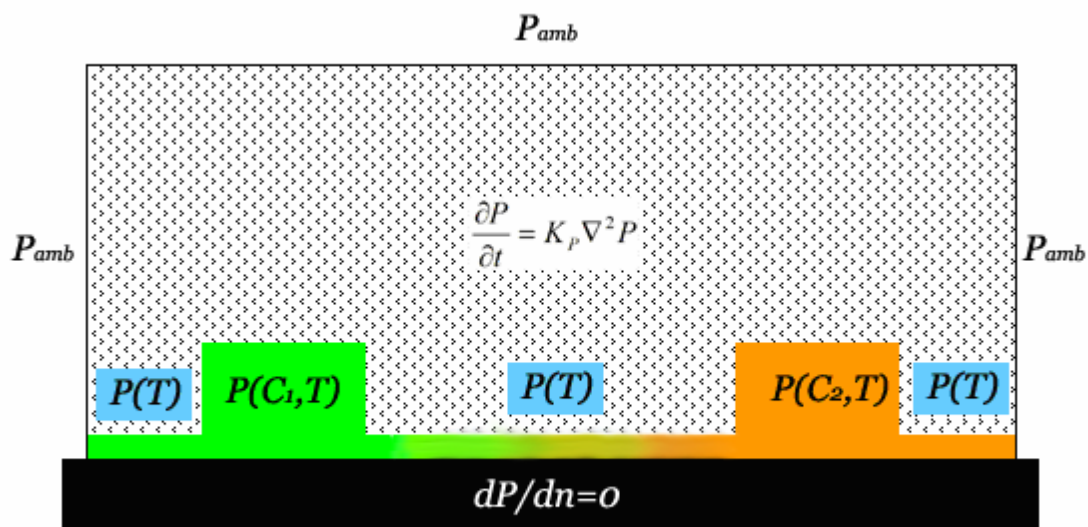
Figure 48: Schematic showing boundary conditions influencing the transport of water vapor through the bulk elastomer. The control lines (blue) are filled with dionized water and serve as sources of water vapor. The vapor pressures of the reagents (orange and green) and control fluids are a strong function of temperature. Additionally, the vapor pressure of the reagents is a function of the concentration of species and hence changes due to both counter-diffusion and hydration/dehydration. The underlying glass substrate (black) imposes a no-flux condition.

The partial pressure at the chip surface is determined by the ambient room conditions and hence may be time-varying. A no-flux condition is present at the bottom of the chip due to the low permeability of the glass substrate. Additional boundary conditions at the flow channel, control channel, and microwell surfaces are determined by the vapor pressure of the various reagents and control fluids. The vapor pressure of the reagents within the flow

structure is a function of the identity and concentration of reagents, and hence is time varying due to diffusive mixing and concentration/dilution effects. The vapor pressure of a solution is approximated by Raoult's law:

$$P = P_0 - P_0 \frac{\Sigma_{i=1}^{\sigma} N_i}{N_0} \quad , \tag{18}$$

where P is the vapor pressure of the solution, P_0 is the vapor pressure of the pure solvent, N_i is the molarity of the solute, and N_0 is the molarity of the solvent (55.346 mol/L for water).

In normal chip operation the control fluid is chosen to be dionized water and is constantly replenished through the control line port. The control lines therefore define the boundary condition of maximal partial pressure and provide a constant source of water vapor. This ensures a constant flux of water vapor from the control lines into the reagent wells and out of the chip. As the system evolves towards steady state the reagents within the wells will asymptotically approach a vapor pressure that gives rise to zero net vapor flux. This implies that at long times the final vapor pressure of each reaction, and hence the level of dehydration, will be determined solely by the ambient conditions and the device geometry. An important point is that the samples do not dehydrate completely, but rather converge to a condition of dynamic equilibrium in which all the reactors assume the same osmotic strength irrespective of the mixing ratio or chemistry. For example, screening devices with crystals of MscL and hdTfR/HFE have been incubated for several months with no apparent change in hydration and no observed degradation of crystals.

It is worth noting that the vapor pressure of an aqueous solution is a strong function of temperature, varying over four-fold from 5 °C (P_{vap} = 6.54 mmHg) to 25 °C (P_{vap} = 27.76 mmHg). This effect results in dramatically different rates and final levels of dehydration between devices incubated at 4 °C and 20 °C. The rate of evaporation from the control structure of a screening device was measured by tracking the meniscus of the control input line over time. Dehydration rates of approximately 8 µL/day were typical of devices incubated at 20 °C compared to rates of 1 ± 1 µL/day in devices incubated at 4 °C.

In the screening device the timescale for evaporative equilibration is on the order of one to several days, making it comparable to or slower than the diffusive equilibration of precipitating agents between wells. This process therefore results a continued slow evolution of the conditions through chemical phase-space after diffusive equilibration is complete. This continual sampling of phase-space is likely a major factor in the observation of crystallization events that occur at long incubation times, and hence increases the number of detected hits. However, since the rate and final extent of evaporation depends in a complex way on the chip geometry, reagent chemistry, and ambient conditions, it is not easily characterized over the large number of unique screening conditions used in chip. For this reason it may be difficult to ascertain the precise chemical condition that gave rise to crystallization events in screening devices at long incubation times. This uncertainty complicates both the transport of chip-based conditions to alternative formats and the harvesting of crystals.

The transport of water vapor during the crystallization process results in a richer phase-space evolution, giving rise to more crystallization hits, but also introduces uncertainty in the exact chemical state of each reactor. Uncertainty in the concentration of chemical species is particularly problematic in the formulation of an appropriate cryo-protectant for harvesting. This problem is further exasperated by the very small volume of the reagent wells since the addition of a microliter of mother liquor or cryo-protectant to a nanoliter volume crystallization mixture results in an abrupt change in the concentration of the reagents.

Mechanical damage is another cause of reduced crystal diffracting power. Physical manipulations during the looping of delicate crystals from solution (common practice in conventional harvesting) can fracture or crack fragile crystals (especially for thin rods or plates). The degree of mechanical damage that occurs during the conventional harvesting of crystals is not well characterized but is thought to be tolerable for all but the most fragile of crystals. The additional manipulations required to extract crystals from screening devices present more severe risks. Peeling away the elastomer to expose the crystallization wells can result in crystals being carried away with the fluid or crushed between the chip and the substrate. Furthermore, crystals that adhere to the walls of the chip or the substrate are difficult to remove without cracking or crushing them.

Finally, harvesting crystals from screening chips necessitates peeling off the entire device or cutting the control lines. This imposes impractical constraints on harvesting since the entire device must be sacrificed for the harvesting of a single well; crystals can not be

harvested from different reactors at optimal times. The potential for inducing chemical and mechanical damage along with the aforementioned technical complications therefore make direct extraction from the screening device suitable for only the most robust of crystals.

Transporting Conditions to Conventional Formats

In cases where crystal growth occurs at low supersaturation levels, or where the absolute concentration of protein is low, it may be necessary to transfer conditions to larger volume formats in order to produce crystals of sufficient size for diffraction studies. Additionally, once crystallization conditions are transported to conventional microbatch or vapor diffusion formats harvesting may be accomplished by well-established conventional techniques. Since the success and quality of crystal growth is governed both by the chemistry and the mixing kinetics of an experiment, transferring chip-based crystallization conditions to conventional formats may not be straightforward. Furthermore the transport of water vapor through the elastomer may introduce uncertainty in the exact concentration of reagents that gave rise to crystallization

The success rate of directly transferring crystallization conditions form the chip to hanging drop vapor diffusion or microbatch techniques was investigated using 4 crystallization standards (beef liver catalase, proteinase K, glucose isomerase, and bovine pancreas trypsin) (experiments conducted at Fluidigm corporation). All four proteins were tested in crystallization trials using a commercially available sparse matrix screen (Crystal Screen; Hampton Research). The results of these experiments are displayed in Venne diagrams in Figure 49. In these experiments the rate of successfully transferring conditions directly

from the chip to hanging drop vapor diffusion format was 66 %. The rate of transferring to microbatch format was comparable at 56 %. This high success rate reflects the ease with which these model proteins can be crystallized. Although no systematic study has been done, the success rate of transferring conditions directly from chip to conventional formats is estimated by the author to be much lower for more challenging crystallization targets (approximately 20 %).

Bovine Pancreas Trypsin   Protease K

Glucose Isomerase   Beef Liver Catalase
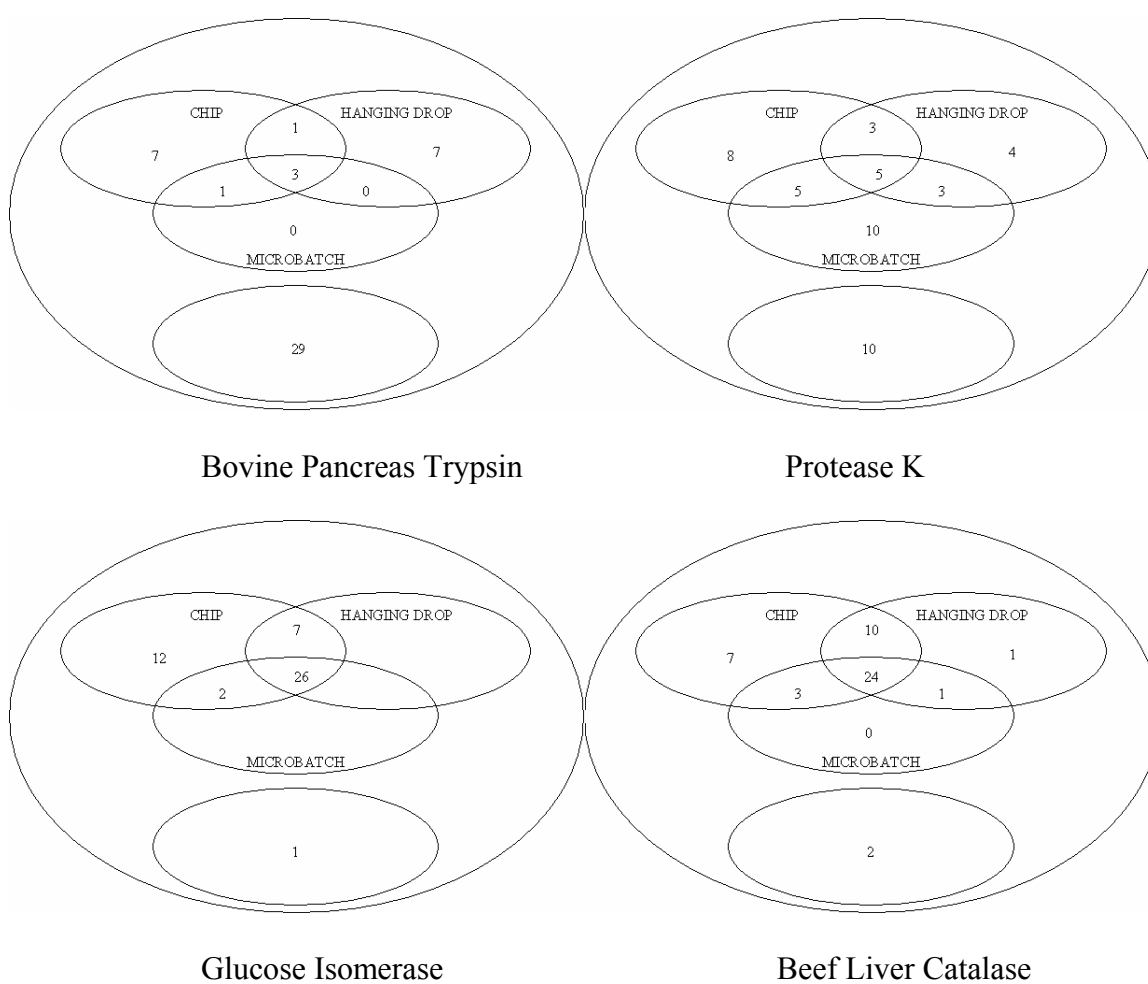
Figure 49: Venne diagrams showing correspondence between chip, microbatch, and hanging drop vapor diffusion formats.

If directly transporting conditions is not successful, identified chip-based crystallization conditions nevertheless provide valuable information that can be leveraged for conducting efficient crystallization trials in conventional formats. Firstly, chip-based experiments provide an excellent way to efficiently evaluate the crystallizability of a target using small amounts of sample. This is particularly useful in cases were many othologues or constructs of a target are being pursued in parallel. Secondly, identifying successful precipitating agents dramatically reduces the chemical space that must be explored in crystal trials. This allows for a more refined search of the relevant parameters, greatly increasing the chance of success. Highly resolved and systematic screening based on crystallization conditions optimized in chip has been used to successfully transport conditions to microbatch or vapor diffusion formats. In experiments conducted at UC Berkeley 5 of 6 target proteins that were initially crystallized in chip were transported to conventional formats (JM Berger, personal communication). It is expected that current efforts directed towards more thorough characterization and modeling of chip equilibration will allow for the development of systematic protocols for transporting conditions between chip and standard formats.

Scaling up µFID Reactions

In cases were systematic screening fails to identify crystallization conditions in conventional formats the success of crystallization may depend on the unique equilibration kinetics achieved in chip. The slow diffusive mixing achieved in chip provides both a continuous sampling of chemical phase-space and eliminates rapid initial precipitation.

Preserving the mixing kinetics achieved in chip is therefore crucial in attempts to scale up μFID crystallization reactions with high correspondence.

Conventional free interface diffusion achieves high transient levels of supersaturation but has a complicated spatial/temporal gradient due to the constant cross section of the capillary. This gradient couples the kinetics and thermodynamics of traditional free interface diffusion assays in a way that μFID does not. In the μFID assay, the fluidic interface is established between the two wells in a constricted channel where the cross section is 10 μm x 100 μm. In contrast, the cross section of a well is approximately 300 μm x 100 μm. This constriction acts as a high-impedance connection between the two channels, localizing the concentration gradient only to the length of the connecting channel. Figure 50 shows a finite difference time domain simulation of the diffusive equilibration of a low molecular weight dye in two microwells coupled by a constricted channel (PDE Toolbox, MATLAB®; The MathWorks Inc. of Natick, Mass.). With the exception of the region in close proximity to the inlet, no appreciable concentration gradient forms in the microwell itself. In a protein crystallization experiment, this implies that as the wells equilibrate, the vast majority of the sample evolves simultaneously through a continuum of thermodynamic conditions.
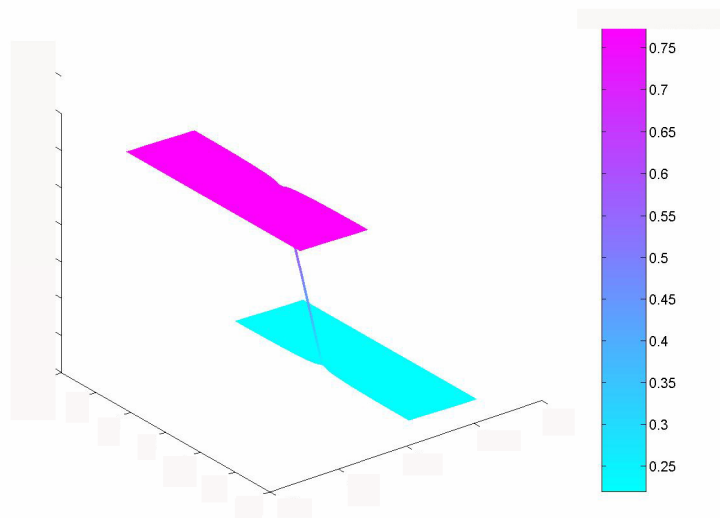
Figure 50: Two-dimensional finite element modeling of diffusion of an organic dye in aqueous solution between two microwells connected by a constricted channel. Simulation shows the bulk of the concentration drop occurring along the channel with no appreciable gradient within the microwells. For modeling purposes, constriction of the channel in the vertical dimension has been represented by a lateral constriction. Concentrations are normalized to a maximum of 1 (arbitrary units).

In the optimization of crystallization conditions, it is often desirable to slow down the equilibration process so that favorable conditions are approached more slowly to produce fewer nucleation events and larger crystals. In vapor diffusion experiments, this can be achieved by methods such as placing a thin layer of semi-permeable oil over the precipitant, increasing the size of the crystallization drop to slow equilibration, or by inclusion of a chemical additive such as glycerol to the crystallization drop in order to reduce the vapor pressure. While these techniques are effective in slowing down the

equilibration of the drop with the reservoir, they allow for only coarse control of the equilibration kinetics. Conversely, microfluidic free interface diffusion allows for precise and straightforward control of the equilibration rate while decoupling the kinetics and thermodynamics of crystallization.

The absence of any spatial gradient within the microwells allows for a simple analytical solution of the time-dependent evolution of the concentration in each chamber. The net transport of a diffusing species along the channel is equal to the product of the diffusive current density and the channel cross sectional area. Since the channel is constricted in both height and width, the problem is one-dimensional and the gradient along the channel is given by the difference in concentration divided by the channel length. The equation governing the change of concentration in a well of volume V_1 and concentration $C_1(t)$ that is coupled to a second well of volume V_2 at concentration $C_2(t)$ is therefore given by

$$\frac{dC_1(t)}{dt} = -DA\frac{C_1(t) - C_2(t)}{V_1 L},\qquad\qquad \textbf{(19)}$$

where D is the diffusion constant of the species. Integration of this equation and application of the initial conditions $C_1(0) = C_0$, $C_2(0) = 0$, gives

$$C_1 = \frac{C_0}{1 + V_2/V_1} + \frac{C_0}{1 + V_1/V_2} * Exp\left[-D\frac{V_1 + V_2}{V_2}\frac{1}{L}\frac{A}{V_1}t\right].\quad \textbf{(20)}$$

From this equation, it can be seen that for a given diffusion constant and relative well volume, the rate of equilibration depends only on two characteristic lengths: the length of the connecting channel, and the ratio of the well volume to channel cross sectional area. Thus, modifying the channel geometry allows for intuitive and accurate control over the kinetics of diffusive equilibration without changing the chemistry of the solutions. For example, by making the channel twice as long the reaction proceeds at one half the rate, whereas reducing the channel cross sectional area by a factor of two increases the equilibration time by the same factor. Furthermore, since these length scales only scale time in the exponent, the locus of concentrations (path through phase-space) achieved during a complete equilibration depends only on the diffusion constants of the species and the relative volume of the wells, and is independent of the channel geometry. The decoupling of the kinetics and thermodynamics of diffusive equilibration has important implications in crystal optimization where it is often desirable to slowly approach crystallization conditions while conserving the successful thermodynamic variables.

Growth Device

The analysis above suggests that a simple scaling of the reaction well volumes will provide a high-correspondence method by which screening chip crystallization hits can be transported to larger volume formats. To test this hypothesis a growth chip device was designed having larger-volume wells and a variety of connecting channel lengths designed to explore the effect of varying mixing kinetics on crystallization. The device features 8 reaction sites having 5 different mixing ratios and 4 different connecting channel lengths

(Figure 51). The volume of each well is designed to be approximately 300 nL, approximately a 30 fold increase over the screening chip format.
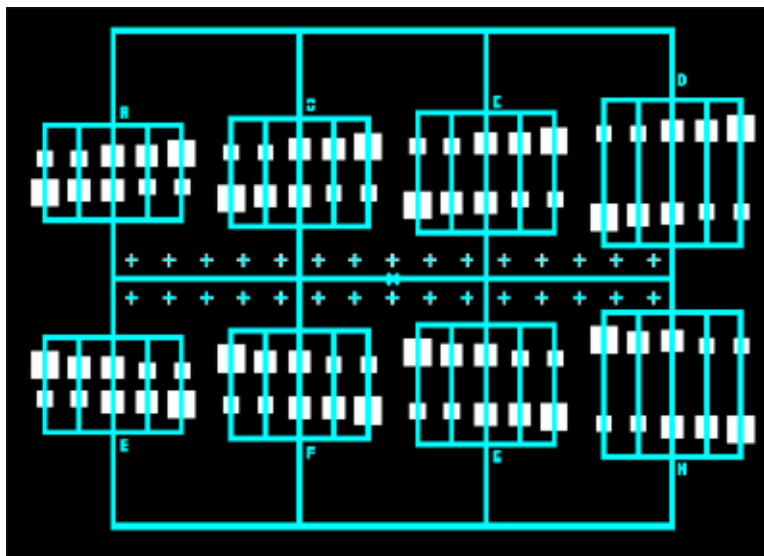
Figure 51: Layout of growth device featuring different mixing ratios and connecting channel geometries.

A series of crystallization experiments were conducted using 7 model proteins that had been successfully crystallized in the small-volume screening device. These models included DNA B/C, Rho, hdTfR/HFE, P450 1-12G (hydroxylase domain), P450 139-3 (hydroxylase domain), DNA D/G/H and MscL. Of these models, four (DNA B/C, hdTfR/HFE, P450 1-12G) had resisted attempts at transferring to hanging-drop vapor diffusion by screening around chip-based conditions. In the case of P450 139-3 vapor diffusion crystallization was achieved by using solubility information derived from

formulator device experiments. Crystallization of the remaining three proteins had been achieved in hanging drop format.

Rho is a RNA/DNA helicase factor responsible for transcriptional termination in bacteria. Rho was first crystallized in vapor diffusion format through extensive screening (91) using conventional methods and then transferred directly to the screening device. In the case of MscL successful vapor diffusion conditions were discovered and optimized prior to identifying conditions independently (including some novel conditions) using sparse matrix chip-based screening experiments. The first crystallization conditions for DNA D/G/H were found using the screening device after extensive unsuccessful conventional screening. This condition was eventually used to achieve crystallization in vapor diffusion format by very refined systematic screening around the identified chip condition. The results of crystallization trials for these three proteins are summarized in Table 2.

Protein	Vapor Diffusion	Growth Chip
DNA B/C	NO	YES
Rho	YES	YES
hdTfR/HFE	NO	NO
P450 1-12G	NO	NO
P450 139-3	YES	YES
DNA D/G/H	YES	YES
MscL	YES	YES

Table 2: Transfer of crystallization conditions using growth device.

Screening around chip-based conditions was found to have a success rate that is comparable to growth chip experiments using the exact chip-based condition. Since no additional chemical optimization was used in growth-chip experiments (although the kinetic variable was manipulated) this result supports the hypothesis that the slow diffusive equilibration between wells allows for more efficient sampling of crystallization phase-space. The overall success rate of the growth chip from this trial was 67 %.

Consistent with the increased reaction volume, the size of crystals grown in the growth chip was generally larger than that of crystals grown in the screening device. Figure 52 shows large crystals of DNA B/C, MscL, and P450 139-3 grown in a growth device. The time required for crystal growth varied substantially, depending on the crystallization target. Crystals of MscL appeared after two days of incubation in growth device. This incubation time is similar to that observed in the screening device (1 to 2 days). In contrast, crystals of DNA B/C appeared after only 2 days of incubation in the screening device, but required greater than 14 days to appear in the growth device.
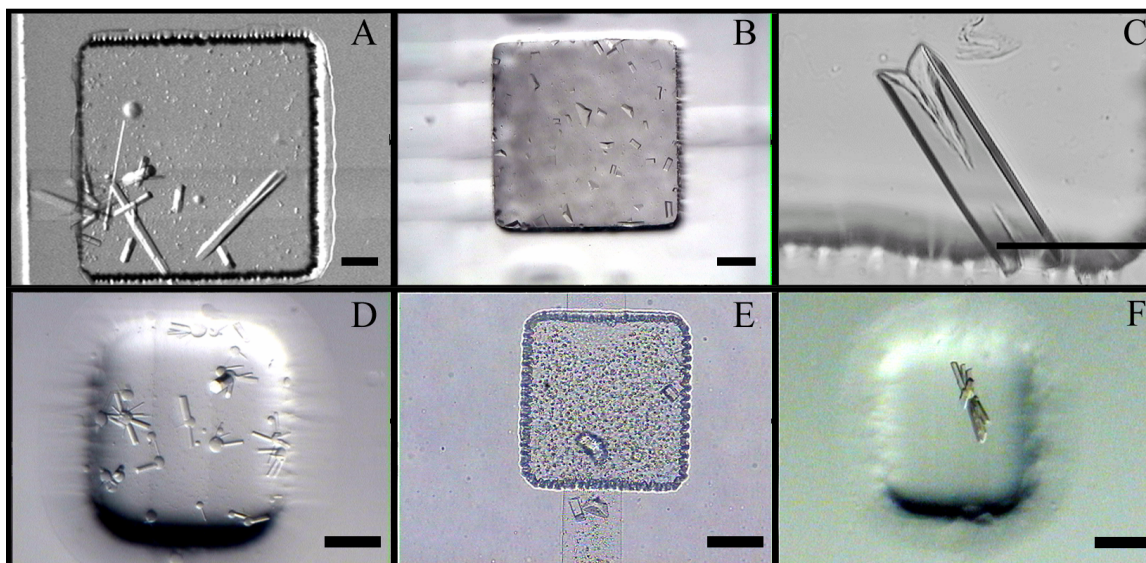
Figure 52: Protein crystallization conditions successfully transported from screening device (≈ 10 nL) to growth device (≈ 300 nL). **(A)** Large crystals of DNA B/C grown in condition identified in screening device **(D)**. **(B)** Crystals of MscL grown in harvesting device using successful condition from screening device **(E)**. **(C)** Large crystal of heme domain of P450 alkane hydroxylase, MUT 139-3. Condition was discovered and optimized in screening device **(F).** All scale bars are 100 μm.

Another interesting observation was that some crystallization targets exhibited a clear dependence of crystal size and morphology on connecting channel length. Crystals of DNA B/C grown by μFID in identical chemical conditions, at the same mixing ratio, but with different connecting channel lengths are shown in Figure 53. This illustrates the importance of varying mixing kinetics as an optimization parameter. In contrast, crystals of MSCL showed similar size and morphology at all connecting channel lengths.
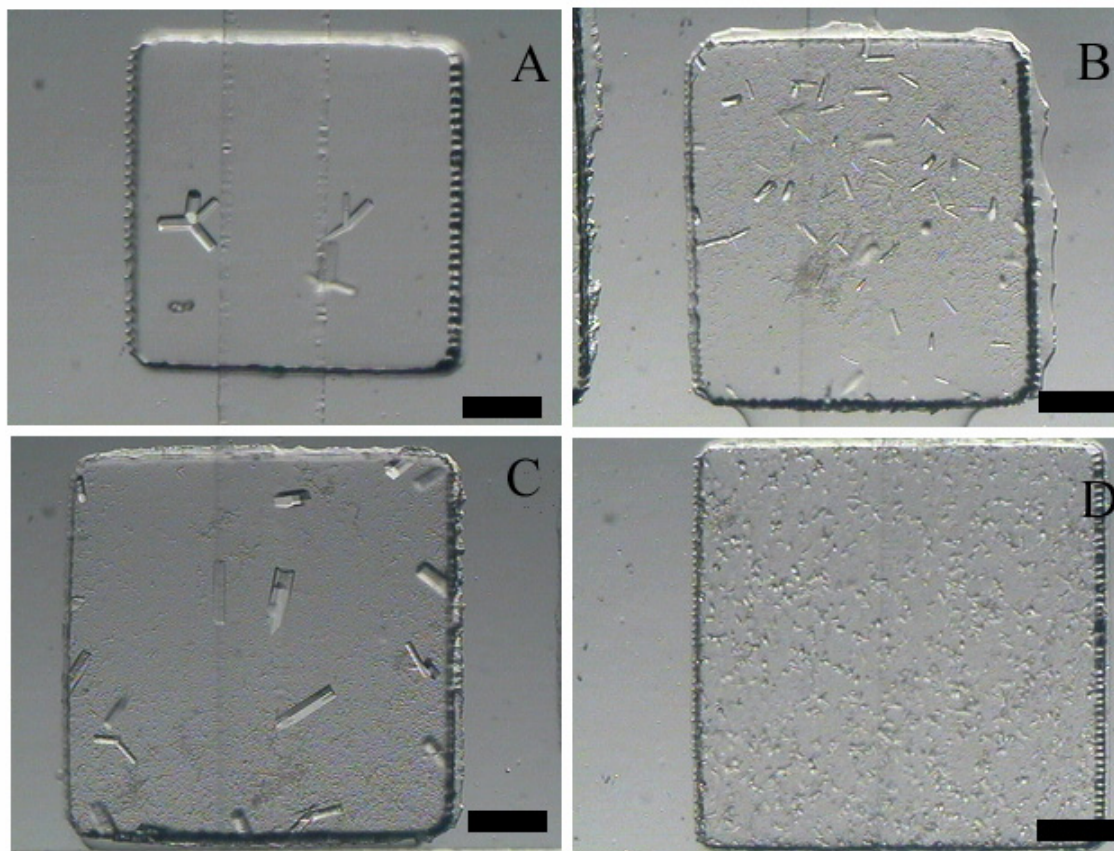
Figure 53: Dependence of crystal size and morphology on connecting channel geometry. **(A)** Crystals of DNA helicase B/C complex. Mixing ratio of 2:1 (protein:precipitant). Precipitant is 2.0 M $(NH_4)_2SO_4$, 0.1 M CAPS pH 10.5, 0.2 M Li_2SO_4. Connecting channel length: 2000 μm. **(B)** Crystals of DNA helicase B/C complex grown in same conditions as (A). Connecting channel length: 250 μm. **(C)** Crystals of DNA helicase B/C complex. Mixing ratio of 4:1 (protein:precipitant). Precipitant is 2.0 M $(NH_4)_2SO_4$. Connecting channel length: 500 μm. **(D)** Crystals of DNA helicase B/C complex grown in same conditions as (C). Connecting channel length: 2000 μm. All scale bars are 100 μm.

Harvesting from the Growth Device

The protocol for extracting crystals from growth chip devices is similar to that used for extraction from screening devices. The device is flipped upside down and a scalpel is used to cut around the periphery of the well containing the crystals creating a "patch" of elastomer that may be removed to expose the well. A drop of cryo-protectant solution into which the crystals will be transferred is dispensed near the edge of the patch. Peeling the patch from the rest of the device draws the cryo-protectant onto the exposed well, covering the crystals. The crystals may then be removed using standard cryo-loops and flash-frozen in liquid nitrogen. Although cumbersome, this general method (with slight variations) has allowed for the extraction of crystals for diffraction studies. In the case of robust model proteins (eg. lysozyme, glucose isomerase, ferritin) high-resolution diffraction data has been collected using growth chip grown crystals. Additionally, crystals extracted from growth chips have been used to collect high-resolution data from drug target proteins with previously unknown structures (personal communication with Fluidigm).

Attempts to harvest more fragile crystals from growth devices have produced varied results, exhibiting diffracting power equal or inferior to crystals grown and harvested by conventional techniques. Chip-grown crystals of DNA D/G/H diffracted to 5.5 Å resolution. This result is comparable to crystals grown and harvested from hanging drop formats, indicating that the low resolution may be attributed to the large unit cell, small size, incorrect cryo-protectant, or poor order of the crystal. In another instance (Rho) crystals showed evidence of damage during harvesting from chip. Crystals of Rho extracted from the growth chip diffracted to approximately 4 Å resolution, while crystals

grown from the same condition in hanging drop format diffracted to 3 Å resolution but displayed increased mosaicity.

Harvesting crystals of DNA B/C from the growth device has been particularly problematic. A large number of crystals of DNA B/C (approximately 50) harvested from growth chips showed very poor diffraction, varying between 25 Å and 8 Å. By comparison a very small (~1000 μm^3) single crystal of DNA B/C (that could not be reproduced), grown after approximately 3 months of incubation in hanging drop format, diffracted to 3 Å and exhibited the same space group as chip-grown crystals; suggesting that the poor diffraction of chip-grown DNA B/C crystals is due to damage during harvesting.

Diffraction Device: Membrane-Mediated Vapor Diffusion

The straightforward scaling up of µFID reactions in the form of a growth device has been successful in producing large diffraction-quality crystals. This strategy has however not proven to be generally applicable in either the transport of successful conditions to larger-volume formats or the harvesting of diffraction-quality crystals. These shortcomings are attributable to dehydration/hydration effects resulting from the permeation of water vapor through the bulk silicone elastomer. To realize a high correspondence method of scaling up crystallization conditions and provide clear path to structure the following criteria must be met.

1. In order to achieve high correspondence with µFID screening reactions, the device must preserve the kinetics of microfluidic mixing while providing larger reaction volumes.

2. In order to achieve high correspondence with µFID screening reactions, the device must provide control over permeability effects and must allow for different rates of hydration/dehydration to be screened.

3. To avoid damaging fragile crystals, the device must allow for harvesting and mounting with minimal crystals manipulations.

4. In order to asses the quality of crystals independent of any cryo-protectant addition or freezing process, it is necessary that the device allow for facile room temperature diffraction studies.

5. The device must allow for the controlled addition of cryo-protectant to the crystal wells.

6. The device must allow for the facile screening of a broad range of cryo-protectants in order to quickly asses optimal freezing conditions.

7. The method of crystal harvesting and automation should be amenable to high-throughput automation and therefore must eliminate the need for delicate crystal manipulations (i.e., "looping").

8. To ensure that crystals are harvested at the optimal time the device must allow for the harvesting of crystals from selective wells without disturbing adjacent reactions.

9. To facilitate alignment of crystals within the X-ray beam the mounting format should provide minimal optical aberration.

10. The mounting format must allow for the collection of high-quality diffraction data over a wide range of angles with acceptable background scatter and attenuation.

A diffraction device designed to simultaneously preserve the successful mixing kinetics of the µFID reactors and allow for precise control over dehydration/hydration effects is shown

in Figure 54. The device integrates 20 reaction sites, each containing 5 separate μFID reactors (inset). Each of the 100 reactors is designed to have a total reaction volume of 200 nL, thereby scaling up the volume of the screening device by a factor of 20. All reaction sites are connected in parallel to a single protein inlet and a single precipitant inlet. The connecting channel between the chambers is designed to have lateral dimensions of 150 μm x 18 μm resulting in a cross sectional area that is approximately 3 fold larger than that of connecting channels in the screening device.
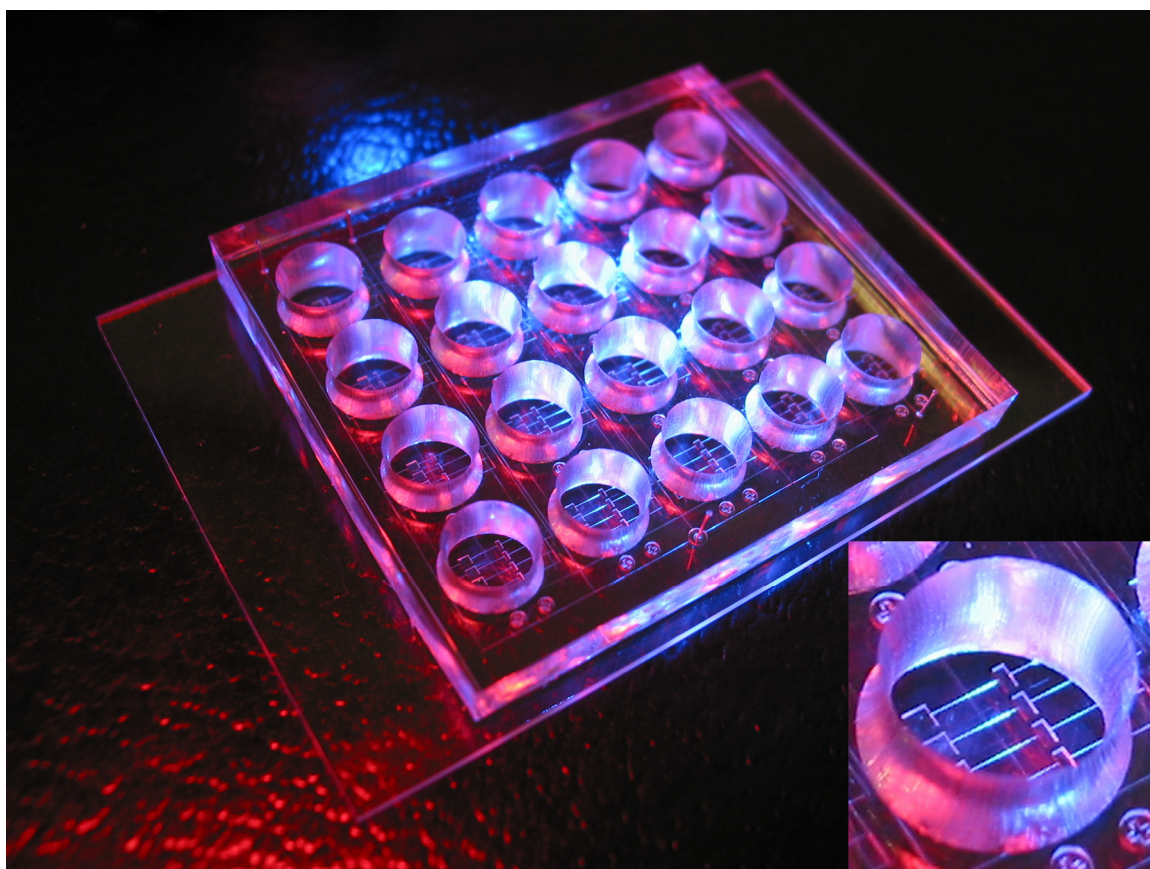
Figure 54: Diffraction chip for scaling up crystallization conditions and harvesting protein crystals. Protein sample and crystallizing agents are mixed at 20 separate reaction sites (inset) featuring 5 µFID reactors.

In order to increase the probability of successfully scaling up conditions, different versions of the device were designed to screen the effect of mixing ratio and channel length. A layout of a diffraction device designed to allow for optimization of both the mixing ratio and mixing rate in the initial transport of crystallization conditions to larger volume formats is shown in Figure 55. Each reaction site has 5 reactors at one of the mixing ratios used in the screening device (4:1, 2:1, 1:1, 1:2, 1:4). Additionally the connecting channel length is varied across the device from 200 µm to 1200 µm. Once the optimal reactor geometry is determined by an initial diffraction chip experiment the condition is repeated on a separate device that reproduces only this geometry over the 100 reactors. This redundancy allows for the production of a large number of crystals from identical conditions to be used in optimizing cryo-protection and freezing protocols.
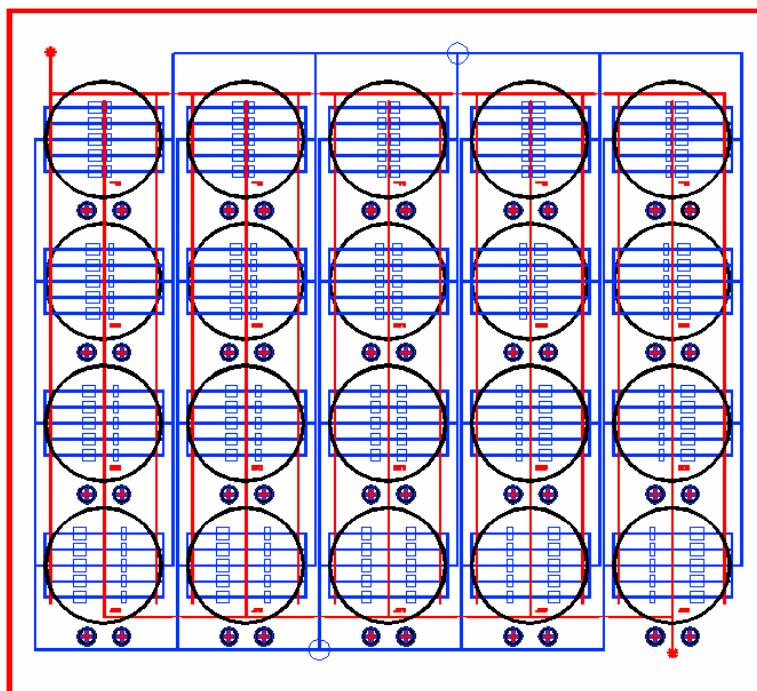
Figure 55: Layout of diffraction device. Two control lines (red) actuate all interface and containment valves in parallel. Flow structure at each reaction site defines a unique combination of mixing ratio and connecting channel geometry (blue). 150 μL reagent reservoirs (black circles) allow for control over rate and extent of dehydration.

In addition to preserving the mixing kinetics of the screening device, the diffraction device further allows for control over the extent and rate of dehydration/hydration. The key distinction between the diffraction device and the growth device is that each of the 20 reaction sites is embedded in a 250 μm thick silicone membrane located at the bottom of separate 150 μL reagent reservoir. A cross section of this membrane showing the enclosed fluidic structure is shown Figure 56.
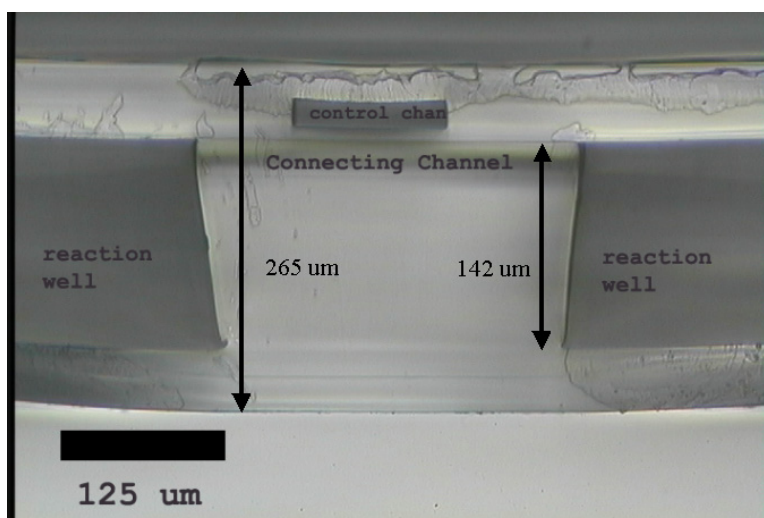
Figure 56: Optical micrograph of cross section of elastomer membrane containing μFID reactors. 142 μm high reaction wells are enclosed at the top and bottom by two 50 μm thick elastomer membranes. The image is inverted so that the membrane containing the constricted connecting channel (in plane), valve membrane, and control channel (cross section) are visible at the top of the structure.

Efficient vapor transport through the thin membrane may be exploited to exercise control over the rate and extent of evaporation. The 150 μL wells overlaying each reaction site are filled with a fluid chosen to control the rate or extent of hydration/dehydration from the reactors. For example an "osmotic bath protocol" may be used in which a solution of known concentration may is added to the reservoir and sealed with clear adhesive tape. During the course of an experiment this solution will equilibrate with the contents of the reactor through membrane-mediated vapor diffusion, and therefore defines an osmotic bath that may be used to precisely control the final extent of dehydration from the reactor (Figure 57). The volume of the osmotic bath is much larger than that of the reactor so the

final state is independent of the contents of the well. In order to ensure the reactor equilibrates to the same osmotic strength as the osmotic bath it is necessary that a low vapor pressure control fluid (eg. fluorinated silicone oil) be used in the control lines. Additionally, since slow dehydration through the elastomer may occur (over several weeks) the osmotic bath solution should be periodically replenished to ensure a well-defined final state.
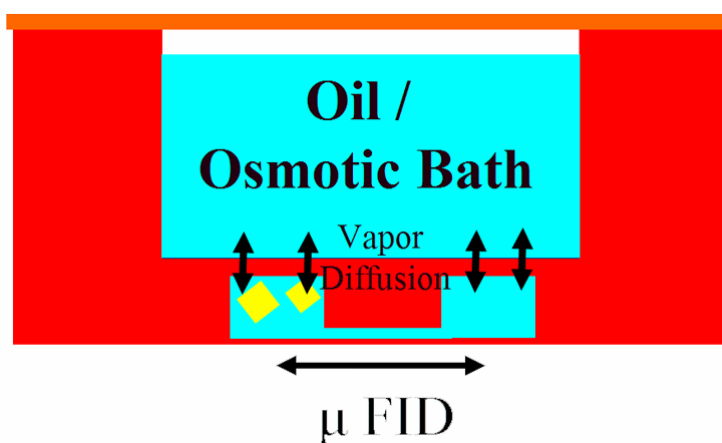
Figure 57: Schematic of diffraction device reaction site illustrating combined equilibration resulting from µFID reaction and membrane-mediated vapor diffusion.

Control over reagent dehydration provides an additional parameter that may be used in crystal optimization. Since the 20 reaction sites of the device may be manipulated independently using different osmotic bath conditions the final level of dehydration/hydration to be screened across the device. This is useful both in scaling up crystallization conditions and in optimizing crystal quality. Figure 58 shows a gallery of lysosyme crystallization trials using identical chemical conditions and different

concentrations of osmotic bath solution. The ease with which the osmotic bath conditions can be exchanged makes it straight forward to manipulate the concentration of crystallization reagents over time. This added level of control may be used to transiently increase the supersaturation for a well-defined time as a means for controlling crystal nucleation. Additionally, once crystals are formed, the osmotic bath may be exchanged for progressively more dilute solutions in order to investigate the solubility of crystals - information which is extremely valuable in crystal optimization, harvesting, and seeding experiments.
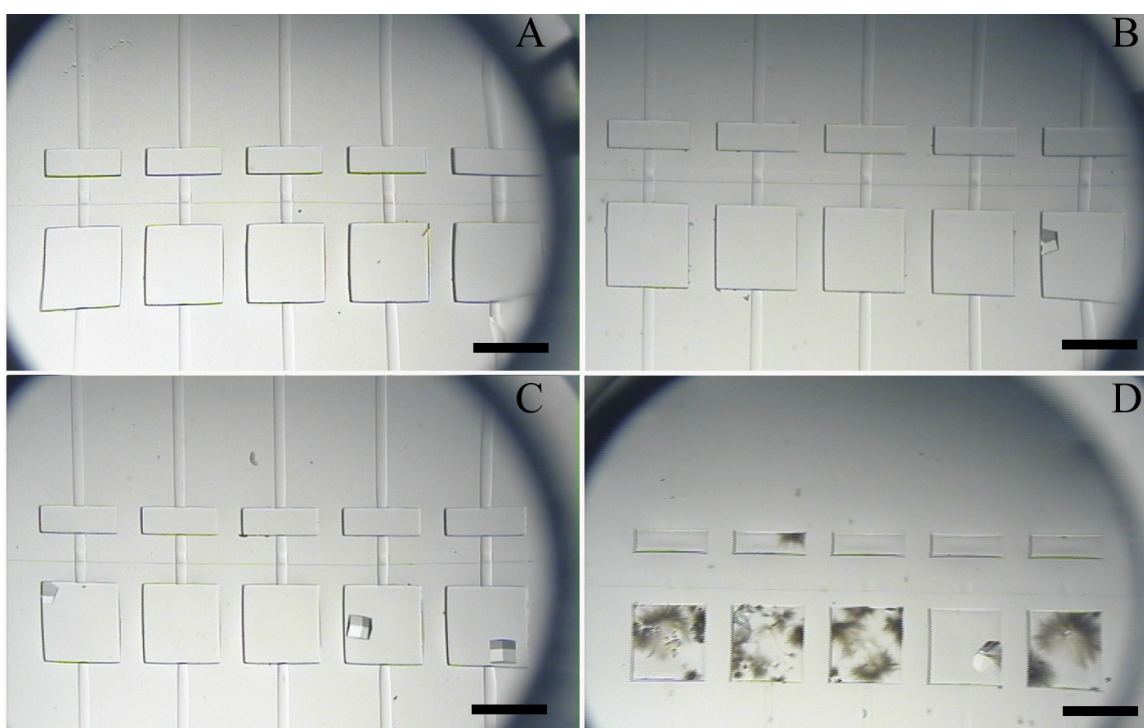
Figure 58: Influence of osmotic bath solution on crystallization of Lysosyme. Mixing ratio 2:1 (protein:precipitant). Precipitant is 2 M NaCl, 0.1 M Sodium Acetate, pH 5.2. Osmotic baths are 0 M NaCl (A), 1.0 M NaCl (B), 2.0 M NaCl (C), and 4.0 M NaCl (D).

Concentrated osmotic bath (D) shows pronounced shrinking of wells and coexistence of tetragonal (second from right) and orthorhombic crystal forms (thin needles). All scale bars are 800 μm.

Membrane-mediated vapor diffusion may also be used to modify the pH or chemistry of the reactors over time. Volatile chemicals added to the reagent reservoir will cross the membrane in vapor phase. This is particularly useful for the addition of volatile cryo-protectants (eg. isopropyl alcohol, ethanol), cross-linking agents (eg. gluteraldehyde, fomaldahyde), or volatile ligands (eg. ethane). Finally, in cases were crystals grow in the presence of a modest concentration of cryo-protectant (eg. glycerol, low molecular weight PEG, MPD, lithium sulfate), the osmotic bath may be used to concentrate these agents sufficiently so that they freeze into an amorphous glass.

Crystallization Using "Osmotic Bath" Protocol

Initial experiments using the "osmotic bath protocol" described above were successful in the crystallization of proteins lysosyme, ferritin, glucose isomerase, and MscL. However, subsequent trials using hdTfR/HFE, DNA B/C and P450 1-12G failed to produce crystals despite extensive exploration of the final reaction state. Experiments with DNA B/C further showed evidence of convective transport between the two wells visible as a plume of protein precipitation. The cause of this convection was determined to be osmotic differences between the sample and the reagent well during the initial stages of equilibration. The time constant for equilibration between the osmotic bath and a reaction chamber may be approximated as

$$\tau \approx \frac{wV\rho_{liq}}{\Delta P_{vap} K_P A \rho_{gas}}, \qquad\qquad \textbf{(21)}$$

where w is the membrane thickness, V is the reactor volume, ρ_{liq} is the mass density of water, ΔP_{vap} is the difference in vapor pressure between osmotic bath and the reagents, K_P is the permeability of the silicone rubber, A is the area of the membrane, and , ρ_{gas} is the mass density of the water vapor. Assuming an initial concentration difference of one molar ($\Delta P_{vap} \approx 3.5$ cmHg), a permeability to water vapor similar to that for CO_2 ($K_P \approx 5*10^{-7}$ $cm^3 \cdot cm/cm^2 \cdot s \cdot cmHg$) (30), a ratio of densities $\rho_{liq}/\rho_{gas} \approx 1000$, and given the reactor and membrane geometries used in the diffraction chip, this time constant is approximately 12 hours. In comparison the time constant for diffusive equilibration of a salt (D $\approx$ 1000 $\mu m^2/s$) between two chambers of 100 nL volume connected by a 500 μm long connecting channel of 2250 μm^2 cross section is on the order of 5 hours. These two timescales are comparable resulting in an osmotic pumping effect between the coupled wells which destroys the desired diffusive mixing. In order to preserve diffusive mixing between the wells the use of the "osmotic bath" protocol was abandoned during the initial diffusive equilibration phase. The use of an osmotic bath in manipulating the final amount of dehydration after initial diffusive mixing is however complete is very useful in establishing a reaction of well-defined chemistry.

Crystallization Using "Permeation Barrier" Protocol

An alternative "permeation barrier" protocol was devised in which permeable oil (FMS oil) is introduced into the reagent reservoirs overlaying the reaction chambers. Since the oil is

immiscible in water it does not induce an osmotic pumping effect between the wells so that the desired equilibration by diffusion is preserved. The oil creates a barrier to vapor permeation and therefore allows for the rate of dehydration to be modulated. By varying the level/amount of oil in each chamber the rate of dehydration may be controlled and screened across the device, mimicking the permeability effects that are realized in the screening device. The effectiveness of this protocol was evaluated in crystallization trials using the 6 of the 7 protein models that had previously been tested using the growth chip (P450 139-3 was not tested). All 6 of the model proteins were successfully crystallize on the first attempt, thereby showing this protocol to be a high correspondence method of scaling up crystallization conditions identified in the screening device. Figure 59 shows crystals of Rho grown using this protocol.

Figure 59: Crystals of Rho grown in diffraction device. 1:1 mixing ratio of protein sample (Rho 10 mg/mL, excess RNA (CU)$_4$, 75 mM NaCl, 10 mM TRIS·HCl pH 7.5) to precipitant (5% w/v PEG 8000, 40% v/v glycerol, 75 mM NaCl). Scale bar is 300 μm.

Diffraction Device: *In Silicone* Diffraction Studies

Complementary to novel technologies for high-throughput screening and crystal growth is the need to develop general methods for quickly harvesting and mounting protein crystals. Traditional techniques for manually mounting crystals by "looping" the crystal out of a drop of mother liquor require significant skill on the part of the technician and are not amenable to automation. Furthermore, since the vast majority of diffraction studies are performed at cryogenic temperatures, harvesting requires the selection and addition of cryoprotectant. The choice of cryoprotectant, the concentration of cryoprotectant, and the rate of cryoprotectant addition are parameters that must be optimized to achieve the maximal diffracting power of the crystal: poorly optimized freezing conditions can result in greatly reduced crystal diffraction.

In cases where diffraction is poor it can be difficult to ascertain whether the crystal was inherently disordered or damaged during the mounting and freezing process. Room-temperature diffraction studies can be used as a diagnostic to evaluate the inherent order of a crystal form prior to screening freezing parameters. In practice room temperature mounts in capillaries are difficult to implement, can mechanically damage crystals, and are rarely used for all but a last resort. Easy methods for performing *in situ* diffraction studies of crystals that do not require mechanical manipulations or the exchange of mother liquor are

therefore of great value in evaluating the quality of crystals. The extension of these methods to allow the automated harvesting of crystals, facile cryoprotectant screening, and low background diffraction studies at cryogenic temperatures will relieve a major obstacle in the structure determination process.

Beyond allowing for control over dehydration during crystallization, the thin membranes of the diffraction device allow for direct *in silicone* diffraction studies. Once a specific reaction site is selected for harvesting, a thin membrane disk containing the crystals may be extracted from the device. A punch tool is inserted through the open face of the reagent reservoirs and used to cut around the periphery of the membrane, creating a "crystal disk". Since the reagent reservoirs are located near the center of the membrane there is no risk of damaging the crystals during this process. The punch tool is designed to fit the orifice of the reagent reservoir so that it is inherently self-aligning. Crystals may be extracted without the need for delicate manipulations under magnifying optics so that the extraction procedure is readily amenable to automation. Furthemore, many crystals within a disk may be harvested simultaneously in a single procedure, thereby greatly increasing the throughput of extraction.

After the crystal disk is cut from the surrounding elastomer it is lifted from the reagent reservoir and mounted using a standard magnetic cap fitted with a small alligator clip (Figure 60A). Once the crystal disk is positioned in the x-ray beam the crystals may be easily visualized through the thin transparent membrane. The crystals may then be interrogated one by one to asses their quality and to generate statistics on the quality of

crystals grown in a given condition. A large savings in time is achieved by eliminating the need for the separate mounting of each crystal screened. Alpha-numeric indices on each well allow for easy cataloguing of conditions.
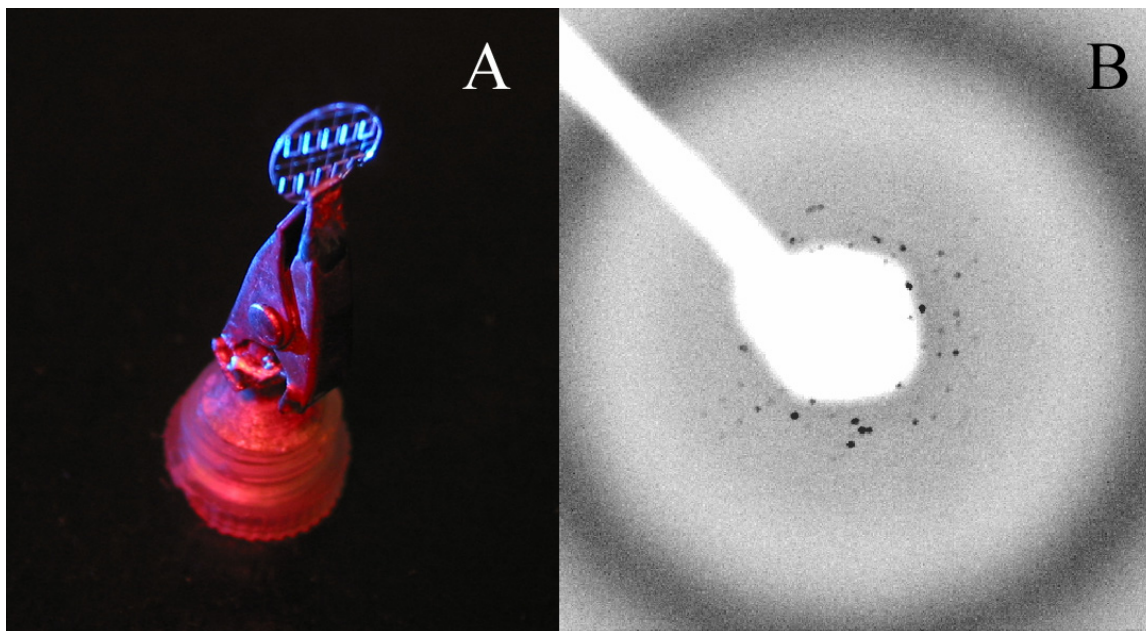
Figure 60: (A) 250 μm thick crystal disk mounted on a cryo-cap fitted with a micro-alligator clip. Diameter of disk is ¼ inch. **(B)** Diffraction pattern from a single MscL crystal showing highest-order reflections at approximately 11.5 Å. Crystals were grown at 4 °C by μFID at a 1:1 mixing ratio with precipitant (40 % v.v PEG MME 750, 100 mM nickel chloride, 100 mM imidazole pH 8.0). Image taken at 4 °C with 20 minute exposure on R-AXIS II home source with 1° oscillation. Characteristic ring diffraction pattern of the silicone elastomer is visible at approximately 7 Å.

This technique was used to evaluate the intrinsic order of crystals of MscL grown in diffraction devices. Approximately 10 crystals were subject to diffraction studies at room temperature on a Rigaku R-AXIS II home source. Exposure times of 10 to 30 minutes were taken with 1 ° oscillation at an angle normal to the face of the crystal disks. Of the 10 crystals studied the highest-order reflections were observed at 9 Å resolution. Representative diffraction data from a crystal of MscL collected *in silicone* at room temperature is shown in Figure 60B. The low resolution data collected from these crystals suggests that the crystals are inherently disordered.

The flash freezing of crystals to cryogenic temperatures (typically -195 °C) is used to reduce x-ray radiation damage and hence increase the amount of data that can be collected from a single crystal. The correct choice and controlled addition of cryo-protectant is a crucial step in achieving the full diffraction potential of a crystal. The diffraction device allows for both the parallel screening of different cryo-protectants, and the controlled addition of these agents by free interface diffusion. To introduce cryo-protectant to a µFID reactor the osmotic bath solution is first replaced with a solution containing the desired cryo-protectant. The membrane covering the well opposite to the well containing crystals is then perforated using a micro-knife bringing it into fluidic contact with reservoir solution. This allows for the cryo-protectant to slowly diffuse into the crystal well over time. For the current well volume and channel geometry the required time for cryo-protectant addition is approximately 24 hours. The parallel screening of 20 different cryo-protectants is accomplished on a single device having identical reaction sites. Once the equilibration of cryo-protectant is complete the crystal disks are extracted as described

above and flash frozen by immersion in a cryogen (liquid nitrogen). As an alternative to introduction directly from the reagent reservoir the cryo-protectant could be introduced to the µFID reactors using a separate microfluidic inlet. This arrangement would further allow for addition of other solutions such as ligands, heavy metals, or fresh protein stock.

Cryogenic *in silicone* diffraction studies were performed on crystals of 3 crystallization standards (lysozyme, glucose isomerase, ferritin), and MscL using a variety of cryoprotectants. 6 crystal disks containing crystals of MscL grown from the same precipitant (40 % v.v PEG MME 750, 100 mM nickel chloride, 100 mM imidazole pH 8.0) were harvested from a single device. These disks were frozen in a variety of cryo-protectants (15% PEG 300, 35% PEG 300, 25% propane diol, 20% PEG 300, 28% xylatol, 20 % glycerol). A single oscillation frame was taken of approximately 40 crystals from these disks. All crystals showed comparable diffracting power with the average resolution of typically less than 10 Å. The highest-order reflections observed were at approximately 9 Å. This result is consistent with diffraction studies conducted at room temperature and supports the hypothesis that these crystals are intrinsically poorly ordered.

In contrast, diffraction studies using the three crystallization standards showed very high-resolution diffraction. Three-dimensional glucose isomerase crystals having a characteristic dimension of 100 µm diffracted to 1.4 Å resolution and exhibited low mosaicity (0.3). Similarily, ferritin crystals diffracted to 1.6 Å resolution with mosaicity of 0.2. Crystals of lysozyme shot through the crystal disk diffracted to 1.2 Å resolution. This resolution is very high, particularly in light of the fact that a five-month-old stock of

lysozyme was used with no optimization of crystallization or harvesting conditions. By comparison, of the 884 structures of lysozyme deposited in the protein data bank all but 10 are of lower resolution.

Three diffraction patterns from a crystal disk containing a 150 μm x 100 μm x 100 μm lysozyme crystal taken at -195 °C is shown in

Figure 61. The patterns are taken at 0°, 45°, and 90° from normal to the plane of the disk. Rotation of the crystal disk changes the thickness of elastomer through which incident and diffracted x-rays must travel, changing both the attenuation of reflections and the amount of background scatter. The signal to noise of reflections is still high at a disk angle of 45° to normal so that data may be collected over a 90° angle. At 90° to normal the incident and diffracted x-rays must pass through a large amount of elastomer, resulting in the elimination of all but the strongest reflections and a large and asymmetric background scatter.
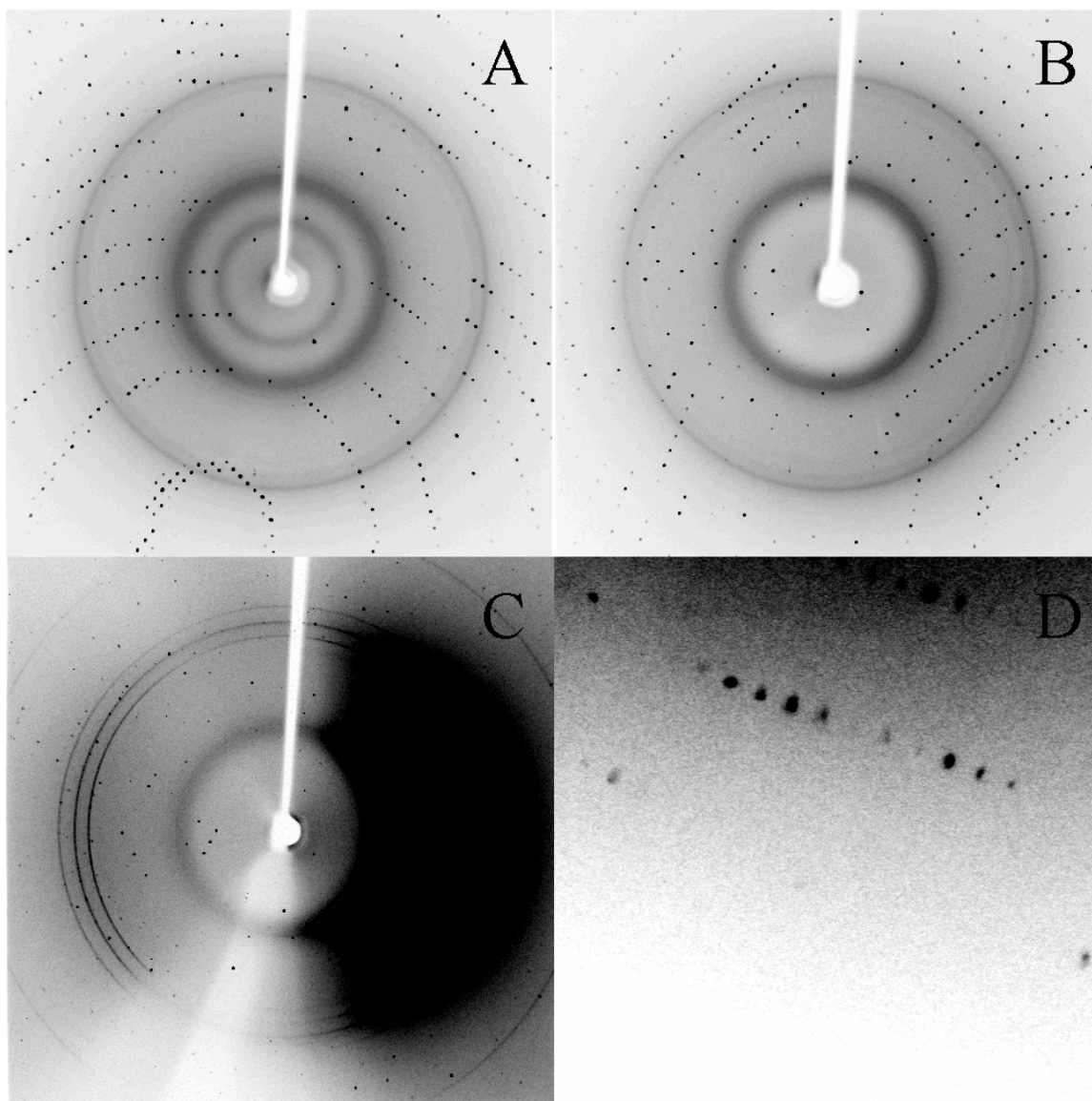
Figure 61: In silicone diffraction studies of lysozyme. **(A)** Diffraction pattern take at 0° from normal to plane of disk: 20 minute exposure with 1° oscillation, detector distance of 250 mm. **(B)** Diffraction pattern take at 45° from normal to plane of disk: 20 minute exposure with 1° oscillation, detector distance of 250 mm. **(C)** Diffraction pattern take at 90° from normal to plane of disk: 20 minute exposure with 1° oscillation, detector

distance of 250 mm. **(D)** Clean reflections at 1.6 Å resolution: 30 minute exposure with 1° oscillation, detector distance of 100 mm. All data taken on R-AXIS IV home source.

Chapter 9

PRACTICAL CONSIDERATIONS: FABRICATION AND OPERATION

Introduction

Since the first reports of microfluidics for use in analytical chemistry and the biological sciences, major efforts have focused on achieving highly integrated lab-on-chip devices. Despite the compelling promise of chip-based fluid-handling and measurement systems, technical obstacles have until recently made this goal largely unrealized. The fabrication of true sealing microvalves, a long-standing problem in the field, was addressed by Unger *et al*. in the development of Multilayer Soft Lithography. This elegant work represented a major breakthrough in microfluidics, allowing for the robust and inexpensive integration of valves in a monolithic silicone elastomer device.

Realizing the potential of MSL in achieving dense integration and high levels of functionality required that technical problems related to fabrication and device operation to be overcome. One major advance, the development of a technique for filling elastomeric microfluidic devices called Pressurized Outgas Priming (POP), is described in Chapter 2. This technique is the basis for a robust geometric metering scheme, allows for the suppression of bubble formation, and enables the practical realization of complex large-scale fluidic networks. The first section in this Chapter introduces the technique of multilayer soft lithography (MSL). The remaining sections outline the author's contribution to the development and refinement of techniques for device priming, substrate bonding, and layer-layer alignment. Additionally, other fabrication issues and techniques

for creating multilevel flow structures, and alternate valve geometries are discussed. It is the author's intention that this Chapter will provide a useful introduction to several important considerations for researchers who are interested in MSL technology.

Multilayer Soft Lithography: Background

Multilayer Soft Lithography (MSL), which is an extension of Soft Lithography (26, 92), enables the facile and inexpensive large-scale integration of valves on chip (13, 27). MSL describes a process by which consecutive micro-molding and layer bonding steps are used to generate complex multilayer fluidic devices with active mechanical valves, pumps, mixers, and flow control logic. Both replica molding from microfabricated masters and the use of elastomer membranes for actuation of microfluidic valves predates the multilayer soft lithography. MSL technology seamlessly integrates these ideas in an elegant and simple fabrication process. The enormous success of this technique can be largely attributed to a method developed by Unger *et al.* for covalently bonding successive layers of silicone elastomer.

Due to their excellent optical properties, low surface energy (22 mJ/m^2), and low Young's modulus, silicone rubbers have become the most popular material for multi-layer soft lithography. Silicone rubbers are typically formed from the combination of two liquid components that cross-link into a flexible solid upon curing. One such example polymer is General Electric RTV 615. Part A of this compound consists polydimethylsiloxane polymers that have been functionalized with vinyl groups. Part B contains silicon hydride (Si-H) groups that covalently bond to the vinyl groups of part A, cross-linking the

polymers. In the presence of a platinum catalyst the silicon hydride groups become covalently bonded through a direct addition reaction to the vinyl groups, thereby solidifying the mixture through a cross-linking process (Figure 62). The low curing shrinkage and absence of gaseous byproducts makes this system ideal for the high-fidelity reproduction of microfabricated features.

When mixed at the stoichiometric ratio of 10:1 (A:B) there is an equal number of vinyl and silicon hydride groups, so that all reactive groups are incorporated into a covalent bond. However, when combined at a different ratio, there remain active groups that do not participate in a covalent bond, and which instead may be used to permanently bond two surfaces together, creating a monolithic device (Figure 62).
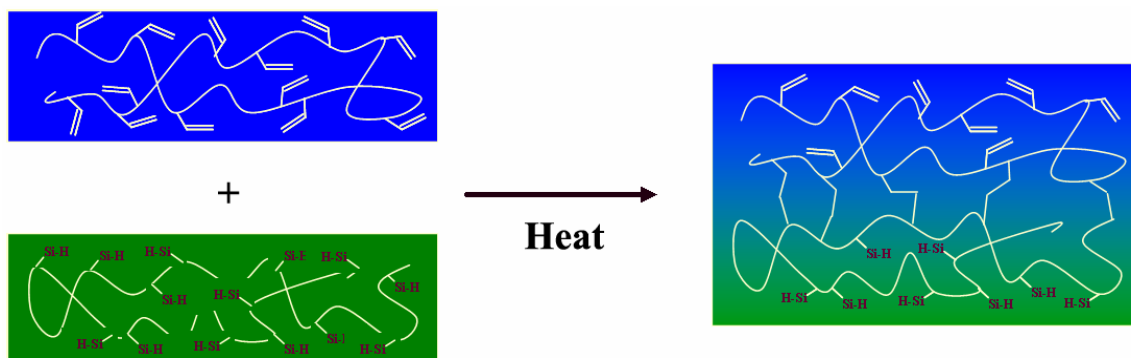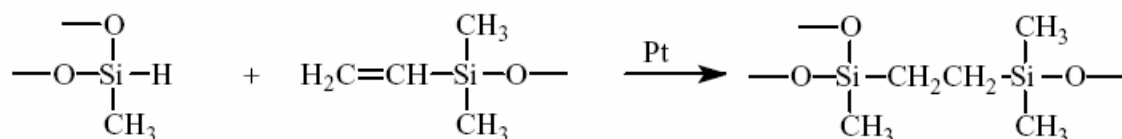
Figure 62: MSL bonding process. Cross-linking of polymer through direct addition reaction of silicon hydride and vinyl groups (top). Off-ratio mixing of silicone results in excess reactive surface groups for covalent layer-layer bonding.

A process flow diagram illustrating the steps in MSL is shown in Figure 63. Two negative molds, one defining the flow structure, and the other defining the control structure of valves, are first patterned on a silicon wafer using conventional photolithography, leaving 10 μm raised features of photo-resist. The flow layer master is then annealed so that the photo-resist is allowed to re-flow, creating rounded flow channels. Masters are reproduced by replica molding in silicone rubber. A 30:1 ratio of (A:B) silicone rubber, having excess vinyl groups, is spun onto the flow mold to a final thickness of 30 μm. A 3:1 silicone rubber layer, containing excess silicon hydride groups, is cast over the control mold to a thickness of approximately 7 mm. Once both layers are heated and allowed to partially cure, the structures solidify. The control layer is then peeled from the mold, punched to create valve access ports, and aligned to the flow structure. The entire device is then heated once again, causing the excess vinyl and silicon hydride groups to covalently bond. The resulting monolithic device is peeled from the flow mold, and channel access ports are punched into it prior to sealing the multilayer polymer to a glass substrate. The substrate itself may additionally have structural features, such as microwells that may be accessed through the molded channels, thus providing larger localized volumes for reactions to occur.
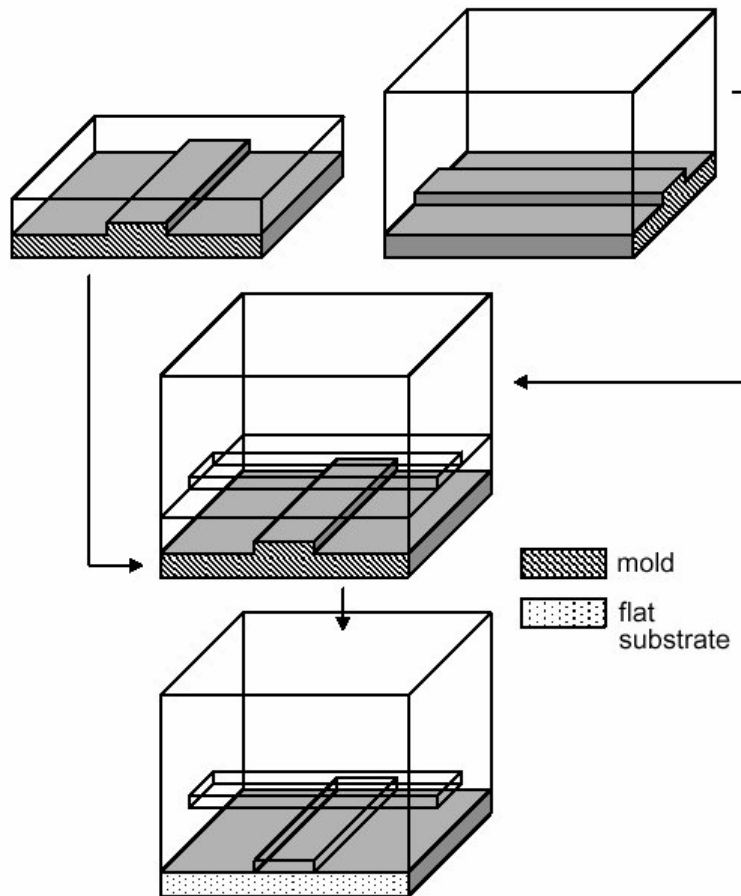
Figure 63: Flow diagram illustration technique of multilayer soft lithography.

When a control channel crosses over a flow channel, only a thin square membrane of elastomer separates the two, forming a valve (Figure 64A). By pneumatic or hydraulic pressurization of the control channel, the membrane may be deflected down into the flow channel, causing it to seal against the glass substrate (Figure 64B). Due to the compliance of the membrane, a hermetic seal may be easily achieved at moderate actuation pressures even in the presence of particulates or imperfections. The low Young's modulus of the elastomer (~1 MPa vrs ~100 GPa for crystalline silicon) allows for closing of valves

having areas as small as 100 μm^2, so that many thousands of active valves may be integrated on a chip smaller then a credit card (27). Just as the transistor is the fundamental component in modern electronic circuitry, higher level fluidic toolbox of components may be built up from combinations of valves.
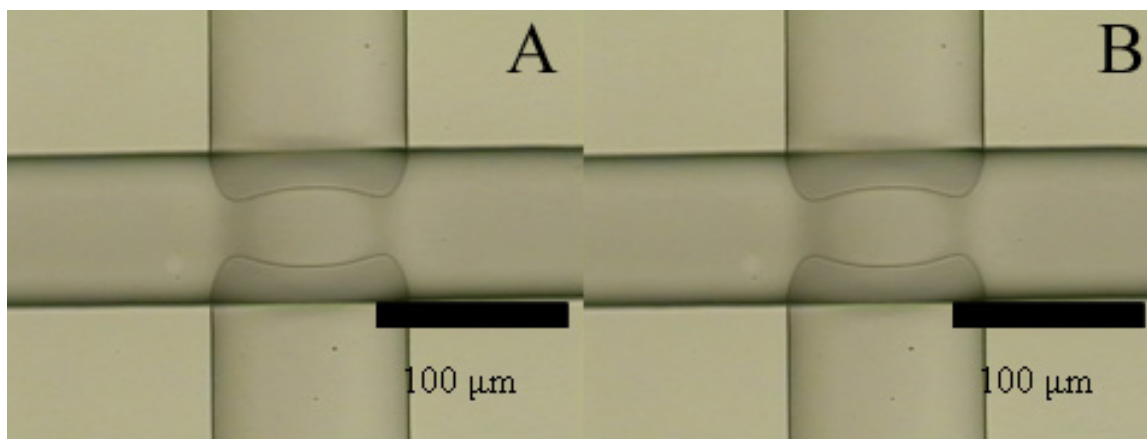
Figure 64: MSL valves. **(A)** Micrograph of an open valve showing control (horizontal) and flow (vertical) structures. **(B)** Closed valve. Application of pressure to control structure deflects membrane and pinches off flow structure, creating a fluidic seal.

Unger *et al.* described the serial combination of three separately addressable valves along a channel to form a peristaltic pump (Figure 65). When operated in the linear regime (below the cutoff frequency) sequential actuation of these valves through a designated peristaltic cycle of states moves a fixed volume of fluid across the pump. This pump allows for the flow direction to be reversed through reversal of the peristaltic sequence. The Navier-Stokes equations, which describe the flow of a Newtonian fluid at low Reynolds number are time-reversible so that reversal of the peristaltic sequence causes an exact time-reversal

of the unsteady flow field due to forward pumping, regardless of symmetry breaking in the flow structure upstream and downstream of the pump. Interestingly, the cycling of two valves is sufficient for producing a directional flow if symmetry is broken through the time sequence (personal communication with Jian Liu). Below the pump cutoff frequency the flow rate is proportional to the peristaltic cycling rate, thereby allowing for programmable control of the mass flux.
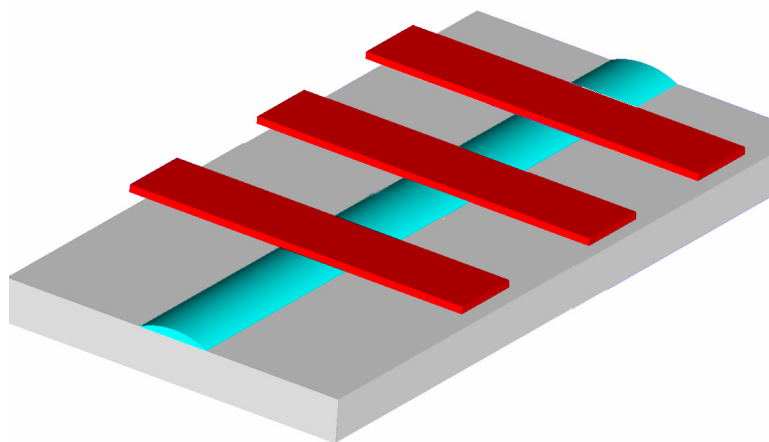
Figure 65: Peristaltic pump.

Chu *et al*. described a rotary mixer which features the integration of a peristaltic pump in a contained circular flow structure to accelerate the mixing of reagents. Batch mixing is achieved through the dispersion of the reagents within the flow structure as they circulate through the ring. Using this method the time required for the mixing of two solutions was reduced from many hours to minutes. Chapter 5 describes the incorporation of this mixing structure as a key element in achieving true combinatorial mixing on chip. An analysis of

the scaling laws that govern the mixing speed, numerical simulations of mixing, and the optimization of this element for ultra-fast mixing are presented in Chapter 6.

The actuation pressure required to close a valve is dependent on the geometry of the valve junction and the material properties of the elastomer. For elastomer membranes fabricated from 20:1 GE RTV bonded to 5:1 GE RTV, and a standard geometry of a 10 μm high flow channel, a 20 μm thick membrane, and a 100 μm x 100 μm valve, the required actuation pressure is approximately 6 psi. The strong dependence of actuation pressure on the channel and valve geometry may be exploited to engineer bridges (valves with very high actuation pressure) by simply tapering the thickness of a control channel in the vicinity of a flow channel that is not to be closed. By applying an intermediate actuation pressure, a single control channel may be used to close a plurality of selected flow channels without significantly impeding flow in adjacent lines.

Chou proposed the use of bridges in realizing a microfluidic multiplexing element. This element uses an array of complementary valve pairs organized in binary-tree architecture to selecting 1 of N flow lines using $2\log_2 N$ control lines (Figure 66). This element enables the realization of increasingly complex fluidic structures with only a modest rise in control complexity. The straightforward implementation of this design was first demonstrated in early protein crystallization designs. More complex multiplexing structures have been instrumental in realizing large-scale fluidic integration (27), and on-chip combinatorial mixing.
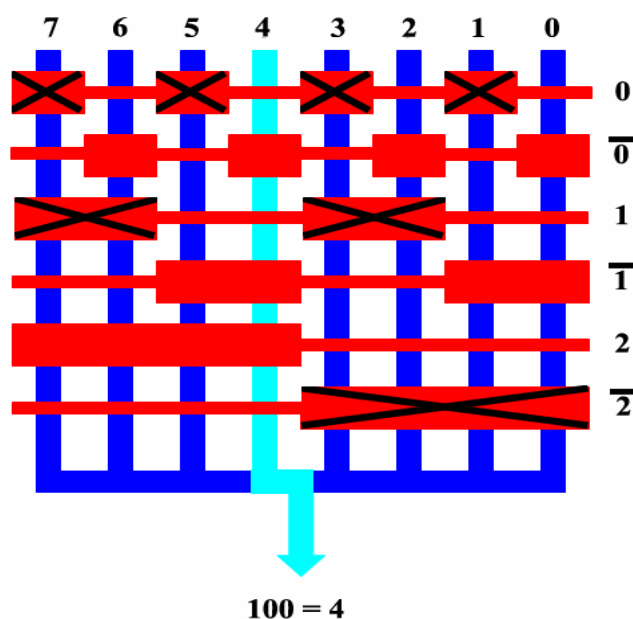
Figure 66: Parallel-channel multiplexing structure. Each pair of complementary valves comprises a bit.

Elastomer Shrinkage

The polymerization of poly(dimethyl-siloxane) does not require the removal of a solvent, and does not produce bi-products. These properties ensure that very little elastomer shrinkage occurs during curing when compared to other elastomer systems (typically with volume shrinkage on the order of 10% - 30%). Nevertheless, even slight intrinsic deformation of a molded structure, when integrated over the full length of a device, can result in unacceptable feature registration errors. Although this problem was tolerated in early MSL devices (cell and DNA sorters), by maintaining small active device areas (approximately 10 mm^2), few valves (less than 10), and large registration tolerances, it placed unacceptable constraints on early screening device designs that necessitated larger

areas (10 cm^2) and higher levels of integration (approximately 200 valves). A linear shrinkage of 1% over the typical length of a device results in misalignment between features that is large (300 μm) compared to the feature dimensions (100 μm).

Initial curing of the elastomer layers prior to bonding results the isotropic shrinkage of the structures. Since both layers are supported by a silicon substrate during curing, this shrinkage is manifested as an expansive strain in the thick layer (7 mm) and thin film (approx 25 μ). Release of the thick layer prior to alignment releaves this strain causing a compression of the molded features. This compression was found to be reproducible and can therefore be compensated for by a complementary expansion of the mold features. A systematic study of a silicone elastomer system (GE 615 RTV) was carried out to determine the degree of shrinkage during polymerization. A microfabricated ruler consisting of an array of lines spaced at 100 μm intervals was fabricated for the measurement of elastomer shrinkage. The elastomer was mixed at a ratio of 5 part A : 1 part B, cast to approximately 7 mm, degassed, and cured at 80 °C for 1.25 hours. The 3 cm molded elastomer part was aligned at one end to the original mold and inspected using an optical microscope. The total shrinkage of the molded part over the 3 cm pattern was determined to be 450 ± 50 microns, corresponding to a linear compression of approximately 1.5 %. The molded part was subsequently cured overnight (approximately 20 hours) and compared to the master once more. The final shrinkage after full curing was determined to be approximately 2.5 %. Correct registration of features over 3 cm with 10 μm alignment tolerances was achieved by the compensatory expansion of appropriate master molds by these factors.

Layer-Layer Registration

As the complexity of devices has increased techniques for the precise alignment of complex molded elastomer parts have been developed in parallel by many members of our lab, most notably by Todd Thorsen, Sebastian Maerkl, Jian Liu, and myself. This discussion is intended to elucidate the process by which micromolded structures can be manually aligned to micron precision over a large active area; a task that will seem unlikely to readers with little experience in this area.

Ignoring leveling considerations, correct alignment of part to a substrate requires the simultaneous control of two translational degrees of freedom and one rotational degree of freedom. Techniques for the alignment of hard planar substrates for wafer bonding applications are well established and can achieve alignment tolerances below 1 μm. In contrast, soft structures present a nontrivial alignment problem due to curing shrinkage, elastic deformation, and unlevel cast parts. This problem is accentuated in the manual alignment of large compliant parts where physical manipulations invariably introduce mechanical deformations which are large compared to the feature sizes. Furthermore, the precision with which an average person can perform manipulations is limited to several tens of microns.

Nevertheless a technique of iterative alignment and mechanical force-motion transduction enables the manual alignment of features over a large working area with micron-scale precision. The part is first aligned to the substrate as precisely as possible, creating a reversible bond. Typically this will result mechanical deformations of the piece (warping),

translational misalignment errors of approximately 100 μm, and rotational errors on the order of a few degrees. One side of the part is then peeled from the substrate and, with the opposite side fixed to the substrate, is realigned by pushing or pulling the piece. During this process the elastomer part acts as a force-motion transducer. The strain imparted to the elastomer is distributed evenly over the length of the unsupported elastomer. This results in a large mechanical reduction so that a 100 μm translation at the end of a 1 cm unsupported section produces a 1 μm translation of features located 100 μm from the fixed point. Slowly advancing the contact front and iterating this process allows for micron scale alignment to be achieved over a large working area. The use of elastic materials for force transduction and mechanical reduction may find applications in other areas where inexpensive micromanipulations are required.

Substrate Adhesion

Glass-elastomer hybrid flow structures eliminate the need for an additional elastomer bonding step and allow for the incorporation substrate features such as electrodes or microwells. Additionally, hybrid structures may exploit the plethora of well-characterized surface modifications and functionalization protocols for glass. Crucial to the operation of these devices is the ability to create a strong silicone-glass bond. Early hybrid devices relied exclusively on Vanderwhaals interactions between the glass and the elastomer for device sealing. This resulted in a weak bond that could not withstand fluid pressures in excess of approximately 3 psi, and that was easily compromised by mechanical strain during the insertion of fluidic input/ouput connectors. The limited operation pressure of these devices necessitated the use of surface modification protocols to increase

hydrophillicity and facilitate filling (98). Using this bonding protocol it was found that delamination was the overwhelming device failure mode, ultimately resulting in the failure of approximately 50% of tested devices.

A method for achieving high-strength silicone-glass bonds by oxygen plasma treatment of silicone has been previously described (99). It is thought that oxygen plasma treatment produces reactive groups on the suface that can then covalently bond to the glass substrate. Contact angle measurements of oxygen plasma treated silicone give clear evidence of a chemical modification that makes the elastomer more hydrophilic. Efforts to reproduce this work in our lab using GE 615 RTV elastomer have resulted in inconsistent and incomplete bonding over large surface areas. Although inconsistent with the proposed bonding mechanism, bonding appears to be dependent upon the material system (personal communication R. Ismagilov); reported results use Silgard silicone rubbers. Results with Silgard are apparently also inconsistent with variations attributed to contaminants introduced in the plasma chamber (personal communication R. Ismagilov). Another practical consideration that makes this technique less attractive is that the surface modification is temporary so that bonding must be done shortly after plasma treatment. This requirement places impractical time constraints on device alignment and assembly. Finally, the bonding is instantaneous so that "one-touch" alignment of devices to substrate features is required.

In order to resolve this fundamental problem a new bonding protocol was developed for reversible and robust bonding of Silgard and GE silicone rubber to glass substrates. To

achieve a strong reversible bond the device and substrate are rinsed with ethanol, dried under a stream of nitrogen, and aligned to one another. The assembled device is then baked overnight at 80 °C. It was found that this procedure reliably produced seals that could withstand greater than 10 psi flow pressures with some seals holding in excess of 30 psi. The bonding procedure was shown to work with both Silgard and GE silicones, and was compatible with borosilicate crown, soda lime and quartz substrates. Robust bonding with epoxy and BSA functionalized slides has also been achieved (personal communication with S. Maerkl). The mechanism for this bonding is unclear and has not been thoroughly investigated. It is however probable that the ethanol does not participate directly in the glass-silicone bonding interaction and that other organic solvents would be equally effective. Limited investigation has showed that ethanol was necessary for bonding, and that bond strength increased with bake time. Furthermore, fully cured elastomers appear to bond as well as partially cured elastomers. Since this technique has been instrumental in improving device yield, and has been universally accepted in our lab as a standard protocol, the mechanism of bonding warrants further investigation.

Robust Multilayer Bonding

Multiple elastomer bonding steps are required for the fabrication of MSL devices that do not use hybrid glass-elastomer channels, use push-up valve geometries, or that incorporate two control layers (see below). The original protocol for bonding successive elastomer layers utilizes alternating mixing ratio compositions of 3:1 and 30:1 (13). This protocol works well for the bonding of thick layers but produces weak bonds for the thin layers that are used to create channel and valve structures. This poor bonding can be attributed to the

diffusion of reactive species through the polymer during curing steps (in personal communication with Mark Unger). FTIR studies of cross sections of bonded silicone elastomer suggest that as a thick elastomer layer containing excess vinyl groups is bonded to a thin silicon hydride-rich layer the short silicon hydride chains can diffuse up into the bulk material (personal communication K. Self). The final material properties of the thin film are therefore dominated by the thicker elastomer layer, resulting in a chemical composition on the bottom surface that resembles 5:1 silicone. A strong second bond can be formed between a thin film of 20:1 elastomer and a thin film of 20:1 elastomer previously bonded to a thick 5:1 layer. Although this protocol works well for the successive bonding of two thin layers, it fails if the thickness of the first bonded film is large (greater than 50 μm). This failure is likely due to incomplete diffusion of the silicon hydride groups from the bottom surface of the first layer.

Bubble Formation

Early MSL devices relied exclusively on pneumatic actuation for implementing valve control. This actuation scheme created problems due to bubble formation resulting from permeation of gas across the elastomer membrane. This mechanism is particularly problematic in applications where valves must be operated at high pressures, or actuated for prolonged periods of time. In principal, since the control lines must necessarily be maintained at a pressure higher than the working fluid bubble formation can appear instantaneously. In practice surface tension at the channel wall suppressed this process until a nucleation event occurs. The onset of this nucleation can be postponed by initially priming the device at high pressure (to ensure no nucleation sites remain). Once a

nucleation event occurs the bubble continues to grow, filling the entirety of the channel or breaking off into a string of satellite bubbles. This phenomena severely limits reliability and performance in pneumatically actuated devices.

As an alternative to pneumatics, hydraulic actuation may be used to completely eliminate the problem of bubble formation. The POP technique allows for control structures to be "dead-end" filled with a hydraulic fluid without any modification of control channel design. Due to the high gas permeability of silicone and the generally large surface to volume ratios of control structures, complete filling of control lines can be achieved in less than a minute at modest filling pressures (10 psi). The choice of hydraulic fluid will be application specific, and will be governed by the fluid properties. The use of dionized water as a control fluid has become standard in applications involving aqueous chemistry.

Controlling Reagent Dehydration

The use of water as hydraulic fluid has the added advantage of reducing reagent dehydration issues. The high permeability of silicone rubber to water vapor implies that reagents are constantly subject to dehydration through the bulk material. This effect is pronounced in applications that require long incubation times and can result in complete drying of the flow structure. The rate of dehydration depends on the relative vapor pressure of the reagent solution, and hence on it's composition, and on the partial vapor pressure in the surrounding polymer matrix. The presence of a water-filled control structure in close proximity to the reagent line mediates this effect by elevating the partial pressure of water vapor near the channels. At short times this acts to dramatically reduce the rate of

dehydration. This effect has been exploited to reduce dehydration in numerous applications including cell-screening arrays (27), PCR devices (32), and protein crystallization (29). At long times a state of dynamic equilibrium is achieved in which the rates of vapor transport to and from the reagents are equal. This equilibrium depends on a number of factors including the osmotic strength of the reagents, the proximity and density of the control structure, and the ambient temperature and humidity. The complicated interplay of these effects makes the long time dehydration of reagents a difficult parameter to control. This issue is further discussed in Chapter 8 along with methods for controlling dehydration.

In some applications it may be advantageous to use alternative control fluids. In such cases material compatibility issues must be considered. Many common organic solvents such as toluene, isopropyl alcohol, and acetone will quickly swell the elastomer, constricting control channels. Other volatile organic solvents such as alcohol will quickly diffuse in gas phase through the bulk material and contaminate reagents. This may be used to advantage as a means of slowly introducing chemical species into a reaction; for example in inducing cells with ethanol. Oils may be used as control fluids if no transport of vapor from the control lines is desired. Many oils, including paraffin oil and poly(dimethyl-siloxane) are incompatible with silicone rubber and will quickly swell channels. Highly fluorinated silicone oils (Fluoroguard[TM] Dupont, FMS oil Hampton Research) are however compatible with silicone rubber and can be used for prolonged periods without detrimental effects. Many of these compounds have very high viscosity (approximately 1000 cP), and are therefore not suitable for applications requiring fast control response.

Push-up Valves

In the original valve configuration described by Unger *et al.* the control structure is bonded on top of a membrane that is deflected down into a hybrid silicon-glass flow channel structure. In this push-down geometry the membrane is not of constant thickness since the flow channel has a rounded cross section. The difference in valve membrane thickness between the center and the edge of the flow channel is equal to the channel height. The added thickness increases the flexural rigidity of the valve. This increased stiffness results in a faster valve recovery time but limits the maximum channel height that can be closed at achievable actuation pressures.

The lack of a robust technique for fabricating inter-layer vias implies that all valves must connected to a planar continuous control structure terminating at a control input port. In some applications this constraint creates routing problems that are fundamentally unavoidable (topologically entangled). One example of this is the design of a microfluidic matrix form combinatorial polymerase chain reactions in which every flow junction must be controlled by three separately addressable valves. The integration of valve structures both on the top and the bottom of a flow structure allows for crossing control lines, thereby obviating the routing constraints imposed by planar structures.

To this end, an alternative valve-geometry was investigated in which a membrane of constant cross section is deflected up into the flow structure. This push-up geometry is more optimal in that a membrane is deflected into a curved shape that matches that of the

top of the flow structure. Push up valves 50, 100, and 200 μm thickness where fabricated and tested in the closing of a 10 μm high and 100 μm thick flow channel. The membrane thickness was designed to be approximately 30 μm. It was confirmed that these valves closed at lower actuation pressures than push-down valves of equal lateral dimensions and similar minimum membrane thickness. This solution to the routing problem was ultimately abandoned for a planar solution using designed differential actuation pressures (discussed below). Nevertheless, the push-up geometry has been used for the fabrication of valves in high channel structures (100), alleviating routing problems (F. Balagadde, personal communication) (32), and for the integration of multilevel fluidic flow structures (in review, PNAS). The closure of a 40 μm high flow channel by 200 μm x 200 μm push-up valves is shown in Figure 67.
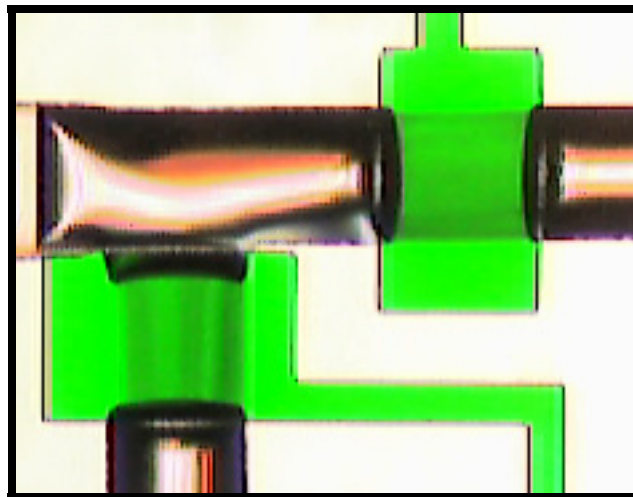
Figure 67: Integrated push-up valves for the closure of tall (40 μm) channel structures. Figure courtesy of J. Marcus. One vertex of the matrix is shown in the inset.

Variable Pressure Valves

If control valves have a consistent logical relationship during operation it may be still be possible to implement planar control structures despite fundamental routing problems due to topological entanglement. In the case of the microfluidic matrix structure shown in Figure 68 operation requires that valve X always be actuated when valve Y is actuated. In this case both valves may be controlled by a single pressure source if the valves are designed to have differential actuation pressure thresholds. The strong dependence of the threshold actuation pressure of a valve on valve width may be exploited to tune valve actuation pressures, thereby allowing for the selective actuation of certain valves at intermediate pressures. Application of 110 KPa psi pressure causes the closure of valve X (width 270 microns) while valve Y (width 96 microns) remains open. At pressures above 260 KPa both valves are closed. This design was used to implement an N by N combinatorial PCR microfluidic matrix that amortizes a single slug of polymerase reagent over N^2 reactions.
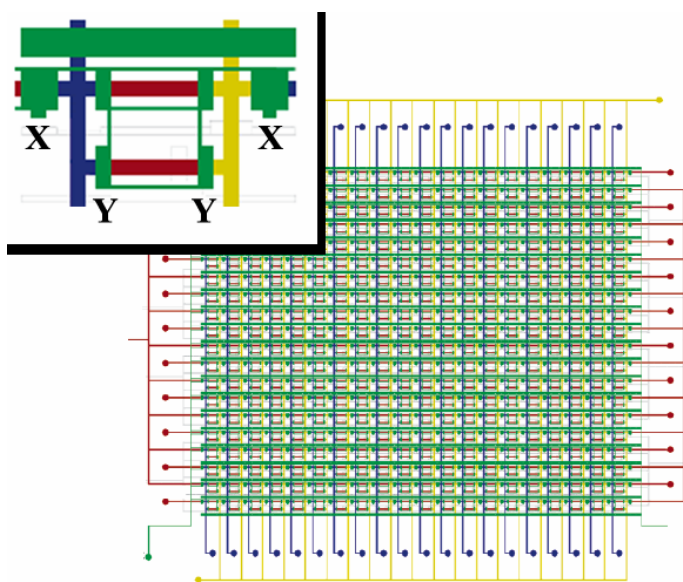
Figure 68: Microfluidic matrix structure using variable pressure valves to eliminate wiring constraints.

Multilevel Molds

The ability to combine channel structures having varying height into a single fluidic network greatly increases design control and flexibility. For instance, tall channels can be used to create a low-impedance fluidic bus, or to increase flow through long i/o connections. Tall reaction wells can be used to increased reaction volumes while minimizing diffusion lengths and surface to volume ratios (see below). Additionally, vertically constricted channel sections can be used as size-specific filters for bead and cell capture or column stacking.

The incorporation of valves into multilevel mold structures imposes additional design constraints that must be adhered to. Regardless of whether a push-up or push-down valve geometry is used, achieving a good seal requires that the flow channel have a rounded cross section. The fabrication of molds having a rounded flow structure is achieved by thermal re-flow of the patterned photo-resist. Negative photo-resists such as SU8 rely on thermal polymerization of UV-exposed regions, and therefore can not be reflowed. In order to be compatible with membrane valves, flow channel sections must therefore be defined using a positive photoresist such as Shipley 5740.

For features that do not require rounded cross sections negative photoresists such as the SU8 series are superior to positive resists in that they are more mechanically robust, allow a

broad range of channel heights (100 nm to 1000 μm), and can achieve very high aspect ratios (up to 50:1).   For these reasons SU8 resists are preferable for the fabrication of control structures molds.   The higher achievable channel heights result in a dramatic decrease in the fluidic impedance of the control structure network, thereby allowing for faster valve response (6).   Furthermore, SU8 resist allow for molding/curing temperatures up to approximately 200 °C compared to approximately 90 °C for 5740. A negative master of a control structure patterned in a 25 μm high SU8 2025 film is shown Figure 69.
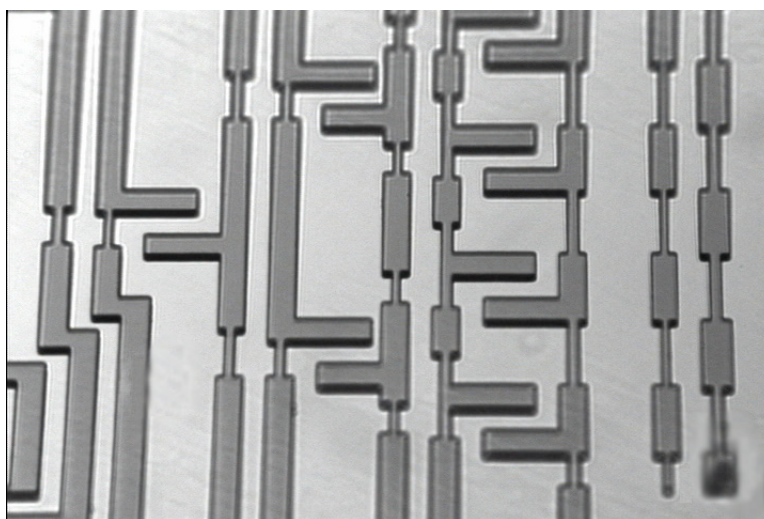
Figure 69: Negative master of 25 μm high control features fabricated in SU8 2025.

Furthermore, in some applications such as the fabrication of removable filters (see below) and observation windows for absorbance and fluorescence measurements, it may be desired to maintain a rectangular channel cross section in specific locations within the flow structure. Multiple lithography steps can be used to create hybrid SU8-5740 molds. If SU8 features are shorter than 5740 features this process is straightforward. Features are first

defined in SU8 by conventional processing. The wafer is then coated with 5740 photoresist and processed in the conventional way. Initial soft-baking of the 5740 planarizes the film so that height perturbations due to spin-coating over the SU8 features are minimized. Since SU8 features as small as 1 μm in height are easily visible through 10 μm of 5740, alignment is easily achieved. Once the 5740 features have been developed they are thermally annealed to generate a rounded profile amenable to the integration of valves. A molded replica of a mixing ring featuring a 10 μm high observation window of rectangular cross section incorporated in a 13 μm high section of channel having rounded cross section is shown in Figure 70.
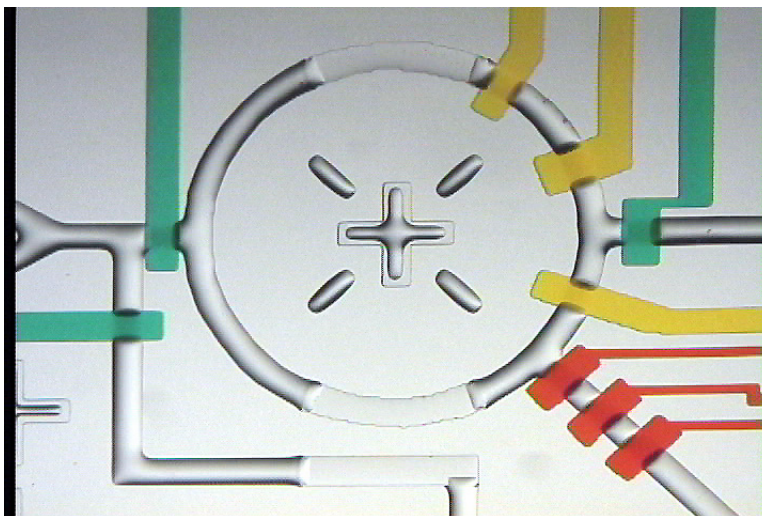
Figure 70: Optical micrograph of mixing ring structure molded from hybrid 5740-SU8 master. 10 μm high observation windows of rectangular cross section allow for precise absorption measurements.

SU8 resists are the most practical option if feature heights in excess of 40 μm are needed in combination with relatively thin (10 μm - 20 μm) valve-compatible channels. In such cases the SU8 features must be added after 5740 processing is complete since the spin-coating of 5740 onto the high SU8 features would result in a poor quality film of uneven thickness. The requirement that the SU8 be added after the 5740 presents a non-trivial technical problem in that the SU8 processing is incompatible with 5740 photo-resist; SU8 developer quickly dissolves 5740 features. After considerable investigation it was found that a standard reflow of 5740 features followed by hard-baking at temperatures above 180 °C for 1 hour resulted in a permanent chemical change to the 5740 photo-resist. Films baked at this elevated temperature exhibit a pronounced change in color, going from dark red to black, but remain optically smooth. Provided that a sufficiently long reflow bake (120 °C for 1.5 hrs) is done prior to hard baking no significant deformation of features is observed.

Hard-baked films were not damaged by SU8 processing, and were further found to be extremely resistant to a variety of solvents including acetone, isopropyl alcohol, and cyclo-benzene; in fact a solvent was not discovered that would remove the film. The elevated bake temperature is crucial to the success of this process. Hard-baking overnight at 150 °C, the first protection protocol that was tried, did not produce chemically resilient films. An important point is that thick SU8 films are highly stressed and are prone to cracking so that thermal shock due to rapid heating or cooling should be avoided. In practice this is easily achieved by temperature ramping protocols or by simply using the thermal mass of the oven/hot-plate to achieve gradual temperature changes. A microfabricated mold featuring

and array of 50 μm high SU8 channels joined to rounded 13 μm high 5740 channels is shown in Figure 71.
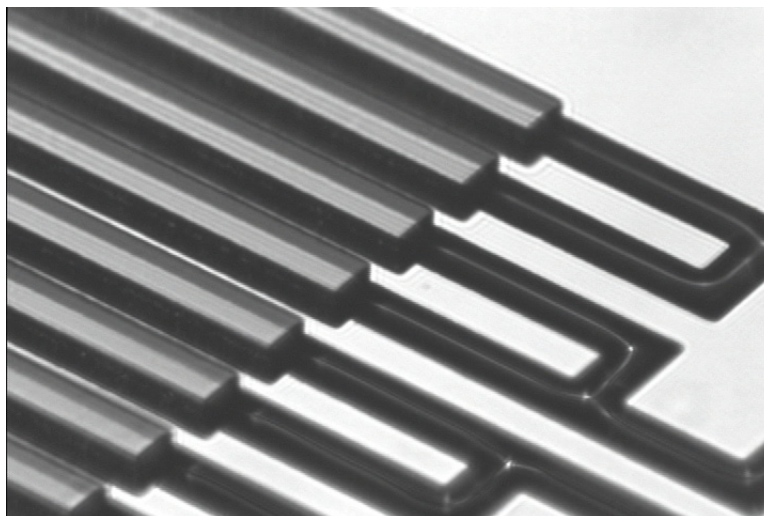
Figure 71: Hybrid 5740-SU8 negative master with 50 μm tall SU8 features fabricated on top of rounded 13 μm high 5740.

Microfluidic Filters

Many applications require the capture of beads or cells during buffer exchange steps or column stacking. This may be achieved by a simple size filter formed by a section of channel that is constricted in height or width. Since beads may be less than 1 μm in radius, very high-resolution lithography is required to implement filters based on lateral constrictions. Alternatively, vertical constrictions may be easily implemented using multilevel molds as described above. A significant consideration in the design and fabrication of features that are highly constricted in the vertical dimension is the possibility of channel collapse during MSL processing. It was found that channel structures having

aspect ratios of 1:10 and heights of 10 μm spontaneously collapsed during alignment of elastomer layers. This process was observed to nucleate in a section of channel and then propagate along the channel length, "zipping up" the channel feature. This problem was eventually overcome by increasing the channel aspect ratio and by optimizing elastomer curing times.

Vertical constrictions due to multilevel mold features are "hard-wired" into a device, creating permanent filters. Removable filters are useful in many applications, such as buffer exchange or cell capture, that only require particles to be impeded intermittently. Such a filter can be easily realized by the partial actuation of a membrane valve. Precise control of the pressure applied to a valve may be used to sufficiently constrict but not close a channel so that particles may not pass. Tuning the actuation pressure of such a filter allows for the filter cutoff size to be dynamically controlled. This strategy has been implemented in the capture of cells for CDNA analysis (31). A major disadvantage to this scheme is that the filter cutoff size is very sensitive to the actuation pressure, making it inconvenient and difficult to automate. Furthermore, perturbations to the pressure in the flow or control structure arising from peripheral valve actuations can result in the escape of trapped particles.

To circumvent these limitations removable filters that are insensitive to actuation pressure can be formed by membrane actuators located in sections of channel with rectangular cross section. Deflection of a membrane into a square channel results in incomplete closure of the channel with small gaps remaining at the channel corners. Sub-micron gaps are easily

achieved in these structures over a broad range of actuation pressures so that no analogue control of the actuation pressure is required. These filters may be molded from masters made using multi-step lithography to include sections of channel made from SU8 (Figure 72). These filters have been used for column stacking in applications including on-chip chemical synthesis and single cell CDNA analysis (J. Marcus in personal communication).
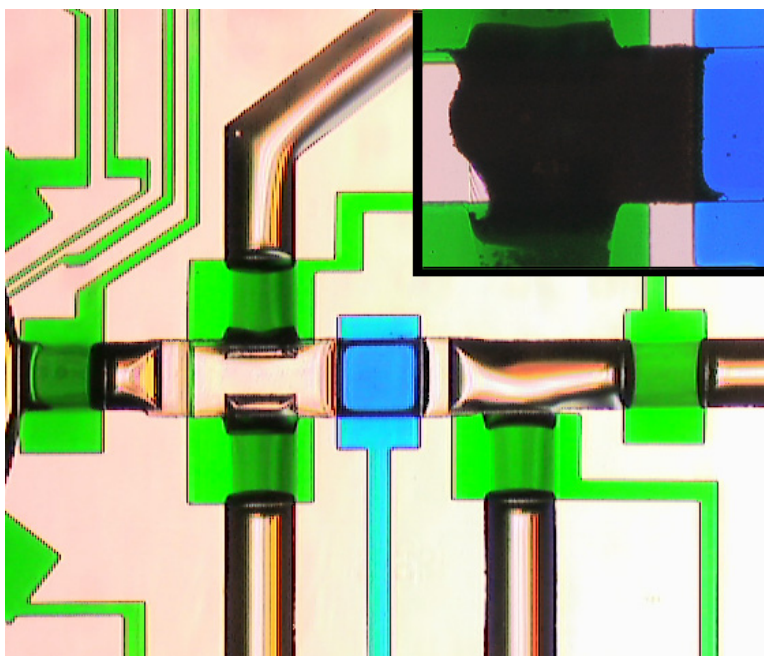
Figure 72: Section of a microfluidic device designed for mRNA capture. Removable filter (blue) is used to stack functionalized beads for affinity capture (inset). Figure courtesy of J. Marcus.

Microwell Fabrication

The integration of microwell structures with increased feature heights allows for reaction volumes to be increased while maintaining small component footprint and minimizing

diffusion times. Tall microwell structures also allow for improved sensitivity in fluorescence and absorbance measurements by providing increased optical path length. Multilevel molds may be used in conjunction with push-up valves to fabricate channel and well structures in a single molding step. An optical micrograph of a multilevel mold having an array of 65 μm high microwells connected by 13 μm high flow channels is shown in Figure 73. The incorporation of microwells or other tall features in the flow channel mold implies that only the push-up valve geometry may be used since a silicone film thick enough to cover the features will result in membranes that are too thick for actuation at reasonable pressures.
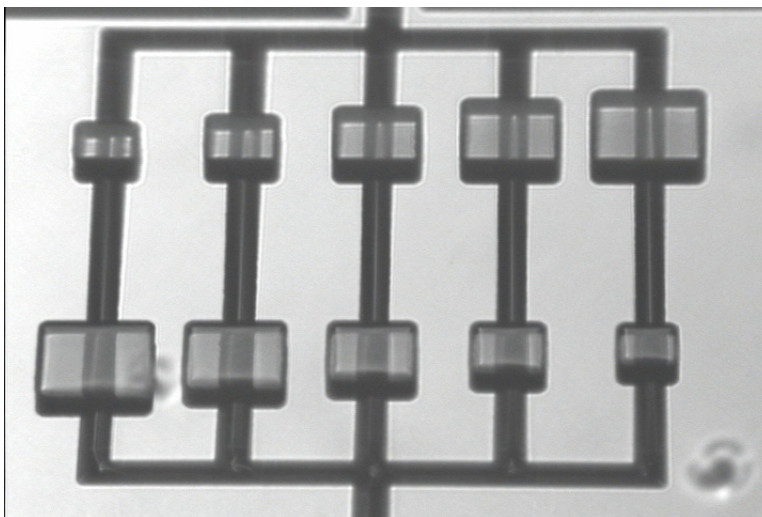
Figure 73: Negative master with 65 μm high microwells fabricated in SU8 2075 resist on top of 10 μm high rounded 5740 channels.

The simultaneous molding of microwells and channel structures has the advantage that no subsequent elastomer alignment step of the channels to the wells is required. Alternatively,

the flow structure may be aligned and bonded to a substrate in which microwells have been separately fabricated. This scheme allows for push-down valve geometry to be used and has the advantage that a reversible substrate bond can be formed that allows for access to the microwells for the recovery of reaction products. In particular, a robust reversible bond can be formed between an elastomer flow structure and a glass substrate with etched microwells. An important advantage of this geometry is that the reagents are in direct contact with the substrate, allowing for the straightforward integration of sensing elements including electrodes, waveguides, ligands, and metallized films for surface plasmon resonance.

A procedure was developed for etching microwells in soda lime and borosilicate crown microscope slides. The glass slides are patterned with photoresist (Shipley SJR 5740) using a negative high-resolution transparency film as a mask. The back of the slides are then masked with an additional layer of photo-resist and hard-baked at 125 °C for 20 minutes to protect them during etching. Etching is performed at 25 °C with propeller agitation in equal parts of dionized water, 1 N hydrochloric acid, and buffered oxide etchant (6 ammonium fluoride: 1 hydrofluoric acid, Transene Company). The addition of hydrochloric acid prevents the re-deposition of insoluble fluoride salts formed by impurity elements in the soda lime and borosilicate crown glass substrates (101). Figure 74: Optical micrographs of features etched in soda lime glass. (A) Rough etch surface due to the formation of insoluble fluoride salts. (B) Addition of 1 N HCl to etchant results in smooth etch. shows a comparison between borosilicate crown glass slides etched with straight buffered oxide etchant and in the presence of 1 N hydrocholoric acid. Etching for 90

minutes at 25 °C yields a maximum well depth of approximately 80 μm. The slides are then washed in acetone to remove the photoresist, and then cleaned in an acid bath (NanoStrip[TM] Cyantek Corp.).
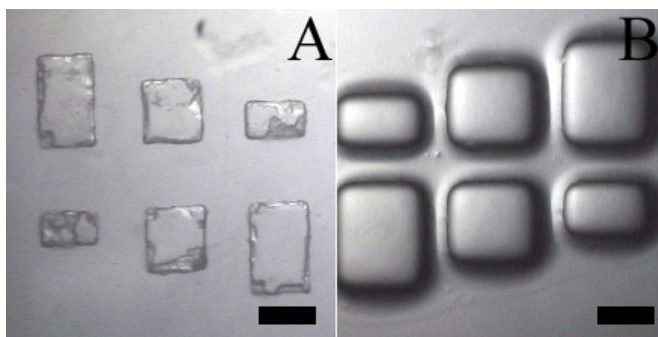
Figure 74: Optical micrographs of features etched in soda lime glass. **(A)** Rough etch surface due to the formation of insoluble fluoride salts. **(B)** Addition of 1 N HCl to etchant results in smooth etch.

APPENDIX A: FABRICATION PROTOCOLS

Fabrication Protocol: Screening Device
3" silicon wafer substrate

Mold Fabrication:

I.   **Flow Mold**

Priming:	HDMS vapor 1 min in tuperware container (STP)
Spin 5740:	2000 rpm x 60 s / 15 s ramp Film thickness = 11 microns
Soft Bake:	contact bake hotplate 110 C x 90 s
Expose Wafer:	define channel structure 45 at 7 mW/cm^2
Develop:	5:1 dilution of Shipley 2401 developer rinse DI H$_2$O dry under nitrogen
Reflow:	contact hotplate 110 C x 40 min
Hard Bake:	in oven ramp 120 C to 180 C hold 1 hr ramp 180 C to 120 C
Spin SU8 50:	500 rpm x 15 s / 15 s ramp 2000 rpm x 40 s / 15 s ramp Film thickness = 60 microns
Pre-Exposure Bake:	contact bake hotplate 5 min x 65 C / 20 min x 95 C
Expose Wafer:	define microwells and low impendence i/o 50 s at 7 mW/cm^2

Post-Exposure Bake: 1 min x 65 C / 12 min x 95 C / 1 min x 65 C

Develop: 100 % Shipley Nanodeveloper
rinse with fresh developer
dry under nitrogen

II.   Control Mold

Spin SU8 2025:   3000 rpm x 45 s / 15 second ramp up
film thickness = 13 microns

Pre-Exposure Bake: contact bake hotplate
1 min x 65 C / 5 min x 95 C

Expose Wafer: define control structure
25 s at 7 mW/cm^2

Post-Exposure Bake: 1 min x 65 C / 5 min x 95 C

Develop: 100 % Shipley Nanodeveloper
rinse with fresh developer
dry under nitrogen

Hard Bake: contact hotplate
150 C x 60 min

MSL Fabrication

Priming: all molds
TMCS vapor 1 min in tuperware container (STP)

Cast Flow Layer: combine 5:1 GE 615 RTV (30 g A: 6 g B)
mix hybrid mixer: 2 min mix / 2 min degas
30 g onto flow mold (petri dish lined with Al foil)

Degas Flow Layer: pull vacuum in bell jar (approx 30 minutes)

Spin Control Layer: combine 20:1 GE 615 RTV (40 g A: 2 g B)
mix hybrid mixer: 2 min mix / 2 min degas
dispense 5 mL on control layer
1800 rpm x 60 s / 15 s ramp*
film thickness = 28 microns

Spin Blank Layer: combine 20:1 GE 615 RTV (40 g A: 2 g B)
mix hybrid mixer: 2 min mix / 2 min degas

dispense 5 mL on blank wafer
2000 rpm x 60 s / 15 s ramp
film thickness = 30 microns

1st Cure Flow Layer: convection oven
80 C x 60 min

1st Cure Control Layer: convection oven
80 C x 40 min

1st Cure Blank Layer: convection oven
80 C x 40 min

Control/Flow Bonding: peel flow layer from mold
align to control layer
bake in convection oven
80 C x 90 min

Puncing I/O Ports: peel bonded device from control mold
punch all flow and control ports

Blank/Control Bonding: place control/flow structure on blank
ensure no air bubbles
ensure no collapsed valves
bake in convection oven
80 C x 3 hours

Dicing: cut around periphery of thick layer
peel from substrate
dice into separate devices

Substrate Mounting: rinse bottom of devices with ethanol
dry under nitrogen
rinse glass slides with ethanol
dry under nitrogen
put device on slide
ensure no air bubbles
bake in convection oven
80 C x 12 hours

* spin parameters need to be optimized for each batch.

Fabrication Protocol: Formulator Device
3" silicon wafer substrate

Mold Fabrication:

I.   **Flow Mold**

Spin SU8 2015:   3000 rpm x 70 s / 15 second ramp up
                           film thickness = 13 microns

Pre-Exposure Bake: contact bake hotplate
                           1 min x 65 C / 3 min x 95 C

Expose Wafer: define observation windows
                           25 s at 7 mW/cm^2

Post-Exposure Bake: 1 min x 65 C / 4 min x 95 C

Develop: 100 % Shipley Nanodeveloper
                           rinse with fresh developer
                           dry under nitrogen

Wash: spin and rinse with acetone and isopropyl alcohol

Hard Bake: contact bake hotplate
                           150 C x 60 min

Priming: HDMS vapor 1 min in tuperware container (STP)

Spin 5740:   1500 rpm x 60 s / 15 s ramp
                           Film thickness = 12.5 microns

Soft Bake: contact bake hotplate
                           110 C x 90 s
Expose Wafer: define channel structure
                           45 at 7 mW/cm^2

Develop: 5:1 dilution of Shipley 2401 developer
                           rinse DI H$_2$O
                           dry under nitrogen

Reflow: contact hotplate
                           110 C x 40 min

Hard Bake: in oven

ramp 120 C to 180 C
hold 1 hr
ramp 180 C to 120 C

Spin SU8 50:	500 rpm x 15 s / 15 s ramp
	3000 rpm x 40 s / 15 s ramp
	Film thickness = 42 microns
Pre-Exposure Bake:	contact bake hotplate
	5 min x 65 C / 15 min x 95 C
Expose Wafer:	define low impendence i/o
	50 s at 7 mW/cm^2
Post-Exposure Bake:	1 min x 65 C / 7 min x 95 C / 1 min x 65 C
Develop:	100 % Shipley Nanodeveloper
	rinse with fresh developer
	dry under nitrogen

II.   Control Mold

Spin SU8 2025:	3000 rpm x 45 s / 15 second ramp up
	film thickness = 13 microns
Pre-Exposure Bake:	contact bake hotplate
	1 min x 65 C / 5 min x 95 C
Expose Wafer:	define control structure
	25 s at 7 mW/cm^2
Post-Exposure Bake:	1 min x 65 C / 5 min x 95 C
Develop:	100 % Shipley Nanodeveloper
	rinse with fresh developer
	dry under nitrogen
Hard Bake:	contact hotplate
	150 C x 60 min

MSL Fabrication

Priming:	all molds
	TMCS vapor 1 min in tuperware container (STP)
Cast Flow Layer:	combine 5:1 GE 615 RTV (30 g A: 6 g B)

	mix hybrid mixer: 2 min mix / 2 min degas 30 g onto flow mold (petri dish lined with Al foil)
Degas Flow Layer:	pull vacuum in bell jar (approx 30 minutes)
Spin Control Layer:	combine 20:1 GE 615 RTV (40 g A: 2 g B) mix hybrid mixer: 2 min mix / 2 min degas dispense 5 mL on control layer 1800 rpm x 60 s / 15 s ramp* film thickness = 28 microns
Spin Blank Layer:	combine 20:1 GE 615 RTV (40 g A: 2 g B) mix hybrid mixer: 2 min mix / 2 min degas dispense 5 mL on blank wafer 2000 rpm x 60 s / 15 s ramp film thickness = 30 microns
1st Cure Flow Layer:	convection oven 80 C x 60 min
1st Cure Control Layer:	convection oven 80 C x 40 min
1st Cure Blank Layer:	convection oven 80 C x 40 min
Control/Flow Bonding:	peel flow layer from mold align to control layer bake in convection oven 80 C x 90 min
Puncing I/O Ports:	peel bonded device from control mold punch all flow and control ports
Blank/Control Bonding:	place control/flow structure on blank ensure no air bubbles ensure no collapsed valves bake in convection oven 80 C x 3 hours
Dicing:	cut around periphery of thick layer peel from substrate dice into separate devices
Substrate Mounting:	rinse bottom of devices with ethanol dry under nitrogen

rinse glass slides with ethanol
dry under nitrogen
put device on slide
ensure no air bubbles
bake in convection oven
80 C x 12 hours

* spin parameters need to be optimized for each batch.

Fabrication Protocol: Diffraction Device
3" silicon wafer substrate

Mold Fabrication:

I.   Reservoir Molds

Spin SU8 2025:   3000 rpm x 45 s / 15 second ramp up
                        film thickness = 13 microns

Pre-Exposure Bake: contact bake hotplate
                        1 min x 65 C / 5 min x 95 C

Expose Wafer: define reservoirs
                        25 s at 7 mW/cm^2

Post-Exposure Bake: 1 min x 65 C / 5 min x 95 C

Develop: 100 % Shipley Nanodeveloper
                        rinse with fresh developer
                        dry under nitrogen

II.   Flow Mold

Priming: HDMS vapor 1 min in tuperware container (STP)

Spin 5740:   900 rpm x 50 s / 5 s ramp
                        Film thickness = 16 microns

Soft Bake: contact bake hotplate
                        110 C x 100 s

Expose Wafer: define channel structure
                        70 at 7 mW/cm^2

Develop: 7:1 dilution of Shipley 2401 developer
                        rinse DI H_2O
                        dry under nitrogen

Reflow: contact hotplate
                        115 C x 25 min

Hard Bake: in oven
                        ramp 120 C to 180 C
                        hold 1 hr

	ramp 180 C to 120 C
Spin SU8 100:	1500 rpm x 60 s / 15 s ramp Film thickness = 150 microns sit for 15 minutes on flat level surface
Pre-Exposure Bake:	contact bake on level hotplate 5 min x 65 C / 30 min x 95 C / 1 min 65 C cool to room temperature
Expose Wafer:	define microwells and high i/o 130 s at 7 mW/cm^2
Post-Exposure Bake:	2 min x 65 C / 12 min x 95 C / 1 min x 65 C
Develop:	100 % Shipley Nanodeveloper rinse with fresh developer dry under nitrogen

III.   Control Mold

Spin SU8 2025:	3000 rpm x 45 s / 15 second ramp up film thickness = 13 microns
Pre-Exposure Bake:	contact bake hotplate 1 min x 65 C / 5 min x 95 C
Expose Wafer:	define control structure 25 s at 7 mW/cm^2
Post-Exposure Bake:	1 min x 65 C / 5 min x 95 C
Develop:	100 % Shipley Nanodeveloper rinse with fresh developer dry under nitrogen
Hard Bake:	contact hotplate 150 C x 60 min

MSL Fabrication

Priming:	all molds TMCS vapor 5 min in tuperware container (STP)
Cast Through Layer:	combine 5:1 GE 615 RTV (36 g A: 7 g B)

mix hybrid mixer: 2 min mix / 2 min degas
36 g onto flow mold (petri dish lined with Al foil)

Degas Through Layer: pull vacuum in bell jar (approx 30 minutes)

Spin Flow Layer 1:   combine 5:1 GE 615 RTV (30 g A: 6 g B)
mix hybrid mixer: 2 min mix / 2 min degas
dispense 5 mL on flow layer
350 rpm x 60 s / 10 s ramp*
film thickness = 180 microns

Degas Flow Layer: pull vacuum in bell jar (approx 30 minutes)

Spin Control Layer: combine 20:1 GE 615 RTV (40 g A: 2 g B)
mix hybrid mixer: 2 min mix / 2 min degas
dispense 5 mL on control layer
1800 rpm x 60 s / 15 s ramp*
film thickness = 28 microns

Spin Blank Layer: combine 20:1 GE 615 RTV (40 g A: 2 g B)
mix hybrid mixer: 2 min mix / 2 min degas
dispense 5 mL on blank wafer
2000 rpm x 60 s / 15 s ramp
film thickness = 30 microns

1st Cure Through Layer: convection oven
80 C x 80 min

1st Cure Flow Layer: convection oven
80 C x 60 min

Spin Flow Layer 2:   combine 20:1 GE 615 RTV (40 g A: 2 g B)
mix hybrid mixer: 2 min mix / 2 min degas
dispense 5 mL on blank wafer
2000 rpm x 60 s / 15 s ramp
film thickness = 30 microns

2nd Cure Control Layer: convection oven
80 C x 20 min

Punching Reservoirs: peel through layer from mold
punch reservoir through holes

Through/Flow Bonding: peel through layer from mold
align to flow layer
bake in convection oven

80 C x 60 min

1st Cure Control Layer: convection oven
80 C x 40 min

Control/Flow Bonding: peel flow layer from mold
take care to not rip membranes
align to control layer
ensure no air bubbles under membranes
ensure no collapsed valves
bake in convection oven
80 C x 70 min

1st Cure Blank Layer: convection oven
80 C x 40 min

Puncing I/O Ports: peel bonded device from control mold
punch all flow and control ports

Blank/Control Bonding: place control/flow structure on blank
pull vacuum to ensure no air bubbles
ensure no collapsed valves
bake in convection oven
80 C x 12 hours

Dicing: cut around periphery of thick layer
peel from substrate
cut device to shape

Substrate Mounting: rinse bottom of device with ethanol
dry under nitrogen
rinse glass slides with ethanol
dry under nitrogen
put device on slide
pull vacuum to ensure no air bubbles
bake in convection oven
80 C x 12 hours

* spin parameters need to be optimized for each batch.

APPENDIX B: MATLAB SCRIPT FOR MIXING SIMULATIONS

```
%      Program for simulating dispersion in tube or rotary mixer for a %
       given flow    %   velocity profile.

%      data input

filename = input('enter function filename: ','s');
fid = fopen(filename, 'w'); % open functionfile

dif = input('diffusion constant(um*um/s): ');
fprintf(fid, 'Diffusion constant (um*um/s): %6f\n', dif);

inic = input('initial concetration: ');
fprintf(fid, 'Initial concentration: %6f\n', inic);

vel = input('max velocity(um/s): ');
fprintf(fid, 'Max velocity (um/s): %6f\n', vel);

xl = input('length of tube (nodes): ');
fprintf(fid, 'Number of nodes in x-dir: %6f\n', xl);

yl = input('width of tube (nodes): ');
fprintf(fid, 'Number of nodes in y-dir: %6f\n', yl);

time = input('simulationb time: ');
fprintf(fid, 'Simulation time (s): %6f\n', time);

dx = input('um pr node x-dir: ');
fprintf(fid, 'Spatial step size in x-dir (um/node): %6f\n', dx);

dy = input('um pr node y-dir: ');
fprintf(fid, 'Spatial step size in y-dir (um/node): %6f\n', dy);

dt = input('timesteps (s): ');
fprintf(fid, 'Time step (s) %6f\n', dt);

slugl = input('slug length(nodes): ');
fprintf(fid, 'Initial length of slug (x-dir nodes): %6f\n', slugl);

numpic = input('number of pictures saved in matrix ct: ');
fprintf(fid, 'Number of events saved (i.e. matrices below): %6f\n',
numpic);


inicond = (x1, y1, time,dx,dy,dt,slug);


%      calculation of timeresolution and initial matrix


stepcount = 1;
lastcount = time/dt;


channelnl = xl + 100;
```

```
c = zeros(channelnl,yl);
inidom = (100+slugl);
c(101:inidom,:) = ones;
c = c*inic;
ctemp = c;
ct = zeros(channelnl,yl*10);

%     discretize velocity profile


v = zeros(yl,1);
n = 1;
while n <= yl
      v(n,1) = -vel*(4/((yl-1)*(yl-1)))*((n-1)*(n-1) - (n-1)*(yl-1));
      n=n+1;
end

%     do calculations


q=1;

while stepcount <= lastcount


%     lower noflux boundary y-1 = y+1
    y = 1;
    x = 2;
    n = y;
      while x < (xl + 97)
            ctemp(x,y) = (dif*dt/(dx*dx))*(c(x+1,y) - 2*c(x,y)
            + c(x-1,y)) + (dif*dt/(dy*dy))*(c(x,y+1) -2*c(x,y)
            + c(x,y+1)) + (v(n,1)*dt/dx)*(-c(x,y) + c(x-1,y))
            + c(x,y);
            x = x+1;
      end


%     high noflux boundary y+1 = y-1
    y = yl;
    x = 2;
    n = y;
      while x < (xl + 98)
            ctemp(x,y) = (dif*dt/(dx*dx))*(c(x+1,y) - 2*c(x,y)
            + c(x-1,y)) + (dif*dt/(dy*dy))*(c(x,y-1) -2*c(x,y)
            + c(x,y-1)) + (v(n,1)*dt/dx)*(-c(x,y) + c(x-1,y))
            + c(x,y);
            x = x+1;
      end
    y = 2;
    n = 2;
      while y < yl
            x = 2;
            while x < (xl + 98)
                  ctemp(x,y) = (dif*dt/(dx*dx))*(c(x+1,y) - 2*c(x,y)
                  + c(x-1,y)) + (dif*dt/(dy*dy))*(c(x,y+1) -2*c(x,y)
```
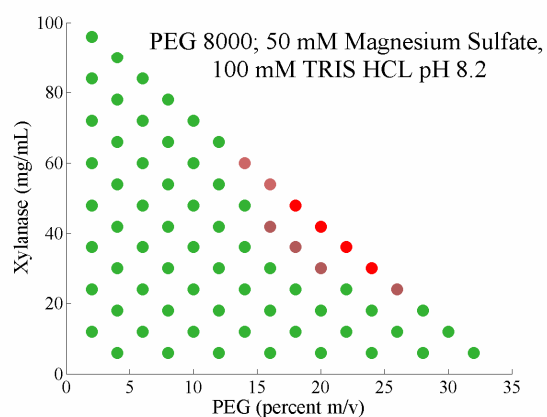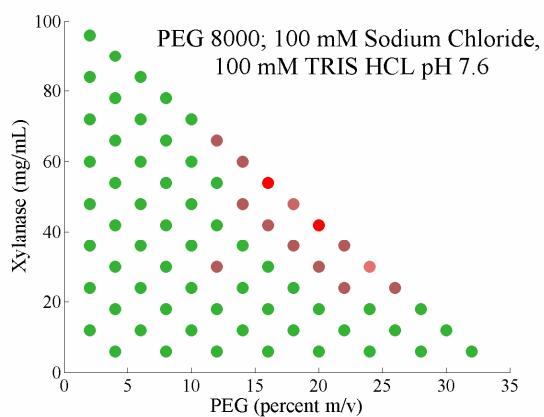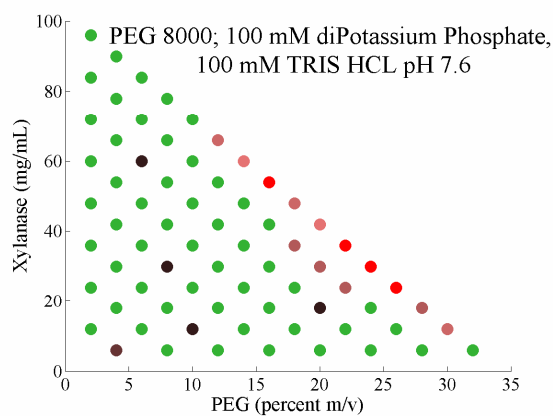
```
                    + c(x,y-1)) + (v(n,1)*dt/dx)*(-c(x,y) + c(x-1,y))
                    + c(x,y);
                    x = x+1;
            end
            y = y+1;
            n = y;
    end
    c = ctemp;

    if stepcount > q*lastcount/numpic
        ct(:,(q*yl-(yl-1)):q*yl)=c;
        tau = dt*q*lastcount/numpic
        x=1;
        while x<=channelnl
            y=1;
            while y <=yl
                fprintf(fid, '%6f\n', c(x,y));
                y=y+1;
            end
            x=x+1;
        end
        q = q+1;
        fprintf(fid,'\n');
    end
    stepcount = stepcount + 1


end
fclose(fid);
```
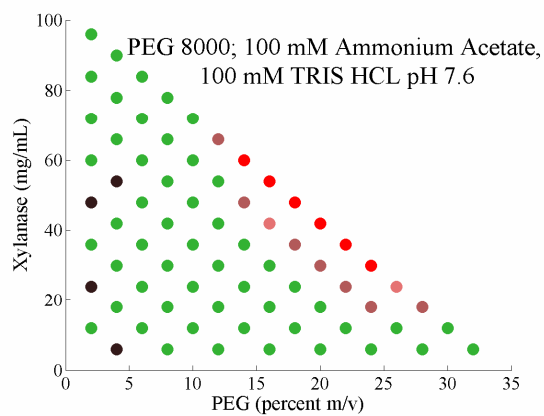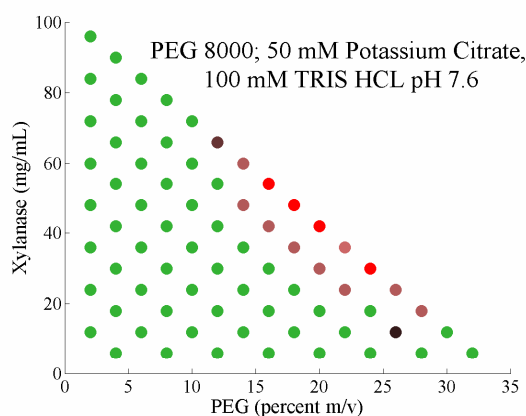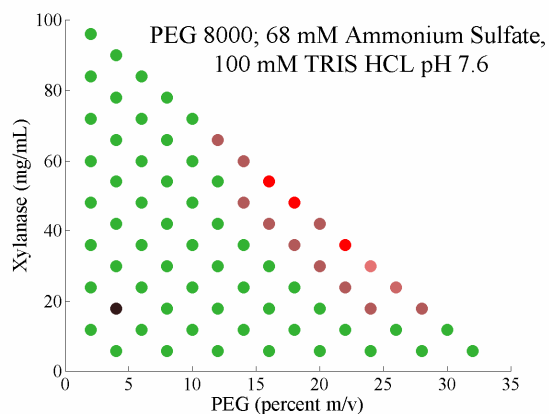
APPENDIX C: PHASE-SPACE DIAGRAMS
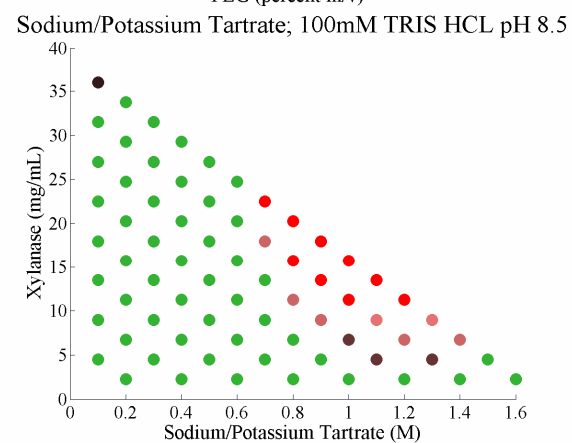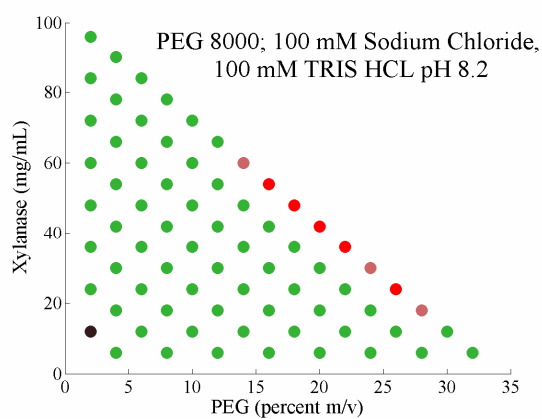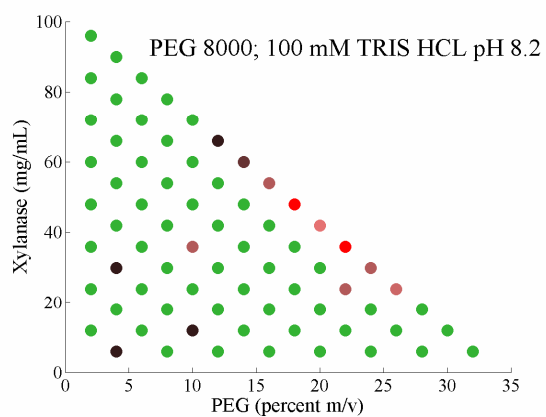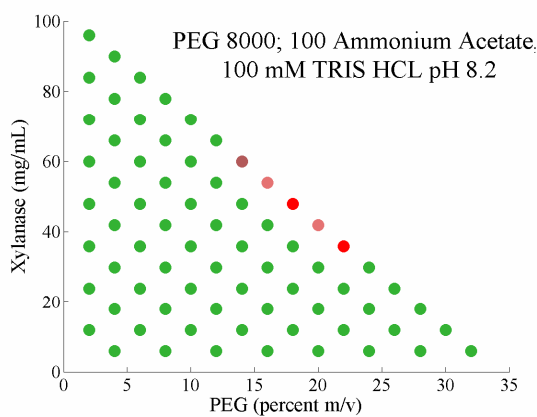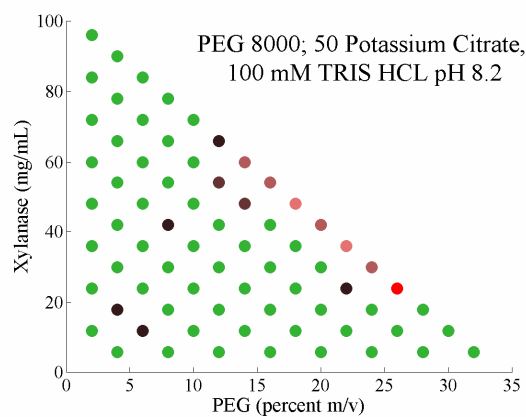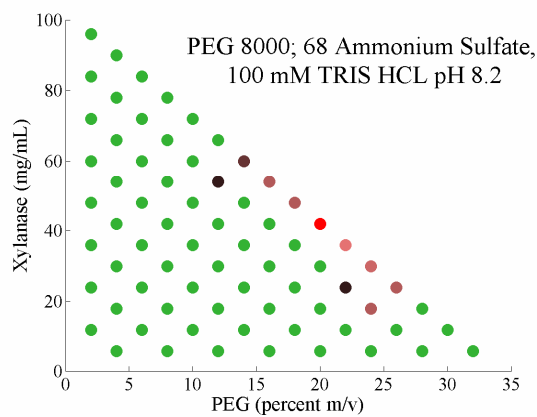
Sodium/Potassium Tartrate; 100mM TRIS HCL pH 6.5
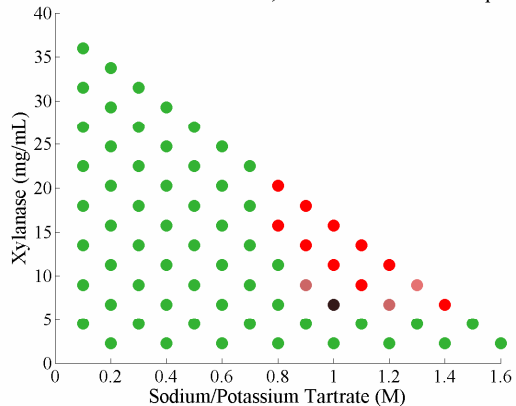
Ammonium Sulfate; 100mM TRIS HCl pH 8.5
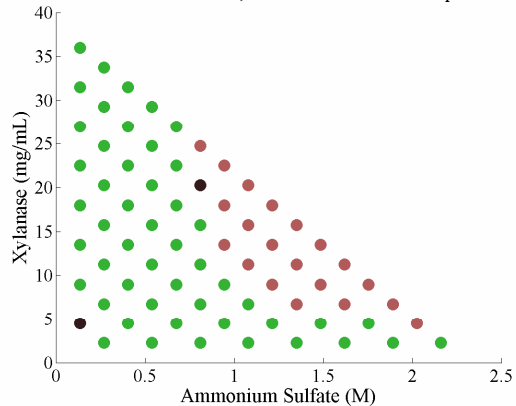
Sodium/Potassium Tartrate; 100mM Sodium Citrate pH 4
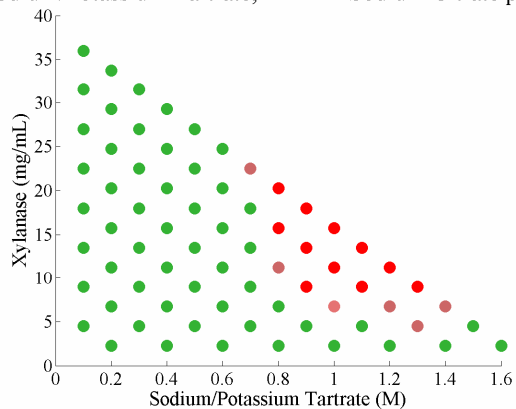
Ammonium Sulfate; 100mM TRIS HCl pH 6.5
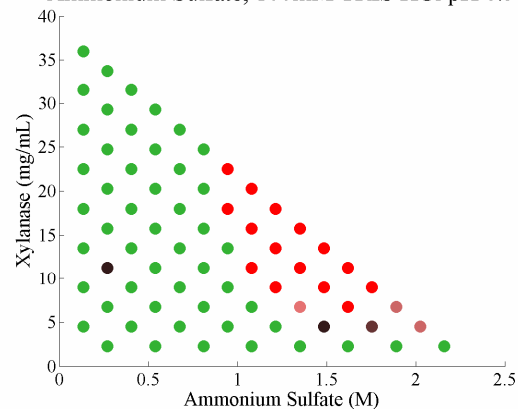
Ammonium Sulfate; 100mM Sodium Citrate pH 4.6

diPotassium Phosphate; 100mM TRIS HCl pH 8.5

diPotassium Phosphate; 100mM TRIS HCl pH 6.5

diPotassium Phosphate; 100mM Sodium Citrate pH 4.6

Sodium Citrate; 100mM TRIS HCl pH 8.5

Sodium Citrate; 100mM TRIS HCl pH 6.5

Sodium Citrate; 100mM Sodium Citrate pH 4.6

PEG 8000; 50 mM Magnesium Sulfate, 100 mM TRIS HCL pH 7.6
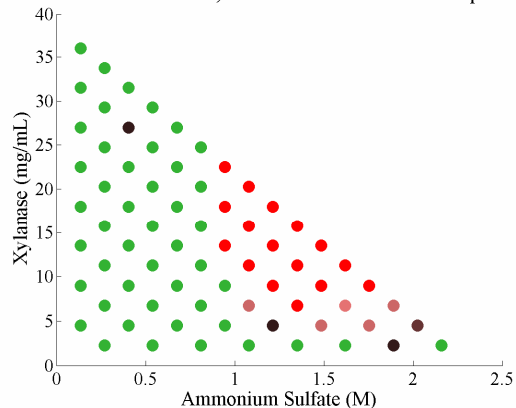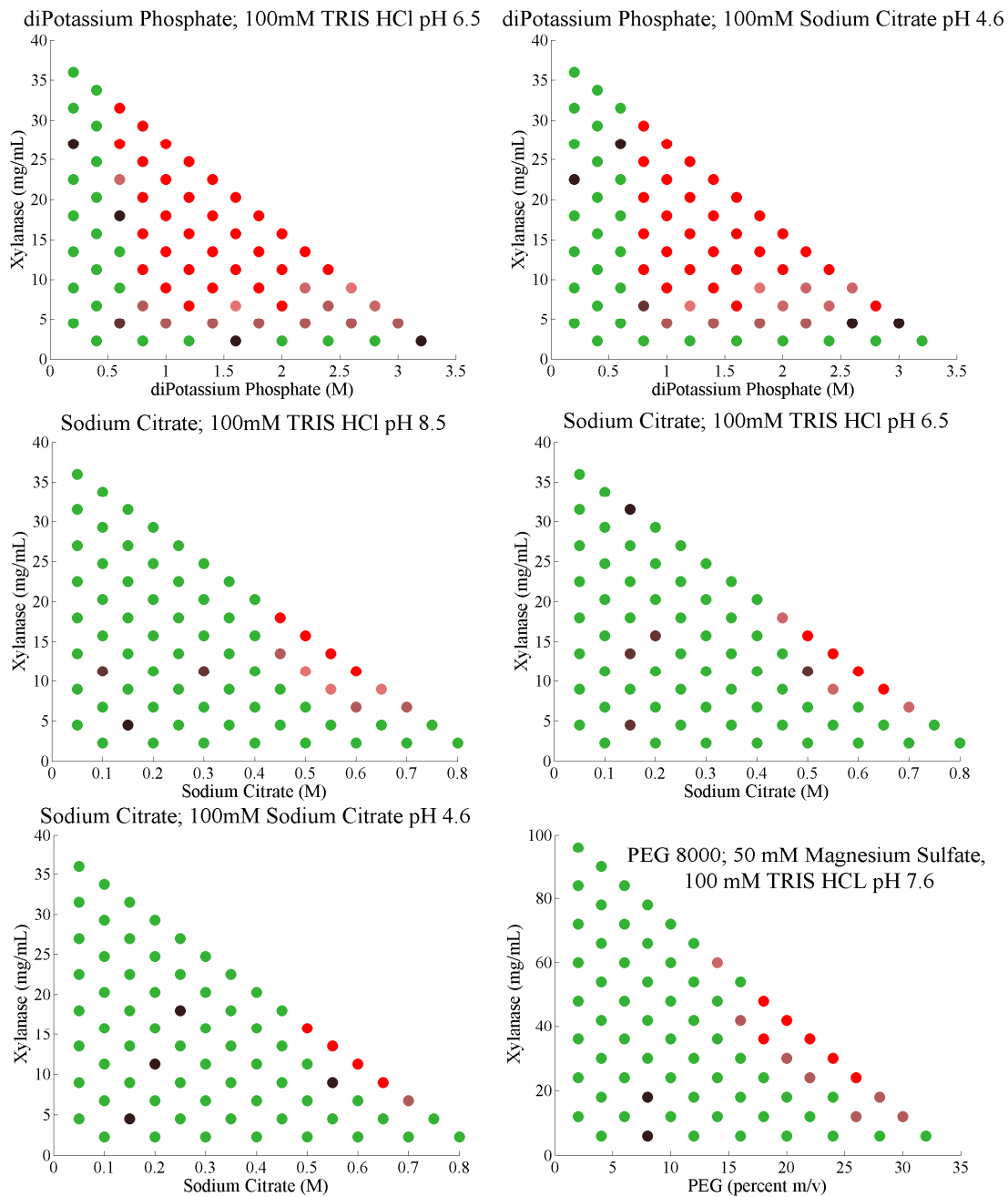
APPENDIX D: CRYSTALLIZATION RESULTS FOR OPTIMAL SCREENING

Optimal Xylanase Crystallization Screen Based on Phase-space Mapping

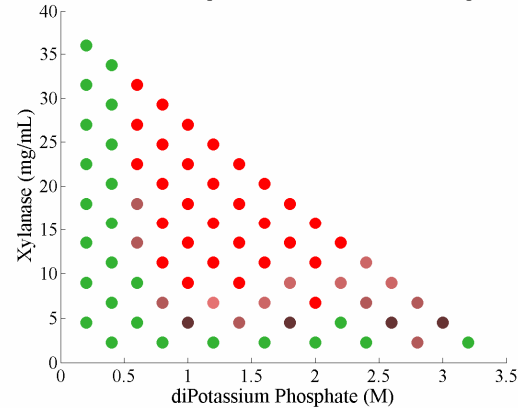| #	Buffer	pH	Conc M	Prec1	Conc M	Prec2	Conc M	Prot. mg/mL
1	NaCitrate	4.6	0.1	NaCitrate	0.65	none	N/A	7
2	NaCitrate	4.6	0.1	NaCitrate	0.475	none	N/A	17
3	Tris/HCL	6.5	0.1	NaCitrate	0.7	none	N/A	5
4	Tris/HCL	6.5	0.1	NaCitrate	0.5	none	N/A	9
5	Tris/HCL	8.45	0.1	NaCitrate	0.425	none	N/A	19
6	Tris/HCL	8.45	0.1	NaCitrate	0.475	none	N/A	9.5
7	NaCitrate	4.6	0.1	Na/K Tart	1.1	none	N/A	6.5
8	NaCitrate	4.6	0.1	K2HPO4	0.8	none	N/A	9
9	NaCitrate	4.6	0.1	K2HPO4	1.8	none	N/A	6.75
10	Tris/HCL	6.5	0.1	K2HPO4	0.6	none	N/A	24.75
11	Tris/HCL	6.5	0.1	Na/K Tart	0.75	none	N/A	21
12	Tris/HCL	8.45	0.1	K2HPO4	2.8	none	N/A	6.75
13	NaCitrate	4.6	0.1	(NH4)2SO4	1.08	none	N/A	9
14	Tris/HCL	6.5	0.1	(NH4)2SO4	1.89	none	N/A	4.5
15	Tris/HCL	8.45	0.1	(NH4)2SO4	0.81	none	N/A	24.75
16	NaCitrate	4.6	0.1	K2HPO4	2.8	none	N/A	3.5
17	NaCitrate	4.6	0.1	Na/K Tart	0.75	none	N/A	17
18	Tris/HCL	8.45	0.1	K2HPO4	0.4	none	N/A	31.5
19	NaCitrate	4.6	0.1	(NH4)2SO4	0.945	none	N/A	23.62
20	Tris/HCL	6.5	0.1	Na/K Tart	1.4	none	N/A	4.5
21	Tris/HCL	6.5	0.1	(NH4)2SO4	1.35	none	N/A	9
22	Tris/HCL	8.45	0.1	Na/K Tart	0.9	none	N/A	6.75
23	Tris/HCL	8.45	0.1	Na/K Tart	0.7	none	N/A	13.5
24	Tris/HCL	8.45	0.1	(NH4)2SO4	1.755	none	N/A	4.5
25	Tris/HCL	8.2	0.1	P8000	16	NaCl	0.1	42
26	Tris/HCL	8.2	0.1	P8000	23	NaCl	0.1	21
27	Tris/HCL	8.2	0.1	P8000	15	None	N/A	54
28	Tris/HCL	8.2	0.1	P8000	24	None	N/A	30
29	Tris/HCL	8.2	0.1	P8000	28	Am Aoc	0.1	18
30	Tris/HCL	8.2	0.1	P8000	19	Am Aoc	0.1	33
31	Tris/HCL	8.2	0.1	P8000	14	Am Aoc	0.1	60
32	Tris/HCL	8.2	0.1	P8000	20	K Citrate	0.05	42
33	Tris/HCL	8.2	0.1	P8000	14	K Citrate	0.05	60
34	Tris/HCL	8.2	0.1	P8000	16	K Citrate	0.05	36
35	Tris/HCL	8.2	0.1	P8000	24	(NH4)2SO4	.0675	18
36	Tris/HCL	8.2	0.1	P8000	24	(NH4)2SO5	.0675	6
37	Tris/HCL	8.2	0.1	P8000	10	MgSO4	0.05	66
38	Tris/HCL	8.2	0.1	P8000	16	MgSO4	0.05	30
39	Tris/HCL	8.2	0.1	P8000	18	MgSO4	0.05	36
40	Tris/HCL	7.6	0.1	P8000	12	NaCl	0.1	66
41	Tris/HCL	7.6	0.1	P8000	28	NaCl	0.1	18
42	Tris/HCL	7.6	0.1	P8000	30	K2HPO4	0.1	12
43	Tris/HCL	7.6	0.1	P8000	22	K2HPO5	0.1	12
44	Tris/HCL	7.6	0.1	P8000	16	K2HPO6	0.1	42
45	Tris/HCL	7.6	0.1	P8000	18	NH4AOc	0.1	36
46	Tris/HCL	7.6	0.1	P8000	28	K Citrate	0.05	18
47	Tris/HCL	7.6	0.1	P8000	16	(NH4)2SO4	.0675	54
48	Tris/HCL	7.6	0.1	P8000	30	MgSO4	0.05	12

Bibliography

1.   Hooke, R. (1665) *Micrographia*.

2.   Sali, A., Glaeser, R., Earnest, T. & Baumeister, W. (2003) *Nature* **422,** 216-225.

3.   Ogata, C. M. (1998) *Nature Structural Biology* **5,** 638-640.

4.   Cusack, S., Belrhali, H., Bram, A., Burghammer, M., Perrakis, A. & Riekel, C. (1998) *Nat. Struct. Biol.* **5,** 634-637.

5.   Perrakis, A., Morris, R. & Lamzin, V. S. (1999) *Nat Struct Biol* **6,** 458-463.

6.   Chayen, E. N. (2002) *Trends in Biotechnology* **20,** 98-98.

7.   Loll, P. J. (2003) *Journal of Structural Biology* **142,** 144-153.

8.   Torres, J., Stevens, T. J. & Samso, M. (2003) *Trends in Biochemical Science* **28,** 174-174.

9.   Edwards, A. M., Kus, B., Jansen, R., Greenbaum, D., Greenblatt, J. F. & Gerstein, M. (2004) *Drug Discovery Today* **9,** S32-S40.

10.   Beebe, D. J., Mensing, G. A. & Walker, G. M. (2002) *Annual Review of Biomedical Engineering* **4,** 261-286.

11.   Manz, A. & Eijkel, J. C. T. (2001) *Pure and Applied Chemistry* **73,** 1555-1561.

12.   Sia, S. K. & Whitesides, G. M. (2003) *Electrophoresis* **24,** 3563-3576.

13.   Unger, M. A., Chou, H. P., Thorsen, T., Scherer, A. & Quake, S. R. (2000) *Science* **288,** 113-116.

14.   Chou, H., Unger, M. A. & Quake, S. R. (2001) *Biomedical Microdevices* **3,** 323-330.

15.   Carter, C. W., Baldwin, E. T. & Frick, L. (1988) *Journal of Crystal Growth* **90,** 60-73.

16.   Hansen, C. L. & Quake, S. R. (2003) *Current opinion in structural biology* **13,** 538-544.

17.   Jenson, D. J. (1998) *Nature* **393,** 735-737.

18.   Jacobson, S. C., McKnight, T. E. & Ramsey, J. M. (1999) *Analytical Chemistry* **71,** 4455-4459.

19.   Kanholz, A. E., Weigl, B. H., Finlayson, B. A. & Yager, P. (1999) *Analytical Chemistry* **71,** 5340-5347.

20.   Dertinger, S. K. W., Chiu, C. Y., Jeon, N. L. & Whitesides, G. M. (2001) *Analytical Chemistry* **73,** 1240-1246.

21.   Zhang, C. & Manz, A. (2001) *Analytical Chemistry* **73,** 2656-2662.

22.   Qui, C. X. & Harrison, D. J. (2001) *Electrophoresis* **22,** 3949-3958.

23.   Brechtel, R., Hoffman, W., Rudinger, H. & Watzig, H. (1995) *Journal of Chromatography A* **716,** 97.

24.   Lucy, C. A. & Underhill, R. S. (1996) *Analytical Chemistry* **68,** 300-305.

25.   Beebe, D. J., Moore, J. S., Bauer, J. M., Yu, Q., Liu, R. H., Devadoss, C. & Jo, B. H. (2000) *Nature* **404,** 588-+.

26.   Quake, S. R. & Scherer, A. (2000) *Science* **290,** 1536-1540.

27.   Thorsen, T., Maerkl, S. J. & Quake, S. R. (2002) *Science* **298**.

28.   Monahan, J., Gewirth, A. A. & Nuzzo, R. G. (2001) *Analytical Chemistry* **73,** 3193-3197.

29. Hansen, C. L., Skordalakes, E., Berger, J. M. & Quake, S. R. (2002) *Proceedings of the National Academy of Sciences of the United States of America* **99,** 16531-16536.

30. Merkel, T. C., Bondar, V. I., Nagai, K., Freeman, B. D. & Pinnau, I. (2000) *Journal of Polymer Science* **38,** 415-434.

31. Hong, J. W., Studer, V., Hang, G., Anderson, W. F. & Quake, S. R. (2004) *Nature Biotechnology* **22,** 435-439.

32. Liu, J., Hansen, C. & Quake, S. R. (2003) *Analytical Chemistry* **75,** 4718-4723.

33. Hansen, C. L., Sommer, M., Self, K., Berger, J. M. & Quake, S. R. (2003) in *Protein Crystallography in Drug Discovery*, eds. Babine, R. & Abdel-Meguid (Wiley-VCH, Weinheim).

34. Jancarik, J. & Kim, S. H. (1991) *Journal of Applied Crystallography* **24,** 409-411.

35. Ai, X. & Caffrey, M. (2000) *Biophysical Journal* **79,** 394-405.

36. Ostermeier, C. & Michel, H. (1997) *Current Opinions in Biotechnolgy* **7,** 697-701.

37. Rosenbusch, J. P. (2001) *Journal of Structural Biology* **136,** 144-157.

38. Cramer, P., Bushnell, D. A., Fu, J. H., Gnatt, A. L., Maier-Davis, B., Thompson, N. E., Burgess, R. R., Edwards, A. M., David, P. R. & Kornberg, R. D. (2000) *Science* **288,** 640-649.

39. Ban, N., Freeborn, B., Nissen, P., Penczek, P., Grassucci, R. A., Sweet, R., Frank, J., Moore, P. B. & Steitz, T. A. (1998) *Cell* **93,** 1105-1115.

40. McPherson, A. (1999) *Crystallization of Biological Macromolecules* (Cold Spring Harbor Laboratory Press, Cold Spring Harbor, New York).

41.   Morse, P. M. (1969) *Thermal Physics* (The Benjamin/Cummings Publishing Company, Inc., London).

42.   Hanggi, P. (1990) *Reviews of Modern Physics* **62,** 251-341.

43.   Boistelle, R. & Astier, J. (1988) *Journal of Crystal Growth* **90,** 14-30.

44.   Luft, J. R. & DeTitta, G. T. (1997) *Methods in Enzymology* **276,** 110-130.

45.   Salemme, F. R. (1972) *Archives of Biochemistry and Biophysics* **151**.

46.   Garcia-Ruiz, J. M., Otalora, F., Novella, M. L., Gavira, J. A., Sauter, C. & Vidal, O. (2001) *Journal of Crystal Growth* **232,** 149-155.

47.   Carotenuto, L., Piccolo, C., Castagnolo, D., Lappa, M., Tortora, A. & Garcia-Ruiz, J. M. (2002) *Acta Crystallographical Section D - Biological Crystallography* **58,** 1628-1632.

48.   Wang, Y. P., Han, Y., Pan, J. S., Wang, K. Y. & Bi, R. C. (1996) *Microgravity Science and Technology* **9,** 281-283.

49.   Garcia-Ruiz, J. M., Novella, M. L., Moreno, R. & Gavira, J. A. (2001) *Journal of Crystal Growth* **232,** 165-172.

50.   Delucas, L. J., C.D., S., Smith, H. W., Vijaykumar, S., Senadhi, S. E., Ealick, S. E., Carter, D. C., Snyder, R. S., Weber, P. C., Salemme, F. R., Ohlendorf, D. H., Einspahr, H. M., Clancy, L. L., Navia, M. A., McKeever, B. M., Nagabhushan, T. L., Nelso, G., McPherson, A., Koszelakk, S., Taylor, G., Stammers, D., Powell, K., Darby, G. & Bugg, C. E. (1989) *Science* **246,** 651-654.

51.   Delucas, L. J., Smith, C. D., Smith, W., Vijaykumar, S., Senadhi, S. E., Ealick, S. E., Carter, D. C., Snyder, R. S., Weber, P. C., Salemme, F. R., Ohlendorf, D. H., Einspahr, H. M., Clancy, L. L., Navia, M. A., McKeever, B. M., Nagabhushan, T.

L., Nelson, G., McPherson, A., Koszelak, S., Taylor, G., Stammers, D., Powell, K., Darby, G. & Bugg, C. E. (1991) *Journal of Crystal Growth* **110,** 302-311.

52. GarciaRuiz, J. M. & Moreno, A. (1997) *Journal of Crystal Growth* **178,** 393-401.

53. Corbett KD, B. J. (2003) *EMBO JOURNAL* **22,** 151-163.

54. West, A. P., Giannetti, A. M., Herr, A. B., Bennett, M. J., Nangiana, J. S., Pierce, J. R., Weiner, L. P., Snow, P. M. & Bjorkman, P. J. (2001) *Journal of Molecular Biology* **313,** 385-397.

55. Savage DF, E. P., Robles-Colmenares Y, O'Connell JD, Stroud RM (2003) *PLOS BIOLOGY* **1,** 334-340.

56. Kong, L. B., Siva, A. C., Kickhoefer, V. A., Rome, L. H. & P.L., S. (2000) *RNA-A Publication of the RNA Society* **6,** 890-900.

57. Glieder, A., Farinas, E. T. & Arnold, F. H. (2002) *Nature Biotechnology* **20,** 1135-1139.

58. Chang, G., Spencer, R. H., Lee, A. T., Barclay, M. T. & Rees, D. C. (1998) *Science* **282,** 2220-2226.

59. Ono, T., Losada, A., Hirano, M., Myers, M. P., Neuwald, A. & Hirano, T. (2003) *Cell* **115,** 109-121.

60. Rosenbaum, D., Zamora, P. C. & Zukoski, C. F. (1996) *Physical Review Letters* **76,** 150-153.

61. Rosenbaum, D. F. & Zukoski, C. F. (1996) *Journal of Crystal Growth* **169,** 752-758.

62. Ataka, M. (1993) *Phase Transitions* **45,** 205-219.

63. Carbonnaux, C., Rieskautt, M. & Ducruix, A. (1995) *Protein Science* **4,** 2123-2128.

64. Mikol, V. & Giege, R. (1989) *Journal of Crystal Growth* **97,** 324-332.

65. Howard, S. B., Twigg, P. J., Baird, J. K. & Meehan, E. J. (1988) *Journal of Crystal Growth* **90,** 94-104.

66. Kam, Z., Shore, H. B. & Feher, G. (1978) *Journal of Molecular Biology* **123,** 539-555.

67. Muschol, M. & Rosenberger, F. (1997) *Journal of Chemical Physics* **107,** 1953-1962.

68. Forsythe, E. L., Judge, R. A. & Pusey, M. L. (1999) *Journal of Chemical and Engineering Data* **44,** 637-640.

69. Saridakis, E. E. G., Stewart, P. D. S., Lloyd, L. F. & Blow, D. M. (1994) *Acta Crystallographica Section D-Biological Crystallography* **50,** 293-297.

70. Saridakis, E. & Chayen, N. E. (2003) *Biophysical Journal* **84,** 1218-1222.

71. DeLucas, L. J., Bray, T. L., Nagy, L., McCombs, D., Chernov, N., Hamrick, D., Cosenza, L., Belgovskiy, A., Stoops, B. & Chait, A. (2003) *Journal of Structural Biology* **142,** 188-206.

72. tenWolde, P. R. & Frenkel, D. (1997) *Science* **277,** 1975-1978.

73. George, A. & Wilson, W. W. (1994) *Acta Crystallographica Section D-Biological Crystallography* **50,** 361-365.

74. Guo, B., Kao, S., McDonald, H., Asanov, A., Combs, L. L. & Wilson, W. W. (1999) *Journal of Crystal Growth* **196,** 424-433.

75.   Stura, E. A., Nemerow, G. R. & Wilson, I. A. (1992) *Journal of Crystal Growth* **122,** 273-285.

76.   Santesson, S., Cedergren-Zeppezauer, E. S., Johansson, T., Laurell, T., Nilsson, J. & Nilsson, S. (2003) *Analytical Chemistry* **75,** 1733-1740.

77.   Taylor, G. I. (1953) *Proceedings of the Royal Society of London Series a-Mathematical and Physical Sciences* **219,** 186-203.

78.   Chen, H. & Meiners, J. C. (2004) *Applied Physics Letters* **84,** 2193-2195.

79.   Stroock, A. D., Dertinger, S. K. W., Ajdari, A., Mezic, I., Stone, H. A. & Whitesides, G. M. (2002) *Science* **295,** 647-651.

80.   Song, H., Tice, J. D. & Ismagilov, R. F. (2003) *Abstracts of Papers of the American Chemical Society* **226,** 442.

81.   Kundu, P. K. & Cohen, I. M. (1990) *Fluid Mechanics* (Academic Press, San Diego).

82.   Holden, M. A., Kumar, S. & Beskok, A. (2003) *Journal of Micromechanics and Microengineering* **13,** 412-418.

83.   Torronen, A., Harkki, A. & Rouvinen, J. (1994) *Embo Journal* **13,** 2493-2501.

84.   Torronen, A. & Rouvinen, J. (1995) *Biochemistry* **34,** 847-856.

85.   Barnes, C. L., Snell, E. H. & Kundrot, C. E. (2002) *Acta Crystallographica Section D- Biological Crystallography* **58,** 751-760.

86.   Miller, T. Y., He, X. M. & Carter, D. C. (1992) *Journal of Crystal Growth* **122,** 306-309.

87.   Ng, J. D., Sauter, C., Lorber, B., Kirkland, N., Arnez, J. & Giege, R. (2002) *Acta Crystallographica Section D - Biological Crystallography* **58,** 645-652.

88. Thomas, B. R., Chernov, A. A., Vekilov, P. G. & Carter, D. C. (2000) *Journal of Crystal Growth* **211,** 149-156.

89. Lin, H., Petsev, D. N., Yau, S. T., Thomas, B. R. & Vekilov, P. G. (2001) *Crystal Growth & Design* **1,** 73-79.

90. Chernov, A. A., Garcia-Ruiz, J. M. & Thomas, B. R. (2001) *Journal of Crystal Growth* **232,** 184-187.

91. Skordalakes, E. & Berger, J. (2003) *CELL* **114,** 135-146.

92. Xia, Y. & Whitesides, G. (1998) *Angew Chem Int Edit* **37,** 551-575.

93. Chiu, C. Y., Jeon, N. L., Huang, H., Kane, R. S., Wargo, C. J., Choi, I. S., Ingber, D. E. & Whitesides, G. M. (2000) *Proceedings of the National Academy of Sciences of the United States of America* **97,** 2408-2413.

94. Jackman, R. J., Wilbur, J. L. & Whitesides, G. M. (1995) *Science* **269,** 664-666.

95. Schueller, O. J. A., Zhao, X. M., Whitesides, G. M., Smith, S. P. & Prentiss, M. (1999) *Advanced Materials* **11,** 37-41.

96. Yang, P. D., Wirnsberger, G., Huang, H. C., Cordero, S. R., McGehee, M. D., Scott, B., Deng, T., Whitesides, G. M., Chmelka, B. F., Buratto, S. K. & Stucky, G. D. (2000) *Science* **287,** 465-467.

97. McDonald, J. C., Duffy, D. C., Anderson, J. R., Chiu, D. T., Wu, H. K., Schueller, O. J. A. & Whitesides, G. M. (2000) *Electrophoresis* **21,** 27-40.

98. Chou, H., Spence, C., Scherer, A. & Quake, S. R. (1999) *Proceedings of the national Academy of Sciences of the United States of America* **96,** 11-13.

99. Duffy, D. C., McDonald, J. C., Schueller, O. J. A. & Whitesides, G. M. (1998) *Analytical Chemistry* **70,** 4974-4984.

100. Studer, V., Hang, G., Pandolfi, A., Ortiz, M., Anderson, W. F. & Quake, S. R.
     (2004) *Journal of Applied Physics* **95,** 393-398.

101. Stjernstrom, M. & Roeraade, J. (1998) *Journal of Micromechanics* **8,** 33-38.